TERAHERTZ-BAND COMMUNICATIONS AT VARIOUS ATMOSPHERIC ALTITUDES

by
AKHTAR SAEED

Submitted to the Faculty of Engineering and Natural Sciences
in partial fulfilment of
the requirements for the degree of Doctor of Philosophy

Sabancı University
July 2021

TERAHERTZ-BAND COMMUNICATIONS AT VARIOUS ATMOSPHERIC ALTITUDES

Approved by:

Date of Approval: July 06, 2021

ABSTRACT

TERAHERTZ-BAND COMMUNICATIONS AT VARIOUS ATMOSPHERIC ALTITUDES

AKHTAR SAEED

Electronics Engineering Ph.D Dissertation, July 2021

Dissertation Supervisor: Prof. Özgür Gürbüz
Dissertation Co-Supervisor: Assoc. Prof. Mustafa Alper Akkaş

Keywords: Absorption loss, bandwidth allocation, beam misalignment, colored noise, drone to drone communications, ergodic channel capacity, LBLRTM, multi path fading, non-terrestrial communications, terahertz communication.

Terahertz (THz) band (0.1-10 THz) communications shows a huge potential for the prospective beyond 5G and 6G wireless systems, as the band offers large bandwidth and data rates as compared to the existing sub 6 GHz bands, which are almost saturated. Traditionally, the THz band has been employed for the sea-level-short range communication, due to the large absorption loss the THz waves experience by the water vapor molecules present in the atmosphere, which decreases across higher atmospheric altitudes, where the communication over the THz band can be highly leveraged among various practical aerial vehicles. In this dissertation, first, we investigate path loss over the THz band (0.75-10 THz) at various atmospheric altitudes, ranges and directions by realistically calculating the THz absorption loss. Four practical altitudes are considered, corresponding to Drone-to-Drone (Dr2Dr), Jet plane-to-Jet plane (J2J), Unmanned Aerial Vehicle-to-Unmanned Aerial Vehicle (U2U), and near-space Space-to-Space (S2S) communications. Following comparison and validation with two real-world experimental results from the literature measured at the sea-level, Line by Line Radiative Transfer Model (LBLRTM) is used to obtain realistic THz transmittance values for each altitude case and setting. Numerical results show that as the altitude increases, the water vapor concentration decreases, enabling the communication over the THz band to be more feasible as compared to the sea-level communication. Moreover, the total usable bandwidth results over the THz band exhibit that the upper bounds of 8.218 THz, 9.142 THz

and 9.250 THz are usable up to the transmission distance of 2 km for J2J, U2U and S2S communication cases, respectively. Next, the THz band is further explored for the identical four aerial communications at the practical altitudes, variable directions and distances, under realistic weather and channel fading conditions, due to beam misalignment and also multi path fading. A channel model for aerial communications at THz band is proposed to calculate the common flat bands (CFB) for frequency-selective path gain and the colored noise spectrums, both of which are highly affected by the atmospheric conditions. An extensive capacity analysis is presented, considering equal power (EP) and water-filling (WF) allocation, showing that when there is no fading, capacity for aerial links is several orders of magnitude larger than the sea-level capacity. For both the proposed CFB and the Standard (STD) approaches, the sea-level capacity is enhanced by an order of magnitude for the drones, which is doubled for the jet plane scenario, which is further tripled for UAVs, which is again increased by another order of magnitude for the satellite communications. When ergodic capacity is computed for the fading scenarios, it is shown that the impact of fading vanishes at higher altitudes. Sea-level ergodic capacity is increased by an order of magnitude for drone-to-drone communications, providing several Tbps at 10 m, while 10s of Tbps is achievable among jet planes and UAVs, and several 100s of Tbps is possible for satellites/cubesats at 1 km under fading, suggesting that THz band is a promising alternative for aerial communications. Then, we consider various realistic mobility scenarios of THz-enabled Dr2Dr links over the THz band (0.75-4.4 THz), also incorporating real drone mobility traces. Additionally, we consider real THz antennas over the THz band (0.75-4.4 THz) under various drone mobility scenarios for evaluating the true potential of utilizing the THz band among drone communications. For maximizing the capacity, we propose a channel selection scheme, MaxActive, which intelligently selects THz narrowband channels promising the maximum capacity. Then, we propose a joint process of channel selection, beamwidth adjustment and power control for the capacity maximization. Based on this joint process, we compare the MaxActive scheme with the CFB scheme as well as the STD narrowband scheme in terms of capacity and spectral efficiency using both WF and EP allocations. It is inferred that the beamwidth misalignment highly affects the THz band Dr2Dr communication. Moreover, the link performance of the MaxActive scheme even with EP approaches the MaxActive and STD schemes with WF, while clearly outperforming CFB and STD with EP.

ÖZET

TEZ BAŞLIĞI

TEZ YAZARI: AKHTAR SAEED

PROGRAM ADI DOKTORA TEZİ, TEMMUZ 2021

Tez Danışmanı: Prof. Dr. Özgür Gürbüz
Tez Eş-Danışmanı: Doç. Dr. Mustafa Alper Akkaş

Anahtar Kelimeler: Emilim kaybı, bant genişliği tahsisi, ışın hizalaması, renkli gürültü, Drondan - Drona iletişim, ergodik kanal kapasitesi, LBLRTM, çok yollu sönümleme, karasal olmayan iletişim, terahertz iletişimi.

Terahertz (THz) bant iletişimi (0.1 - 10 THz), neredeyse tamamıyla kullanılmış olan mevcut 6 GHz alt bantlara kıyasla, çok büyük bant genişliği ve veri hız sunduğundan; potansiyel 5G ve 6G kablosuz sistemlerinin ötesinde büyük bir iletişim potansiyeli sunar. Geleneksel olarak, THz bandı, atmosferde bulunan su buharı molekülleri tarafından kullanılabilir. Bu moleküller, THz dalgalarının bulunduğu daha yüksek atmosferik irtifalarda, azalan büyük emilim kaybı nedeniyle, deniz seviyesinde kısa menzilli iletişim için kullanılmıştır. THz bandı, farklı hava araçları arasında daha çok tercih edilebilir. Bu çalışmada, ilk olarak, THz emilim kaybı gerçekçi bir şekilde hesaplanmış ve farklı iletim mesafeleri ve yönleri dikkate alınarak, çeşitli atmosferik irtifalarda THz bandı (0.75 - 10 THz) üzerinde yol kaybı analizi araştırılmıştır. Drondan - Drona (D-D), Jet uçağından - Jet uçağına (J-J), İnsansız Hava Aracından İnsansız Hava Aracına (İHA - İHA) ve Yakın Uzay Uydusundan Yakın Uzay Uydusuna (Y-Y) karşılık gelen dört pratik irtifa dikkate alınmıştır. Literatürde, deniz seviyesinde ölçüm yapan iki çalışmanın deneysel sonuçları karşılaştırılmış ve doğrulanmıştır. Bu doğrulamanın ardından, her bir irtifa durumu ve ayarına karşı, gerçekçi THz bant iletim değerlerini elde etmek için "Satırdan Satıra Işınımlı Transfer Modelleri (SSITM)" kullanılmıştır. Sayısal sonuçlar, rakım arttıkça su buharı konsantrasyonunun azaldığını ve THz bandı üzerinden iletişimin, deniz seviyesi iletişimine kıyasla daha uygun olduğunu göstermektedir. Ayrıca, THz bandı üzerinden toplam kullanılabilir bant genişliği sonuçları, J-J, İHA-İHA ve Y-Y iletişimi için; 8.218 THz, 9.142 THz ve 9.250 THz'lik üst sınırların, 2 km'lik iletim

mesafesine kadar kullanılabilir olduğunu göstermektedir. Ayrıca, THz bandı, farklı irtifa, yön ve mesafelerdeki hava araçları dikkate alınarak, gerçekçi hava ve kanal zayıflaması koşulları altında, ışın hizasızlığı ve çok yollu sönümleme nedeniyle aynı dört hava iletişimi için daha fazla araştırılmıştır. Her ikisi de atmosferik koşullardan oldukça etkilenen frekans seçici yol kazancı ve renkli gürültü spektrumları için Ortak Düz Bantları (ODB) hesaplamak amacıyla THz bandında hava iletişimi için bir kanal modeli önerilmiştir. EG (Eşit Güç) ve SD (Su Doldurma) tahsisi göz önünde bulundurularak, kapsamlı bir kapasite analizi sunulmuş ve zayıflama olmadığında, hava bağlantıları kapasitesinin, deniz seviyesi kapasitesinden birkaç kat daha büyük olduğunu gösterilmiştir. Hem önerilen hem de standart yaklaşımlar için, deniz seviyesi kapasitesi, dronlar için bir büyüklük sırasına göre artırılır. İHA'lar için üç katına çıkan jet uçağı senaryosu için iki katına çıktı ve uydu için başka bir büyüklük sırasına göre artırıldı. iletişim. Sönme senaryoları için ergodik kapasite hesaplandığında, sönüm etkisinin yüksek irtifalarda ortadan kalktığı gösterilmiştir. Deniz seviyesindeki ergodik kapasite, insansız hava aracından insansız hava aracına iletişim için bir büyüklük sırasına göre artırılır ve 10 m'de birkaç Tbps sağlarken, Jet uçakları ve İHA'lar arasında 10s Tbps'ye ulaşılabilir ve solma altında 1 km'deki uydular/küpatlar için birkaç 100s Tbps mümkündür. THz bandının hava iletişimi için umut verici bir alternatif olduğu. Sönümleme senaryoları için ergodik kapasite hesaplandığında, yüksek irtifalarda geniş haberleşme menzilleri için sönümleme etkisinin ortadan kalktığı gösterilmiştir. Ardından, THz bağlantı kapasitesini ve spektral verimliliği değerlendirmek için gerçek dünya D-D hareketlilik izlerini de dikkate alan çeşitli gerçekçi hareketlilik senaryoları göz önünde bulundurulmuş ve böylece THz etkin D-D senaryolarını değerlendirilmiştir. THz bandı (0.75 - 4.4 THz) üzerinde kapasiteyi en üst düzeye çıkarmak için, maksimum kapasiteyi vaat eden THz dar bant kanallarını akıllıca seçen MaksAktif kanal seçim şemasını önerilmektedir. MaksAktif'i EG ve SD tahsislerini kullanarak, kapasite ve spektral verimlilik açısından ODB şeması ve Standart Dar Bant (SDB) şeması karşılaştırılmıştır. EG'li MaksAktif'in SD ile MaksActif ve SDB şemalarına iyi bir şekilde yaklaştığı ve EG ile ODB ve SDB'den açıkça daha iyi bir performans gösterdiği sonucuna varılmıştır.

ACKNOWLEDGEMENTS

I would like to express my deepest regards to my advisor, Prof. Dr. Ozgur Gurbuz, for providing me the prestigious opportunity to work under her supervision, in addition to her support and motivation throughout my studies. I am also grateful to her for her devotion, which steered me towards the completion of this dissertation successfully, and embracing me for my career ahead. I also greatly appreciate Prof. Gurbuz to be my mentor, whose valuable supervision to me will guide me and shape me over my whole life ahead. Additionally, I would like to thank Prof. Gurbuz for her financial support to me over the last semester of my studies, enabling me to perform an un-interrupted research. I would also like to thank my co-advisor, Assoc. Prof. Dr. Mustafa Alper Akkas, who introduced me to the field of Terahertz Communications, and for his valuable advice and support throughout my PhD. I would also like to show my regards to all the academic members of the Faculty of Engineering and Natural Sciences at the Sabanci University for their constructive and critical reviews over the entire studies. Special gratitude goes to my Ph.D. Thesis Progress Committee members, Prof. Dr. Ibrahim Tekin and Prof. Dr. Albert Levi, for providing their valuable and constructive comments on my work at each milestone, helping me to perform my Ph.D. and directing me towards my research way. I would also like to pay my regards to all existing and former team members of the Telecommunications and Networking Lab, Sabanci University, for their perpetual support and real friendship right from the very beginning of my studies at Sabanci University. I keep a radiant and deep-colored memory of my days in the lab and all the remarkable guys that I have met over all these years. To all of you, I thank you very much for the distinctive atmosphere we have had in the lab together. I do not have words to express my gratitude to my family, including my late parents; Saeed Ahmed and Shamim Saeed, my wife Sharmeen, my son Abdullah and my daughter Fatima. This achievement would have not been possible without their love, support and encouragement.

To my family, for their endless love, support and encouragement.

Table of Contents

List of Tables

List of Figures

List Of Abbreviations

AOC Antennas on Chip
BS Base Station
BM Beam Misalignment
CFB Common Flat Band
Dr2Dr Drone to Drone
DSNs Drone Sensor Networks
EM Electromagnetic
EP Equal Power
HAP High Altitude platform
HITRAN HIgh resolution TRansmission molecular AbsorptioN database
HotW HITRAN on the Web
IoT Internet of Things
IRS Intelligent Reflective Surface
IR infrared
J2J Jet Plane to Jet Plane
LBLRTM Line by Line Radiative Transfer Model
LAN Local Area Network
LOS Line Of Sight
MIMO Multiple Input Multiple Output
mmWave Millimeter Wave
MP Multi Path
NF Noise Figure
OFDM Orthogonal Frequency Division Multiplexing
PAN Personal Area Network
PSD Power Spectral Density
Rx Receiver
STD Standard
S2S Space to Space
THz Terahertz
Tx Transmitter

UAV Unmanned Aerial Vehicle
UE User Equipment
U2U UAV to UAV
WF Water-Filling
V-BW Variable-Bandwidth
VHF Very High Frequency
WSN Wireless Sensor Network

Chapter 1

INTRODUCTION

Wireless communications has been mostly implemented in the sub-6 GHz spectrum, which is almost saturated. With the progression towards impending beyond 5G systems and prospective 6G systems [1], telecommunication researchers and policy makers have started looking into the higher frequency spectrum to meet the ever increasing demand of data rates [2]. Towards this goal, the Terahertz (THz) band (0.75-10 THz) is being considered as one of the prospective candidates, due to the potential of providing large amount of bandwidth [3].The THz band (0.1–10 THz), as shown in Fig. 1.1 [4,5], is envisioned as one of the key enablers towards ubiquitous wireless communications beyond 5G accommodating a large number of connected devices and ultra-high user data rates.

The THz band is located in between the millimeter wave (mmWave) and the far infrared (IR) band and still considered one of the least investigated and exploited regions in the electromagnetic spectrum although it offers a much higher bandwidth than the mmWave range and more favorable propagation conditions than the IR band. Similar to mmWave communications, THz band can be employed for backhaul links for transmitting signals over large bandwidths among various base stations. The THz band can also be considered as a replacement of optic fiber and copper-based Local Area Networks (LANs) for macro and micro cell communications in remote and rural areas. Moreover, THz band can also be considered for very-short range communications (whisper radio) including on-board communications, nano-sensors, etc. In addition to wireless communication, the THz band has also been employed in other applications such as in sensing, imaging using high-resolution spectroscopy. Recently, significant progress has been made with respect to THz devices based on different technologies, and commercial THz systems are anticipated to become a reality in the near future. For example, there is a common understanding now that the THz communications will become an integral part of the upcoming 6G systems family [1, 6].

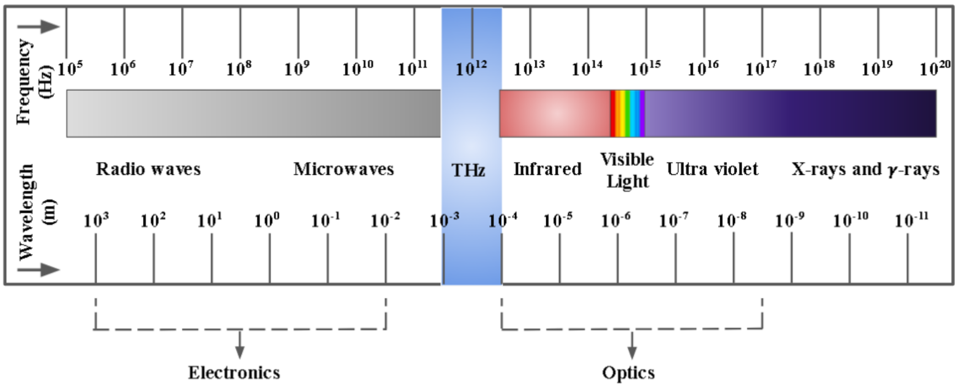

Figure 1.1 The terahertz band in the electromagnetic spectrum.

The intelligent information society of 2030 is expected to be globally information driven, highly digitized, with the support of unlimited and near instant complete wireless connectivity [7] and 6G will be the prime catalyst for achieving this target, connecting everything in all dimensions, as well as concatenating almost all different functions such as, communication, sensing, imaging, computing, caching, navigation, control etc. for supporting all applications [8]. As wireless communications is rapidly progressing towards 6G, the exponentially growing network traffic arises the need of exploiting the electromagnetic spectrum above the existing sub 6 GHz bands, which are almost saturated. A possible solution to this need is to utilize the THz band as the bridge between the 5G mmWave band and the free space optics band [9, 10]. THz band offers large bandwidth, favorable for very high data rate applications [11], while at the same time promises huge antenna gains due to shorter wavelengths as compared to the lower frequency bands [4, 12].

Propagation in the THz band is highly affected by the absorption loss, which accounts for the attenuation suffered by the EM wave since some of its energy is converted into vibrational kinetic energy by gas molecules (e.g. water vapor) in the atmosphere [13]. This absorption loss is highest at the sea-level, as the atmospheric gas concentration is at the maximum [4, 14, 15]. For this reason, THz communication at the sea-level has been studied mostly for very short range communications, such as for on-chip communications [16] or for connecting data centers within up to 10 m.

For obtaining the THz absorption loss, certain radiative transfer tools have been employed by the researchers working on THz band communications. For instance, for identifying transmission windows at the sea-level communication, HITRAN on the Web is employed for obtaining absorption coefficients in [17]. Again, considering HITRAN, [18] presents channel modeling and capacity analysis up to 10 m under various transmit power allocations over constant narrowbands within 0.1-10 THz [19]. In [20], a theoretical multi-ray channel model is presented for 0.06-10 THz band at the sea-level, considering ranges up to 6 m. In [14], a distance-aware based bandwidth adaptation resource allocation is proposed; a rate of 100 Gbps is reported within 21 m, suggesting the THz band to be a feasible candidate of 5G cellular network hot spots, wireless local area networks and wireless personal area networks (PANs) [4]. THz band (0.275-0.4 THz) is analyzed over distance ranging from 10 m to 100 m as a possible candidate to the wireless fiber extenders in [21] considering the joint impact of beam misalignment and multi path fading. It is shown in [21] that the degradation effect of the beam misalignment and multi path fading on the ergodic capacity can be countered by provisioning high transmit power levels.

1.1 Motivation: Terahertz Communication In The Sky

The earth's atmosphere has its maximum gaseous concentration at the sea-level, which subsides at higher altitudes, leading up to our question: Can THz band be utilized for wireless communication across high altitudes, for communicating aerial vehicles? The existing aerial communication systems (see Fig. 1.2 for example scenarios at respective practical altitudes) operate at lower frequencies, and lately, distributed aerial communications and computing platforms has been gathering attention with the research advancements in 5G technologies, edge computing, and machine learning [22].

Considering the state-of-the-art aerial communications, in [23], several drone communication systems are proposed to offer bandwidths in the order of several 100 MHz in the ISM band, providing a backup link for bursty and non-homogeneous data traffic demand, which can occur in natural disasters or in communal congregation/gathering events (e.g., concerts [24]). Jet planes traditionally use the Very High Frequency (VHF) bands for communicating with each other and with ground stations [25]. High altitude Unmanned Aerial Vehicles (UAVs) and High Altitude Platforms (HAPs) have recently proven to be effective communication relays between satellites and earth stations (to substantially reduce propagation delays) typically operate over L-band (0.5-1 GHz) and S-band (2-4 GHz) [26]. Satellites conventionally employ microwave bands for communication links [27], where the L-band is typically used for Global Positioning System (GPS) and satellite phones, C-band (4-8 GHz) is used for TV networks, and Ka-band (26-40 GHz) is used for satellite-based radars [28].

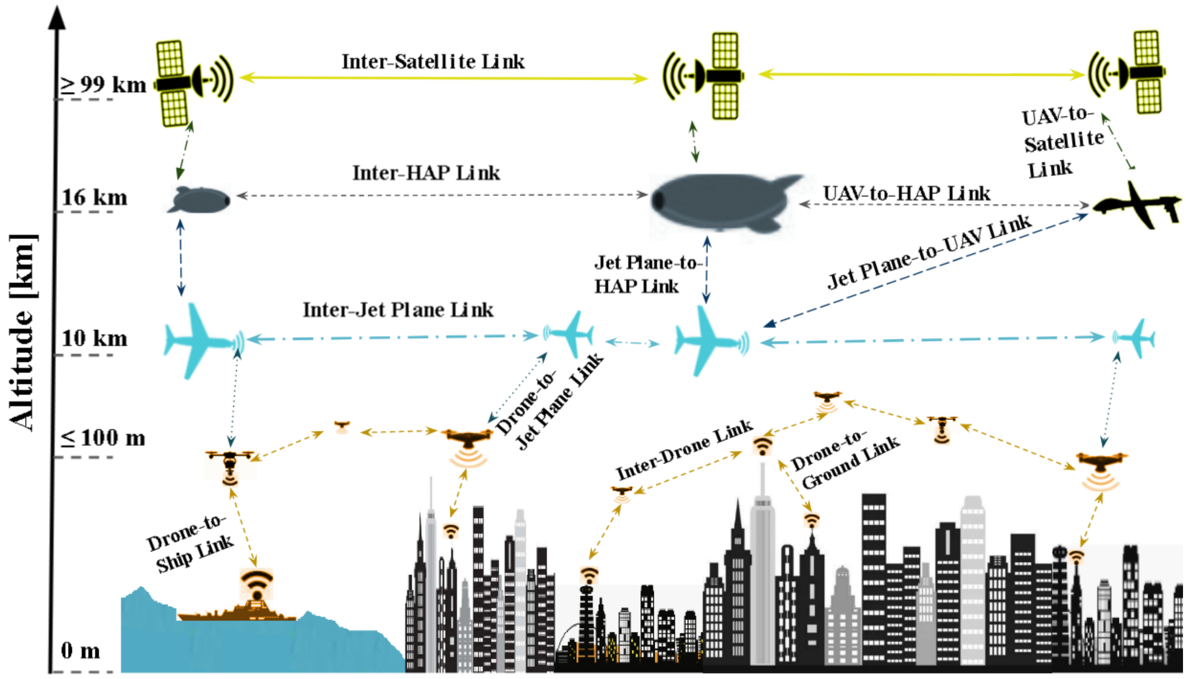

Figure 1.2 Possible real scenarios of THz-enabled aerial vehicles across various atmospheric altitudes.

For aerial communications, a holistic investigation of THz band communication among Vertical Heterogeneous Networks (V-HetNets) is suggested in [29], proposing that the THz communication can be a possible candidate band for 6G and even beyond for back-hauling and front-hauling small cells. V-HetNets include satellites, HAPs, flying drone base stations, etc (Fig. 1.2). The effect of UAV hovering fluctuations in the mmWave communication links under multi path fading is analyzed in [30], where it is shown that extent of stability of the antennas mounted on the UAV transceivers has considerable effect on the system performance, while provisioning higher antenna gains does not surely improve the system's performance. Therefore, under the hovering fluctuations, antenna radiation pattern optimization is the key governing the system's performance. Geostationary Satellite-to-Earth links utilizing THz band is theoretically investigated in [31] by employing ITU atmospheric model for obtaining the absorption effect over 0.1-0.5 THz band, showing that the satellite-to-Earth links can possibly support up to 10 Gbps per GHz, given that high gain power amplifiers and high antenna gains are supported. In [32], am atmospheric tool is employed for analyzing Tbps links between satellites and ground stations and also among high altitude balloons and satellites. Line by Line Radiative Transfer Model (LBLRTM) tool is utilized in [33] for analyzing transmittance analysis of the THz band (0.75-100 THz) under pristine conditions. In the following, we provide the THz band communication for drone-specific cases/scenarios that are available in the literature.

Drones will soon inhabit our skies as they are easily available, reliable and low-cost devices. The demand for such hovering drones is increasingly witnessed in civil and government applications, as globally, many governments and industries have been investing heavily in deploying the drone networks as per their requirements [34]. Typically, small drones with multi-copter-like functionalities are favorable due to their cheap maintenance and convenient deployments [35]. In order to achieve a certain mission, it is usually desirable to deploy a collection or swarm of drones in a networked fashion [36]. Such drone networks or drone sensor networks can monitor a large coverage area and the sensed data can be gathered with enhanced reliability, resilience and fault tolerance under diverse conditions.

Recently, THz band has been considered for UAV communications. Aerial channel models for UAVs communications over 2 GHz to 900 GHz under various weather conditions (rain, snow and fog) is studied in [37], showing that the attenuation caused by the rain is the most severe for mmWave bands, whereas the attenuation at THz bands increases by the snow. Antennas and codebook designs at 28 GHz and 140GHz (sub-THz frequency for upcoming 6G systems) for UAV communications with realistic antenna simulations and flight patterns are studied in [38], showing that the appropriate codebook design and multi-array configurations are important particularly for long range applications, offering over 1 Gbps rate at 1 km under moderate rain. In [39], a comprehensive survey is provided on Antennas On Chips (AOCs) as a candidate for the 5G wireless systems, Wireless Sensor Networks (WSNs), UAVs, Internet of Things (IoT), etc. The paper also provides the existing AoCs with respect to specific applications over low-frequency bands, mmWave bands and THz bands.

A wireless network with THz-based UAVs serving ground users are considered in [40] with the goal of minimizing the transmission delays of both the uplink and downlink by optimizing jointly the UAV location, bandwidth and transmit powers of the served users. A sub-optimal solution to this problem is also proposed as an iterative algorithm, showing a reduction in delay by up to 59.3 %, 49.8 % and 75.5 %, respectively, as compared to optimizing only the UAV location, bandwidth allocation or the transmit power control. A heterogeneous network comprising of UAVs and macro base station working at sub-6 GHz and small cells working at THz frequencies is presented in [41], where it is shown that the ground users linked to the THz-based small cells experience significant improvement rates in contrast to those users which are connected to the tier of sub-6GHz. In [42], THz drone/UAVs networks are studied by analyzing area spectrum efficiency and coverage probability, showing that due to large path loss at the THz frequency of 0.35 THz, a larger UAVs density is required for a certain coverage probability as compared to the lower carrier frequencies. In [43], THz Multiple Input Multiple Output (MIMO) Orthogonal Frequency Division Multiplexing (OFDM) communication is considered between two UAVs by studying estimation error bounds of the orientation and position. It is concluded that the position accuracy at millimeter levels can be targeted by minimizing the transmitter-receiver separation. In [44], outage probability is studied for a single-cell network having a UAV as a decode-and-forward relay in full-duplex mode, assisting a Base Station (BS) and extending its coverage over the THz channel. Transmit power of the mobile device and the UAV with the objective of minimizing the outage probability is derived and compared with the fixed power allocation, showing that the outage probability is decreased by 20 % with the obtained optimum power levels as compared to the fixed power allocation. In [45], UAVs and Intelligent Reflective Surface (IRS) are employed for providing the THz communications over 240-400 GHz, with 20 GHz bandwidth of the sub-band, having the aim of maximizing the minimum average rate of the UAVs.

Due to narrow transmission and reception beams, THz communication links between mobile aerial vehicles need to be frequently aligned. For instance, an optimal beamwidth selection is presented in [46] for enabling high rate links between mobile aerial vehicles. An adaptive beamwidth control for UAV communications operating at THz center frequency of 0.3 THz, 10 GHz bandwidth is proposed in [47], where a stochastic beam controlling scheme, LeTera is proposed. It is shown that LeTera dynamically predicts the best beamwidth via echo state learning with statistical information of the UAV mobility patterns obtained using real mobility traces, with an accuracy of 99 %, which in turn leads to a near-optimal capacity in mobile environments. The effect uncertainties due to the mobility of flying drones communicating over the mmWave and THz band is studied in [48], showing that the micro-scale mobility uncertainties has negligible effects on the link capacity, whereas the small scale and large scale mobility instances pose a significant degradation in the link capacity. The work of [48] is extended in [49], where LeBeam scheme is proposed with the object of maximizing the expected capacity of the mmWave/THz band links by dynamically obtaining the optimal beamwidth with respect to the mobility uncertainties. Based on the research works on the THz aerial communications provided above, following open research issues are studied in this dissertation:

In [33], the atmospheric attenuation is investigated in detail using LBLRTM for the frequency range [0.1-100 THz] under pristine conditions. It is shown in [33] that LBLRTM can provide good atmospheric predictions for earth-to-space links. Earlier in the literature, LBLRTM has been employed for the transmittance-based atmospheric analysis [33, 50, 51]. However, extension of the transmittance-based atmospheric analysis to the total path loss and the subsequent evaluation of total usable bandwidth at various atmospheric altitudes are not present in the literature. Moreover, in the literature, although standard distance-dependent capacity computation at the sea-level is available, considering various transmit power allocation over constant narrowbands [18, 19], however, the concept of an altitude-dependent variable bandwidth approach based on common flat bands among the path gain and the colored noise is not studied in the literature. Furthermore, for THz communication within drones under mobility, the authors in [48, 49], considers only beamwidth optimization, while considering only a single THz band for transmission. However, to the best of our knowledge, joint channel selection over the THz band (0.75-4.4 THz) and the beamwidth adjustment considering realistic 3D beamwidths for Tx and Rx drones is not present in the literature. Motivated by the open research areas of THz aerial communications, in this dissertation, we study each of the above open research areas in the literature. The contributions are provided in the subsequent section.

1.2 Thesis Contributions

In this dissertation, we study the THz band for the aerial communications with realistic transmittance from LBLRTM. We perform path loss, total usable bandwidth of four practical aerial communication scenarios with the constant noise model. Then, we propose a variable bandwidth model with altitude-dependent THz capacity computations under both ideal channel and fading channel conditions using colored noise model. Additionally, as a special case of aerial communications, we consider THz communication for Drone-to-Drone (Dr2Dr) communications under mobility, also considering real-world drone traces as well as real THz antennas. We also propose another channel selection scheme, MaxActive, with the objective of maximizing capacity under both water-filling (WF) and equal power (EP) allocations of the THz-enabled Dr2Dr link. Moreover, we propose a joint channel selection, beamwidth adjustment and power control considering the MaxActive, Common Flat Band (CFB) and Standard (STD) schemes for obtaining the capacity and spectral efficiency. Our contributions and findings can be summarized as follows:

- We analyze the total path loss values at four atmospheric altitudes, in addition to the sea-level communication. We observe that for the atmospheric altitudes of up to 1 km, the absorption effects are significant. At 10 km altitude, the total path loss exhibits mainly the free space spread loss behavior due to negligible absorption at the altitude. For the altitudes above 16 km, the absorption effect becomes negligible.
- The numerical results show that for the altitudes higher than 16 km, the entire

THz band (0.75-10 THz) is usable as a single transmission window. Across 10 km altitude, a bandwidth of greater than 8 THz is usable, while for the altitudes lower than 1 km, only the initial window of 0.75-1 THz is usable.

- An altitude-dependent variable bandwidth communication model is developed, where the common flat bands of path gain and noise are determined, followed with the SNR and capacity computations for the determined jointly flat bands, which are summed over the entire THz band. THz channel capacity (without fading) is observed as a function of altitude, direction of transmission and range. Detailed capacity analysis is pursued, considering the common flat band and standard capacity computations, each using WF and EP allocations, for four aerial communication scenarios of drones, jet planes, UAVs, and satellites, under practical settings, various atmospheric weather conditions and fading.

- Numerical results show that for both the proposed and the standard approaches, the sea-level capacity is enhanced by an order of magnitude for the drones, which is doubled for the jet plane scenario, which is further tripled for UAVs, which is again increased by another order of magnitude for the space communications. When ergodic capacity is computed for the fading scenarios, it is shown that the impact of fading vanishes at higher altitudes. Sea-level ergodic capacity is increased by an order of magnitude for drone-to-drone communications, promising several Tbps at 10 m, while 10s of Tbps is achievable among jet planes and UAVs, and several 100s of Tbps is possible for satellites/cubesats at 1 km under fading, suggesting that THz band is a promising alternative for aerial communications.

- A novel bandwidth selection scheme, MaxActive, is proposed with the objective of maximizing the channel capacity of the THz-enabled Dr2Dr link under mobility. The proposed scheme is evaluated under both WF and EP allocations, also comparing with CFB and STD schemes under various realistic mobility scenarios.

- A realistic 3D antenna model is employed for THz-enabled Dr2Dr links under mobility with beamwidth adjustment provision to promise uninterrupted THz Dr2Dr links under mobility. Additionally, real THz antennas over the THz band (0.75-4.4 THz) are also considered under various drone mobility scenarios for revealing the true potential of employing the THz band for drone communications.

- It is observed that even with the EP allocation, the capacity offered by the proposed MaxActive scheme with constant gain, 3D symmetric and asymmetric beamwidths well approximates the capacity values of MaxActive, CFB and STD with WF allocations.

- For the ideal, perfectly aligned scenario, the WF capacity and spectral efficiency results with the constant gain, 3D symmetric beamwidths without adjustment are increased by an order of magnitude when the real THz antennas are employed. Moreover, real THz antennas under real mobility traces offer WF capacity and WF spectral efficiency values, improved by five and three orders of the magnitudes, respectively, as compared to the constant gain, 3D asymmetric beamwidths without adjustment.
- Considering the state-of-the-art THz antennas and real drone traces, employing the THz band (0.75-4.4 THz) for THz band Dr2Dr communications can promise WF-based capacity values in the order of several Gbps even if no beamwidth adjustment is provisioned, while for the perfectly aligned mobility, up to 2.8 Tbps of capacity is achievable, with a WF spectral efficiency of up to 11.88 bits/sec/Hz, depicting the potential of the THz band for Dr2Dr communications.

1.3 Thesis Organization

The rest of the dissertation is organized as follows: Chapter 2 presents the THz band propagation in the atmosphere. In Chapter 3, THz path loss and total usable bandwidth analyses for four practical aerial vehicles are provided considering constant noise model. In Chapter 4, for the identical four aerial scenarios, the capacity analysis is provided under both ideal and fading conditions with colored noise model, also presenting variable bandwidth approach with altitude dependent channel model. In Chapter 5, THz band Dr2Dr communication is considered with real-world drone mobility traces and real THz antennas, and a joint channel selection, beamwidth allocation and power control is proposed for maximizing channel capacity. Finally, the conclusions are provided in Chapter 6.

Chapter 2

TERAHERTZ PROPAGATION IN THE ATMOSPHERE

2.1 Terahertz Absorption Loss

For analyzing THz propagation in the atmosphere, we require the radiative transfer theory for computing the EM wave attenuation as it propagates across the atmosphere [52]. This attenuation is due to the molecular absorption in the atmosphere, where mainly the water vapor molecules induce this molecular absorption [4, 18]. Moreover, since the atmospheric gaseous concentration is at the maximum levels at the sea-level, therefore, the THz band communication at the sea-level is highly affected by this water vapor-based absorption, causing to limit the communication at the sea-level to be up to only a few meters. Therefore, for computing the total path loss, it becomes essential to incorporate the THz absorption loss in addition to the free space spread loss, which is due to the spread of the THz waves as it propagates across the atmosphere. The total path loss at THz frequency, f and distance, d between Tx and Rx is obtained as the sum of the free space spread loss in dB and the absorption loss in dB, as:

$$A_{pl}(f,d)[dB] = A_{abs}(f,d)[dB] + A_{spread}(f,d)[dB] \ . \tag{2.1}$$

$A_{abs}(f,d)$ provides the absorption loss experienced by the THz through the atmospheric propagation. This absorption loss is mainly due to the water vapor molecules in the atmosphere, and can be derived from the transmittance, $\tau(f,d)$, as [17,18,33]:

$$A_{abs}(f,d) = \frac{1}{\tau(f,d)} \quad , \tag{2.2}$$

and in dB scale,

$$A_{abs}(f,d)[dB] = 10log_{10}A_{abs}(f,d)\ . \tag{2.3}$$

$A_{spread}(f,d)$ denotes the free space spread loss due to the attenuation experienced by the THz wave while propagating through the atmosphere and the loss due to the isotropic antenna, which is obtained as [18, 53]:

$$A_{spread}(f,d)[dB] = 20log_{10}\left(\frac{4\pi fd}{c}\right)\ . \tag{2.4}$$

For obtaining realistic $A_{abs}(f,d)$ for a given settings such as THz frequency range, transmission distance, atmospheric composition, etc., across the THz band (0.1-10 THz), various radiative transfer tools are available. These radiative transfer tools also enable to obtain $\tau(f,d)$ values [54, 55], which is the absorption gain corresponding to a given setting. Thus, $\tau(f,d)$ is the primary parameter for obtaining the THz absorption. In the following, state-of-the-art radiative transfer tools are mentioned for computing the THz absorption loss at the sea-level as well as at various altitudes across earth's atmosphere.

2.2 Radiative Transfer Tools

2.2.1 HITRAN on the Web

HITRAN on the Web (HotW) is an online tool widely used to assess spectral line parameters of various atmospheric gases which is required for analyzing the radiative transfer modeling and studying absorption spectra of gaseous molecules [56]. The tool is based on the standard HITRAN database [57] that comprises of the infrared spectrum which is further extended to higher spectral regions spanning from microwave up to ultraviolet (0.00001-25232.0 cm^{-1}). The tool offers to model wavenumber profiles including transmittance functions, absorption functions and absorption coefficients considering various parameters including pressure, temperature and transmission distance. The tool is based on the earlier developed Internet information systems Spectroscopy of Atmospheric Gases (SPECTRA) [58].

2.2.2 am atmospheric tool

Another tool for the radiative transfer theory analysis is am atmospheric model [59]. am offers radiative transfer calculations considering electromagnetic wave propagation across the atmosphere covering wavelengths starting from microwave up to sub millimeter bands. Specifically, am can be employed to model any problem involving a narrow beam propagation across a series of segment paths with a user-specified atmospheric composition, temperature and pressure considering local thermodynamic equilibrium. Various spectra that can be obtained using the am tool include thermal emission, absorption and excess delay.

2.2.3 Line by Line Radiative Transfer Model (LBLRTM)

For obtaining realistic transmittance values at different altitudes, in this thesis, Line by Line Radiative Transfer Model (LBLRTM) tool is employed. LBLRTM is based on the Fast Atmospheric Signature Code (FASCODE) program. The key features of LBLRTM are arbitrary good spectral resolution, inclusion of both foreign and self-broadened continuum models of water vapors, and extra continuum models provided for carbon dioxide, nitrogen, oxygen and ozone gases. The minimum supported spectral limit in the LBLRTM is 0.75 THz, with the spectral resolution of 0.01 cm^{-1} (0.3 GHz) [50]. Identical to the HITRAN on the Web, LBLRTM employs the Voigt line shape together with a personalized algorithm for linearly combining the line approximation functions. Based on predefined atmospheric profiles, transmitter and receiver atmospheric altitudes (in km), zenith angle (in degrees) between the transmitter and receiver, LBLRTM calculates various atmospheric parameters such as transmittance, radiance and optical depth. Hence, LBLRTM provisions support for analyzing the atmospheric mean transmittance across various altitudes, unlike HITRAN on the Web [56] which is traditionally employed for the atmospheric analysis at the sea-level. LBLRTM has been widely considered as one of the best models for the atmospheric based analysis typically used in radiative transfer applications, consisting of a wide spectral range, extending from the sub-millimeter to the ultra-violet band. The Voigt line shape is employed together with an algorithm for linearly combining functions for line approximation. In [33], the atmospheric attenuation is investigated in detail using LBLRTM for the frequency range [0.1-100 THz] under pristine conditions. It is shown in [33] that LBLRTM can provide good atmospheric predictions for earth-to-space links. Earlier in the literature, LBLRTM has been employed for the transmittance-based atmospheric analysis [33, 50, 51]. In this thesis, prior to employing the LBLRTM for obtaining realistic transmittance values at various altitudes, directions of communication and ranges, in the following, we validate LBLRTM with two experimental results from the literature.

2.2.4 LBLRTM Validation with Experimental Results

In this thesis, the LBLRTM is validated against the two existing experimental measurement results in [60] over 0.75-2 THz and in [61] over 1-3 THz. For the validation purposes, we obtain the power transmittance values by taking the square of the am-

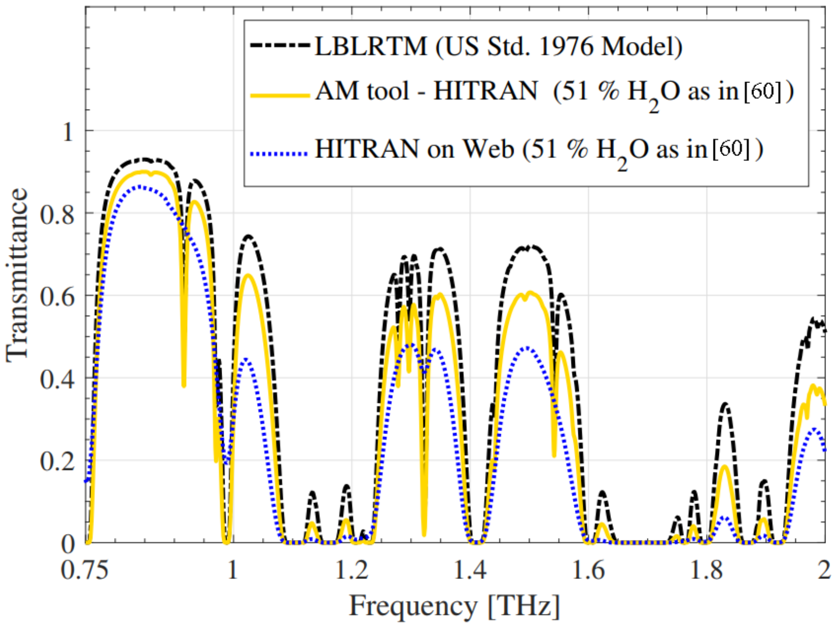

Figure 2.1 LBLRTM comparison with the am atmospheric model and HITRAN on the Web. Communication at sea-level at transmission distance (d) = 6.18 m as in [60].

Table 2.1 Simulation parameters as in [60].

LBLRTM	**am atmospheric model**	**HITRAN on Web**
US Std. 1976 Model Wavenumber V1 = 25.01731 cm^{-1} Wavenumber V2 = 66.71282 cm^{-1} H1, H2 = 0 km ZANGLE = 90 deg RANGEF = 0.00618 km	f 750 GHz 2000 GHz 50 MHz T0 296 K layer P 1013.25 mbar T 21 C h 6.18 m column h20 RH %51	Gas mixture = 51 % H20 Min. Wavenumber, WNmin = 25.01731 cm^{-1} Max. Wavenumber, WNmax = 66.71282 cm^{-1} Temperature, T = 296 K Pressure, P = 1 atm Cut-off on Intensity, Scut = 1.0E-28 cm/mol Line profile = Voigt Wing (W), #halfwidths = 50 App.function (AF) = No influence on the device Optical path, L = 6.18 m

plitude transmission (or transmittance) values presented in [60] and [61]. To further observe the accuracy of the LBLRTM with other existing radiative transfer tools, we compare the LBLRTM with two High-resolution Transmission molecular absorption database (HITRAN) [62] implementations, using the am atmospheric model [59] and the HITRAN on the Web [56] as the two theoretical benchmarks, since the THz-band has been initially assessed at the sea level using HITRAN [17, 18]. It is to be noted here that we can compare LBLRTM with HITRAN over the entire considered THz-band (0.75-10 THz). However, THz-band communication is a new topic in the research community and the experimental works found in the literature are up to 3 THz. Therefore, we have included the am atmospheric model and HITRAN on the Web results only up to 3 THz. The simulation parameters of the three-considered tools are provided in Table 2.1 as in [60] and in Table 2.2 as in [61].

Figure 2.1 illustrates the transmittance as a function of frequency (0.75-2 THz) at

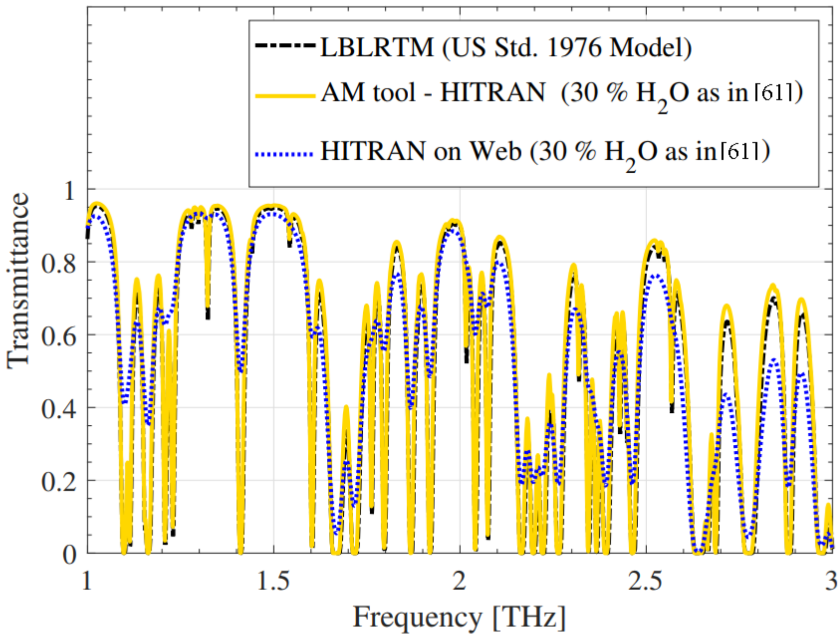

Figure 2.2 LBLRTM comparison with the am atmospheric model and HITRAN on the Web. Communication at sea-level at transmission distance (d) = 1 m as in [61].

d = 6.18 m as considered in Figure 5 of [60]. The transmittance curves obtained using the LBLRTM are provided as the black-line, whereas the HITRAN-based transmittance (51 % H_2O as in [60]) are obtained via the am atmospheric model [59] and HITRAN on the Web [56] as the yellow-line and blue-dashed line, respectively. Table 2.3 summarizes the mean and standard deviation of absolute errors ($\mu(|\epsilon|)$ and $\sigma(|\epsilon|)$) of the three-considered tools with respect to the experimental data [60]. It can be seen that LBLRTM offers a reasonable $\sigma(|\epsilon|)$, while the am atmospheric model offers the least $\mu(|\epsilon|)$ and $\sigma(|\epsilon|)$ for the considered setting as compared to LBLRTM and HITRAN on the Web. This shows that LBLRTM can be considered for a reasonable theoretical approximation as compared to both the am atmospheric model and HITRAN on the Web.

Figure 2.2 depicts the transmittance vs. frequency (1-3 THz) at $d = 1$ m as provided in Figure 4 of [61], whereas $\mu(|\epsilon|)$ and $\sigma(|\epsilon|)$ of the three considered tools are given in Table 2.3. It can be observed that the LBLRTM curves closely approximate the experimental data points, showing a slight better $\mu(|\epsilon|)$ and $\sigma(|\epsilon|)$ of 0.1184 and 0.1253, respectively, as compared to that of the am atmospheric tool, which are 0.1601 and 0.1402, respectively. HITRAN on the Web based transmittance depicts the highest deviations. This shows that the LBLRTM can be considered as a reliable tool for approximating the transmittance of real-world THz-band communication scenarios.

Table 2.2 Simulation parameters as in [61].

LBLRTM	am atmospheric model	HITRAN on Web
US Std. 1976 Model Wavenumber V1 = 33.35641 cm^{-1} Wavenumber V2 = 100.06923 cm^{-1} H1, H2 = 0 km ZANGLE = 90 deg RANGEF = 0.001 km	f 1000 GHz 3000 GHz 50 MHz T0 296 K layer P 1013.25 mbar T 23.6 C h 1 m column h20 RH %30	Gas mixture = 30 % H20 Min. Wavenumber, WNmin = 33.35641 cm^{-1} Max. Wavenumber, WNmax = 100.06923 cm^{-1} Temperature, T = 296.6 K Pressure, P = 1 atm Cut-off on Intensity, Scut = 1.0E-28 cm/mol Line profile = Voigt Wing (W), #halfwidths = 50 App.function (AF) = No influence on the device Optical path, L = 1 m

In the subsequent sections, we assess the THz-band communication using the LBLRTM at the sea-level up to the near space by unifying the study over 0.75-10 THz, although the LBLRTM is validated with the experimental work up to 3 THz. This is because of the LBLRTM shows reasonable theoretical approximation with the am atmospheric model and HITRAN on the Web, and it offers the provision to assess THz-band transmittance at variable altitudes, zenith angles, and transmission distances [50, 51, 63], from the sea-level up to the space [33].

Table 2.3 Mean and standard deviation of the absolute error from the experimental data as in [60] and [61]: LBLRTM, am atmospheric model (HITRAN) and HITRAN on the Web.

	Experimental Validation with [60]			**Experimental Validation with [61]**		
	LBLRTM	**am (HITRAN)**	**HITRAN on Web**	**LBLRTM**	**am (HITRAN)**	**HITRAN on Web**
$\mu(\lvert\epsilon\rvert)$	0.1359	0.0629	0.0877	0.1184	0.1601	0.1961
$\sigma(\lvert\epsilon\rvert)$	0.0896	0.0776	0.0821	0.1253	0.1402	0.2078

2.2.5 Modeling of Atmospheric Conditions Using LBLRTM

In this section, we investigate the variation of atmospheric conditions, i.e. , temperature, pressure, and water vapor concentration as a function of altitude, considering their implications for aerial communication scenarios by employing LBLRTM.

We model THz band communications at varying atmospheric altitudes by taking the leverage of LBLRTM, which also provides six weather profiles, namely, Tropical, Mid Latitude Summer, Mid Latitude Winter, Sub Arctic Summer, Sub Arctic Winter and US Standard 1976. Fig. 2.3(a) shows the atmospheric temperature and pressure variations as the function of the altitude. It can be observed that among all of the six weather profiles, the temperature (left y-axis) decreases drastically as the altitude increases, particularly across the altitudes of 10-20 km, making the THz band an ideal candidate for establishing Tbps communication links among cruising jet planes, UAVs and HAPs. Moreover, it can also be seen that the atmospheric pressure (right y-axis) follows a logarithmic relation with the altitude. The pressure is at the maximum level at the sea-level (i.e. , 100 kPa) which is trivial, as the

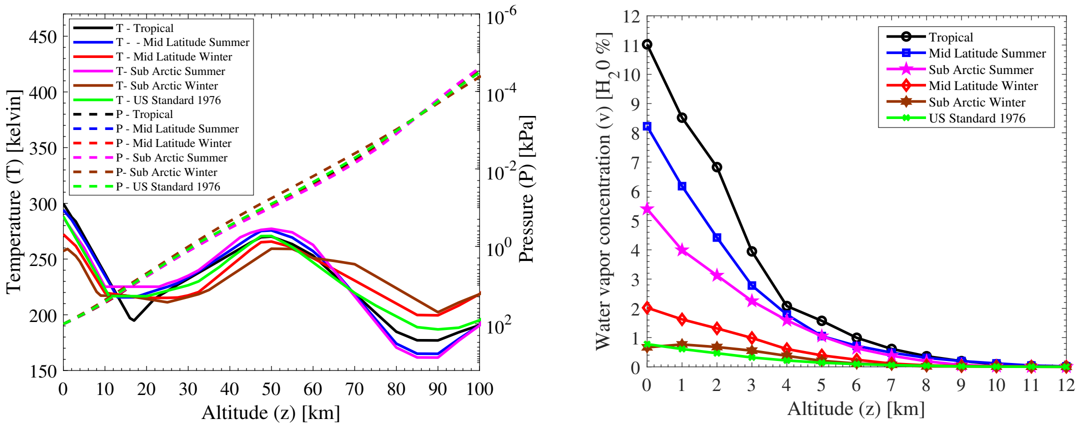

(a) (b)

Figure 2.3 Variations in the atmospheric temperature and pressure (a), and water vapor concentration (b) across the earth's atmosphere for six different LBLRTM weather profiles.

maximum atmosphere is concentrated at the sea-level. As the altitude increases from 0 km up to about 10 km, the pressure decreases by an order of magnitude, i.e. , from 100 kPa to nearly 10 kPa. This condition also favors high rate links in the order of Tbps among cruising jet planes, UAVs and HAPs. From the 30 km altitude on wards, the temperature starts rising again up to 50 km altitude, making transmittance observed across these altitudes to be more colored. Finally, reaching at the altitude of 90 km and above, the temperature drops to lowest levels, observing the negligible pressure levels, highly favoring Tbps Inter Satellite Links (ISLs).

Fig. 2.3(b) illustrates the influence of altitude on the water vapor concentration across the earth's atmosphere for the six weather profiles in LBLRTM. The maximum water vapor concentration is observed at the sea-level for all of the six weather profiles with the tropical weather profile offering the highest concentration of 11.02 % and the subarctic winter profile being the lowest at 0.667 %. As the altitudes reaches 1 km, the water vapor concentration decreases exponentially, promising the drone communications over the THz band with the communication links in the order of 100 s of Gbps. At the altitude of 4 km, all of the three weather profiles offering the highest concentrations i.e. , Tropical, Mid Latitude Summer and Mid Latitude Winter converge to a lower water vapor concentration of merely 2 %. This exponential decreasing trend continues till the 6 km altitude, where all of the six weather profiles exhibit the water vapor concentration of less than 1 %. Interestingly, for the higher altitudes reaching 12 km, all of the six weather profiles offer negligible water vapor concentration, i.e. , nearly 0 %. This shows that the THz band can be highly leveraged for communication among aerial vehicles by the reduced water vapor concentrations at higher altitudes. For instance, aerial vehicles flying at and above 10 km altitudes, such a cruising jet planes across 10-12 km, UAVs and HAPs flying across 16-22 km, and even beyond i.e. , among ISLs between communicating satellites and cubesats [64] across and above 99 km. It is to be noted here that although LBLRTM provisions the radiative transfer analysis for the altitudes up to 120 km, only the altitudes of up to 12 km are provided in Fig. 2.3(b), as the water vapor concentrations above the 12 km altitude are negligible. Having presented the THz absorption loss, efficacy of LBLRTM and THz propagation in the atmosphere, in the following chapter, THz path loss analysis for aerial vehicles is presented followed by the total usable bandwidth analysis, in detail.

Chapter 3

TERAHERTZ COMMUNICATIONS AT VARIOUS ATMOSPHERIC ALTITUDES

As discussed in Chapter 2, wireless communication over the THz band (0.75-10 THz) highly suffers from atmospheric absorption loss at the sea-level. Hence, the considered transmission distances are usually in the order of a few meters [4]. In this chapter, we investigate the feasibility of employing the THz band (0.75-10 THz) for communications at different altitudes among aerial vehicles, and we evaluate how THz communications can leverage from the lower atmospheric gas concentrations (mainly water vapor molecules) at high altitudes. We consider four aerial communication cases, namely, Drone-to-Drone (Dr2Dr), Jet plane-to-Jet Plane (J2J), Unmanned Aerial Vehicle to Unmanned Aerial Vehicle (U2U), and Space to Space S2S communication as shown in Figure 3.1. For performance analysis, the open source LBLRTM is utilized for realistically calculating the transmittance values for each case. Thereafter, the absorption loss values are derived and are subsequently incorporated with the spread loss for computing the total path loss. Conclusively, the total usable bandwidths across the THz band (0.75-10 THz) are computed for the each case by considering total path loss thresholds corresponding to the practical transmit powers, antenna gains, Signal-to-Noise Ratio (SNR) level.

We present the THz band communications for the four practical aerial vehicle communication cases as depicted in Figure 3.1 by considering various transmitter-receiver orientations starting from vertical-up towards vertically-down communi-

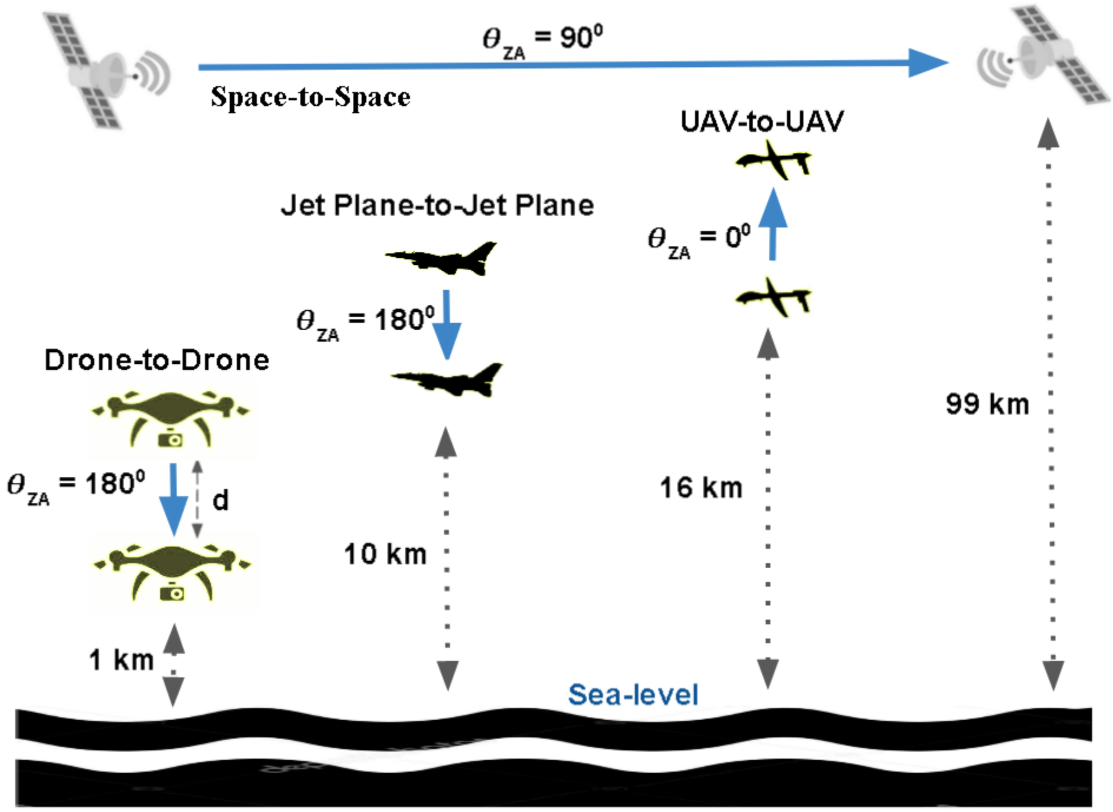

Figure 3.1 Aerial vehicle communication cases considered in the chapter and visual illustration of the zenith angles between Tx and Rx aerial vehicles.

cations. As a bench mark, we also include the THz band communication at the sea-level.

3.1 Path Loss Model

For the path loss analysis, the radiative transfer theory is employed usingLBLRTM for computing the EM wave attenuation as it propagates across the atmosphere. This attenuation is specifically due to the molecular absorption in the atmosphere. For doing so, we need to compute the fraction of EM radiation which is passed through the medium after experiencing the absorption, known as the medium's transmittance $\tau(f, d)$. According to the Beer-Lambert's Law [18]:

$$\tau(f, d) = \frac{P_0}{P_i} = e^{-k(f)d} \ , \tag{3.1}$$

where f denotes the EM wave's frequency, d is the transmission distance, P_0 and P_i refers to the passed and incident EM powers, while k is the frequency-dependent medium absorption coefficient. Mathematically, $k(f)$ (in m^{-1}) is defined as:

$$k(f) = \sum_{i,g} \frac{p}{p_0} \frac{T_{STP}}{T} Q^{i,g} \sigma^{i,g}(f) \ , \tag{3.2}$$

where p and p_0 denote the system's pressure and reference pressure, T and T_{STP} are the system's temperature and standard temperature and pressure. $Q^{i,g}$ and $\sigma^{i,g}$ are the molecular volumetric density (in $molecules/m^3$) and absorption cross-section of isotopologue i of gas g. A detailed analysis covering the molecular absorption can be found in [18].

$A_{abs}(f,d)$ provides the absorption loss experienced by the THz through the atmospheric propagation. This absorption loss is mainly due to the water vapor molecules in the atmosphere, and can be derived from the transmittance $\tau(f,d)$ prior obtained by using LBLRTM, as [17, 18, 33]:

$$A_{abs}(f,d) = \frac{1}{\tau(f,d)} = e^{k(f)d} \ , \tag{3.3}$$

and in dB scale,

$$A_{abs}(f,d)[dB] = k(f)d10log_{10}e \ . \tag{3.4}$$

Since LBLRTM provides the transmittance results $\tau(f,d)$ against a given setting, (3.3) can be used to obtain the absorption losses $A_{abs}(f,d)$ directly using $\tau(f,d)$ for a given transmission distance. $k(f)$ can be obtained numerically from (3.3), based on the obtained $\tau(f,d)$ values using the LBLRTM as [33, 65]:

$$\ln \frac{1}{\tau(f,d)} = \ln e^{k(f)d} = -\ln \tau(f,d) = k(f)d \ . \tag{3.5}$$

Therefore,

$$k(f) = \frac{-\ln \tau(f,d)}{d} \ [m^{-1}] \ . \tag{3.6}$$

The total path loss is obtained as the sum of the free space spread loss and the absorption loss as:

$$A_{pl}(f,d)[dB] = A_{spread}(f,d)[dB] + A_{abs}(f,d)[dB] \ . \tag{3.7}$$

Here, $A_{spread}(f,d)$ denotes the free space spread loss due to the attenuation experienced by the THz wave while propagating through the atmosphere and the loss due to the isotropic antenna, which is obtained as [18]:

$$A_{spread}(f,d)[dB] = 20log_{10}\left(\frac{4\pi f d}{c}\right) \ . \tag{3.8}$$

In this work, LBLRTM is used to obtain the transmittance values, $\tau(f,d)$ in (3.3) at different altitudes for the aerial vehicle communication cases, thereby obtaining the absorption loss $A_{abs}(f,d)[dB]$ in (3.4). In the following, we provide the path loss analysis at various atmospheric altitudes, in detail.

3.2 Path Loss Analysis At Different Atmospheric Altitudes

3.2.1 Sea-Level Communication

As our benchmark case, we consider the THz band communications at the sea-level (altitude = 0 km) at d = 1 m, 10 m and 50 m. The reason here for not including the THz band lower than 0.75 THz is the limitation of the LBLRTM as it has been stated earlier in Section 2.2.3.

The transmittance curves of the sea-level communication case are provided in the Figure 3.2a. It can be seen that by increasing the transmission distance, the transmittance decreases substantially due to huge absorption losses at the sea-level. The first effective range for the THz band communication at 1 m seems to be 0.7600-0.9828 THz (greater than 70 %), which closely corresponds to the fourth transmission window ([0.77-0.92 THz]) as identified in [4] at 1 m distance. The reason for a broader transmission window obtained here via LBLRTM can be justified by the fact that the HITRAN-based results seem to be more attenuated in contrast to the LBLRTM results as already discussed in Section 2.2.4. At 10 m, the observed THz band having the transmittance values above 80 % are: 0.79-0.9 THz and 0.92-0.94 THz, while the absorption effect is much greater for the higher frequencies. For d = 50 m, the maximum transmittance observed (55 %) at the THz frequency of 0.8474 THz. The transmittance values of greater than 50 % spans from 0.8165 THz to about 0.8904 THz. For the higher frequencies from 0.9687-9.154 THz, the absorption effect is dominant, causing the transmittance values to remain less than 20 %. Figure 3.2b provides absorption losses (truncated at 200 dB to avoid masking of the feasible THz band transmission windows) case obtained using the transmittance results in Figure 3.2a. Clearly, the absorption loss values are huge enough particularly for the higher THz frequencies, showing that the losses contributed by the absorption are highly affecting the communication across the THz band. At 0.917 THz (d = 50 m), the absorption loss is 24.19 dB, which is 19.354 dB greater as compared to the absorption loss at $d = 10$ m. The total path loss Figure 3.2c shows the huge absorption loss contributions to the spread loss. The mean total path variations with respect to the zenith angle, θ_{ZA} for the sea-level communication with transmission distances of 1 m, 10 m and 50 m are provided in Figure 3.2d, showing that there is an increasing trend in the mean total path loss as d increases, while there is no considerable effect of employing the vertically-up ($\theta_{ZA} = 0^0$), horizontal ($\theta_{ZA} = 90^0$) or vertically-down ($\theta_{ZA} = 180^0$) communication on the mean total path loss. This is due to the homogeneity in the atmosphere across the sea-level.

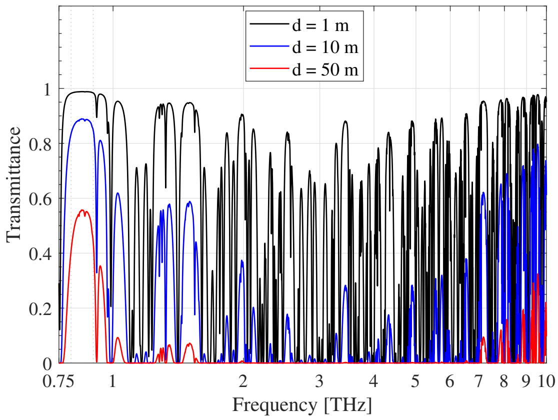

(a)

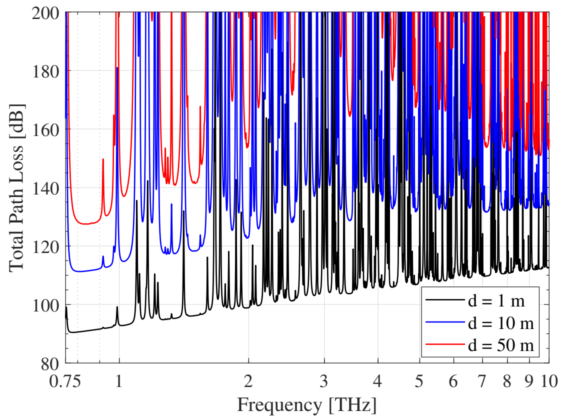

(c)

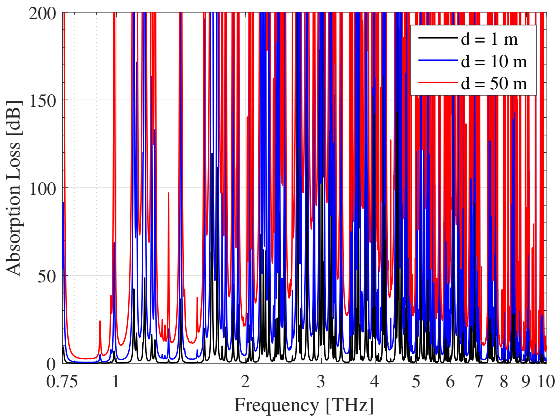

(b)

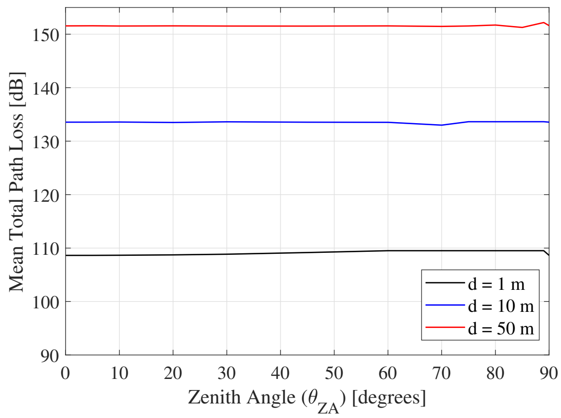

(d)

Figure 3.2 Sea-level communication: $d = 1$ m, 10 m and 50 m, $\theta_{ZA} = 0^0$ (vertically-up). (a) Transmittance vs. Frequency [THz], (b) Absorption Loss [dB] vs. Frequency [THz], (c) Total path Loss [dB] vs. Frequency [THz], and (d) Mean Total Path Loss [dB] vs. Zenith Angle (θ_{ZA}) [degrees].

3.2.2 Drone-to-Drone Communication

As the first aerial communication case, we consider Dr2Dr communications, as drone networks are emerging for many applications, such as military or disaster recovery [66,67], which can leverage THz band communication, providing the high bandwidth for exchanging high resolution images or videos. We consider such a case for Dr2Dr communications over the THz band (0.75-10 THz) where two flying drones are communicating with each other with the transmitter at a fixed altitude of 1 km (Figure 3.1. d = 10 m, 50 m and 100 m are considered [68]. Figure 3.3a shows the transmittance for the Dr2Dr case (d = 10, 50 m and 100 m) with respect to the frequency (0.75-10 THz). On comparing Dr2Dr case of d 10 m with the sea-level communication case at 10 m (Figure 3.2a), it can be observed that the band offering the transmittance values of greater than 80 % is increased. i.e. 0.7824-0.911 THz and 0.9228-0.9563 THz. This is due to the leverage by considering the higher altitude

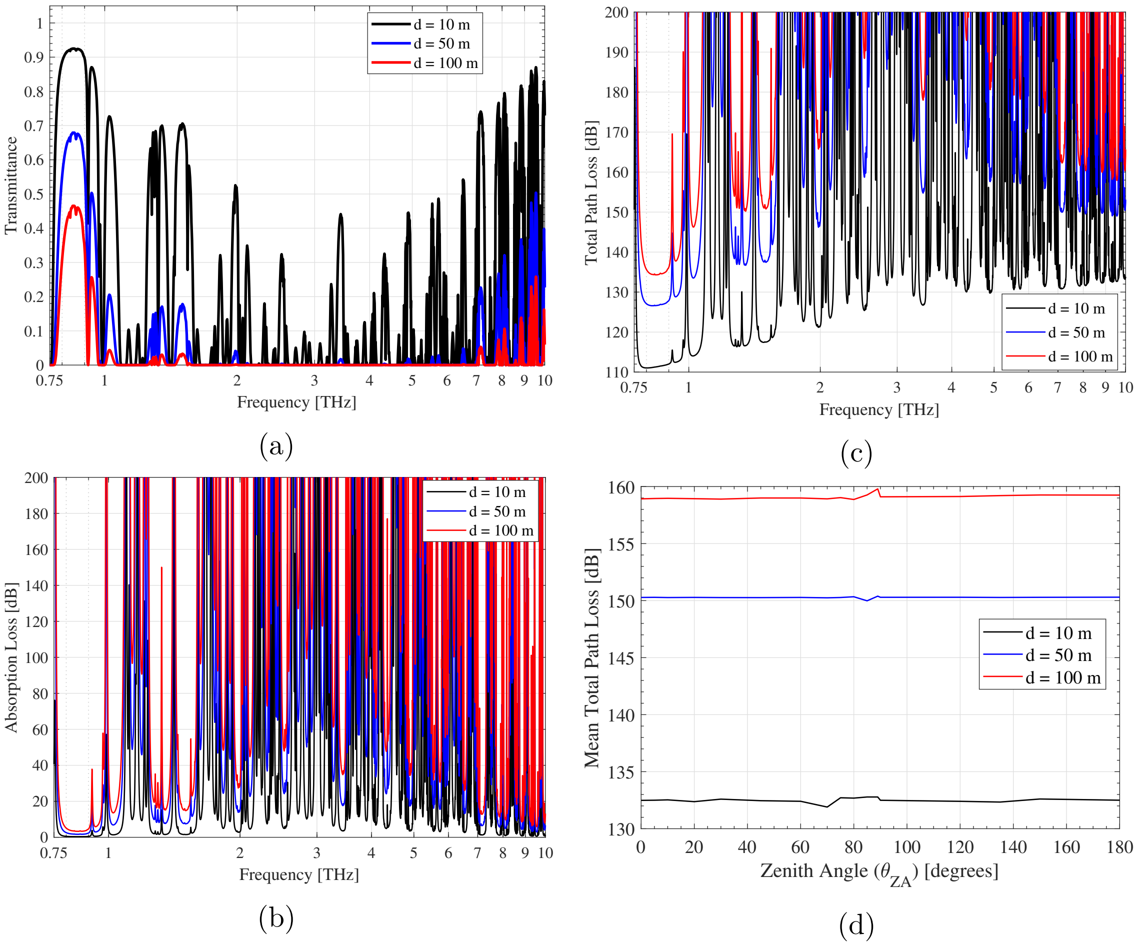

Figure 3.3 Drone-to-Drone communication: d = 10 m, 50 m and 100 m, $\theta_{ZA} = 0^0$ (vertically-up). (a) Transmittance vs. Frequency [THz], (b) Absorption Loss [dB] vs. Frequency [THz], (c) Total path Loss [dB] vs. Frequency [THz], and (d) Mean Total Path Loss [dB] vs. Zenith Angle (θ_{ZA}) [degrees].

of 1 km instead at the sea-level, thereby observing comparatively lower absorption loss values. The transmittance curves for $d = 50$ m with greater than 50 % values become broader as compared to the sea-level communication results in Figure 3.2a. Additionally, a narrow band of 0.9316-0.4995 THz is also offering the transmittance of greater than 50 %. For $d = 100$ m, the highest transmittance value is observed at 0.84 THz, which is 46.55 %. Figure 3.3b. depicts that the absorption loss values for the Dr2Dr case are lower as compared to the sea-level case. Figure 3.3c illustrates that for $d = 100$ m, high antenna gains would be required to overcome huge total path losses, which is trivial that as the transmission distance increases, the total path loss also increases. Furthermore, Figure 3.3d shows that $\theta_{ZA} = 0^0$ (vertically-up) offers the lowest mean total path values followed by 90^0 and 180^0, showing that the THz band communications can be leveraged more by traversing up in the atmosphere, providing high data rate links for multimedia applications which are typically vital in the disaster and military surveillance applications [68]. In contrast to the mean total path loss variations shown in Figure 3.2d, it can be seen that for the Dr2Dr communication with d greater than 50 m, the zenith angle starts influencing the transmission, i.e. the vertically-up communication offers the highest transmittance values as compared to the horizontal communication, followed by the vertically-down communication.

3.2.3 Jet Plane-to-Jet Plane Communication

Another practical case for the THz communications can be among cruising jet planes, which typically fly at altitudes of about 10 km and above , which is the boundary of troposphere and stratosphere [33]. We evaluate such a case, where a jet plane is cruising at an altitude of 10 km, transmitting to another flying plane at $d = 500$ m, 1 km and 2 km.

Figure 3.4a depicts the transmittance for the jet plane communication case ($d =$ 500 m, 1 km and 2 km). It can be observed that the transmittance curves for all the three cases are mostly above 80 % for approximately the entire THz range [i.e. 0.75-10 THz] with intermittent absorption-based dips. This is because the water vapor concentration at the high altitude of 10 km are extremely low as compared to the lower altitudes, making the THz range (0.75-10 THz) a viable communication band among jet plane-to-plane communications. By increasing d from 500 m to 2 km, the losses increase thereby decreasing the overall transmittance. For $d = 2$ km, the THz band (0.75-10 THz) still offers high transmittance values, maintaining values greater than 80 % with the intermediate absorption loss-based dips. It can be clearly seen from Figure 3.4b that observed absorption loss offers various bands showing very minute losses. The first such band is across 0.755-0.986 THz. It is evident that due to very low absorption loss contributions over the band (0.75-10 THz), the total path loss values in Figure 3.4c follow the free space spread loss values with a few sharp absorption peaks contributions from Figure 3.4c. $d = 1$ km still offers low total absorption bands. The huge losses incurred due to larger propagation distance of 1 km and 2 km should be countered by provisioning highly directional antennas (high gains) at the transmitter and receiver of the communicating jet planes. Furthermore, the zenith angle-based mean total path loss variations in Figure 3.4d illustrate that $\theta_{ZA} = 0^0$ (vertically-up) offers the lowest mean total path loss (i.e. highest transmittance), followed by 90^0 (horizontal) and 180^0 (vertically-down). This also shows that establishing THz band communications towards a higher altitude (vertically-up from 10 km to 12 km) offers the lowest absorption loss values than communicating over the same altitude (horizontally at 10 km) or even worse towards the lower altitude (vertically-down from 10 km to 8 km). It is to be

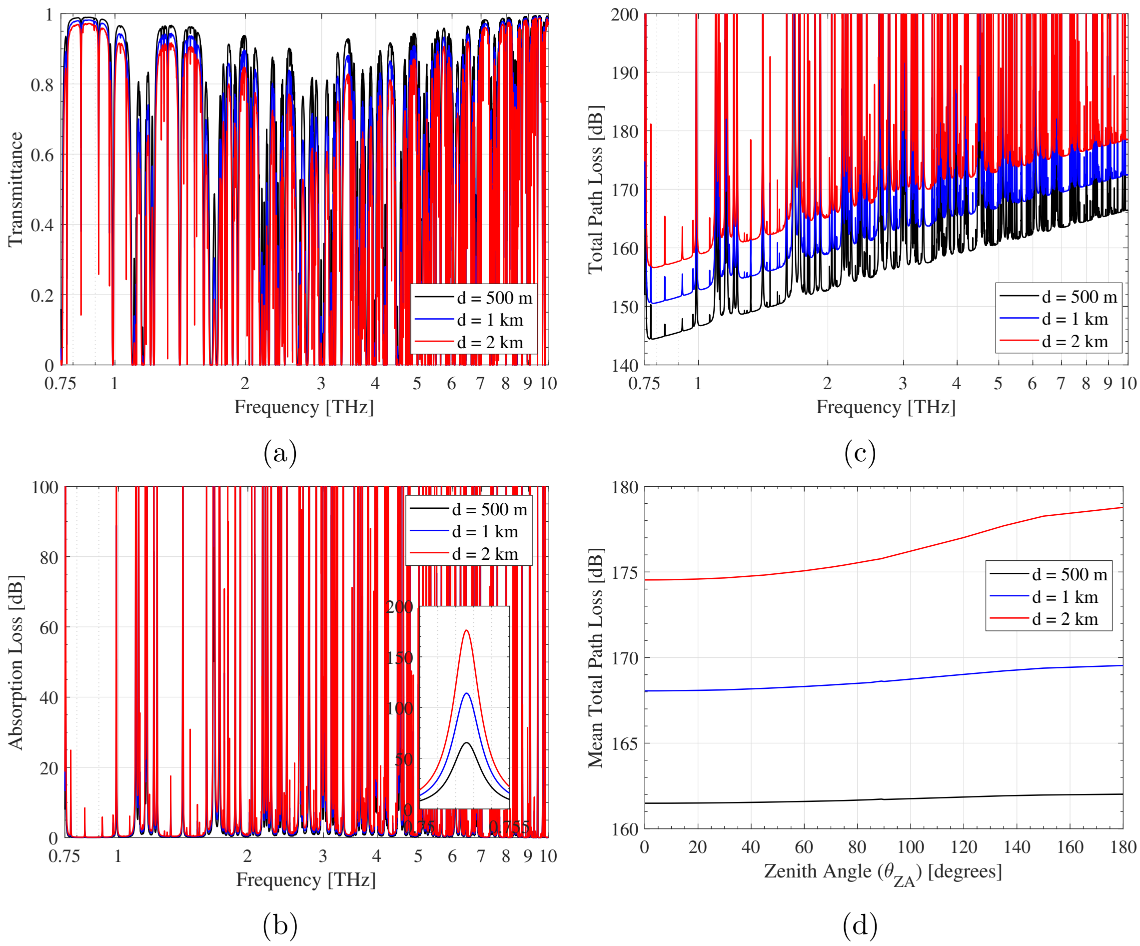

Figure 3.4 Jet Plane-to-Jet Plane communication: $d = 500$ m, 1 km and 2 km, $\theta_{ZA} = 0^0$ (vertically-up). (a) Transmittance vs. Frequency [THz], (b) Absorption Loss [dB] vs. Frequency [THz], (c) Total path Loss [dB] vs. Frequency [THz], and (d) Mean Total Path Loss [dB] vs. Zenith Angle (θ_{ZA}) [degrees].

noted that here in the J2J case, the transmittance is highly influenced by the zenith angle variations as compared to the sea level and Dr2Dr communication cases.

3.2.4 UAV-to-UAV Communication

THz band can provide high speed communication links among high-altitude UAVs, which usually fly at altitudes in the order of several kilometers [69]. We consider such a case for two UAVs communicating over the THz band (0.75-10 THz), where the transmitting UAV is flying at an altitude of 16 km, while the receiving UAV is considered at the transmission distances of 500 m, 1 km and 2 km from the transmitter. The altitude of 16 km, which is in fact the stratospheric region of the atmosphere [33], is considered to be highly suitable for the THz communications, as the water vapor concentrations are negligible at the altitudes of 16 km and above [70].

Figure 3.5a provides the transmittance values for the U2U communication case, $d = 500$ m. As compared to the J2J case corresponding to the identical transmission distance of 500 m, the transmittance values of the U2U case are much higher, reaching mostly 99-100 % together with extremely sharp transmittance dips due to the absorption losses. The transmittance values over the THz band (0.75-10 THz) remain mainly above 90 % making the band still feasible for the greater communication distance of 1 km. The absorption losses in Figure 3.5b show near negligible effect due to the higher atmospheric altitude of 16 km. The total path loss in Figure 3.5c confirms the negligible absorption effect, i.e. nearly free space spread losses are observed together with highly sharp absorption peaks. The results show that at the altitude of 16 km, U2U communications can still employ the THz band (0.75-10 THz) for the communication distance of up to 2 km, provided that adequate high antenna gains are supported to overcome the free space spread losses, while transmitting over the lower absorption loss bands. It is to be noted here that the effect of varying the zenith angle (i.e. 0^0 up to 180^0) on the mean total path loss is observed to be negligible for the U2U cases of $d = 500$ m up to 2 km, as illustrated in Figure 3.5d.

3.2.5 Space to Space S2S Communication

The Space to Space boundary normally referred to as the Karman Space Boundary starts at about 100 km [33, 71]. From this altitude upwards, space regulations are applied by various telecommunication regulatory bodies. Since the altitudes of low perigee elliptical orbit satellites can be as low as 80-90 km [71], for this case, we consider a possible satellite communication over the THz band (0.75-10 THz), where a very low perigee satellite at 99 km is transmitting to another satellite at $d = 500$

m, 1 km and 2 km, as considered in the earlier aerial communication cases.

Figure 3.6a provides the transmittance curves for the Space to Space S2S case, highlighting that the transmittance curves for the distance of 500 m over the entire THz band (0.75-10 THz) are always greater than 99.965 %, confirming the approximate atmospheric absence at the altitudes of 99 km and above. Figure 3.6b re-iterates the fact of the lack of atmospheric absorption at 99 km as the absorption losses are approximately negligible at such altitudes. The results show that even by increasing the transmission distance from 500 m to 1 km, the transmittance values (Figure 3.6a) over the entire THz band (0.75-10 THz) are still greater than 99.27 %. Even for $d = 2$ km, the minimum transmittance values over the the entire THz band (0.75-10 THz) remain greater than 98.3 %, promising the THz band to be a viable communication band candidate for the satellite communications [72], particularly among ISLs [73, 74] supporting links in the order of Terabits per sec [Tbps].

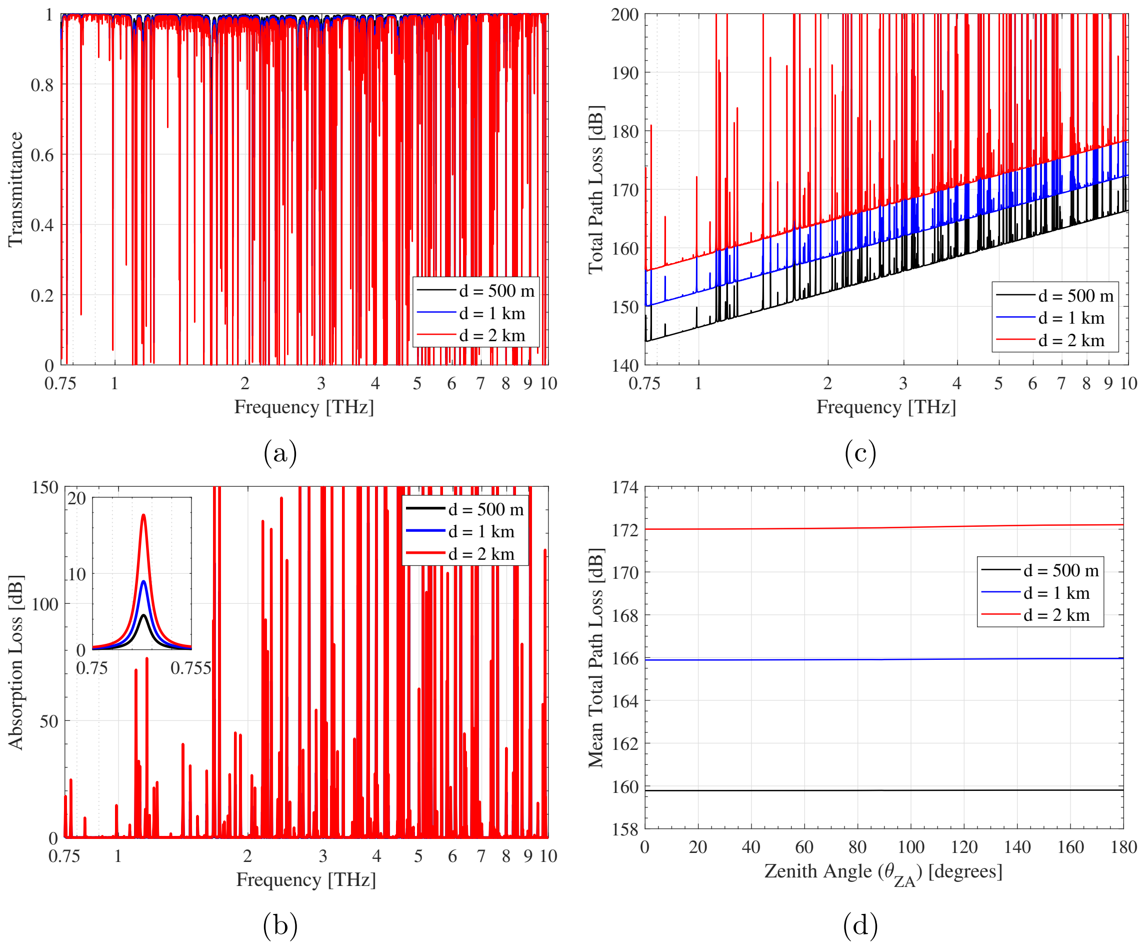

Figure 3.5 UAV-to-UAV communication: $d = 500$ m, 1 km and 2 km, $\theta_{ZA} = 0^0$ (vertically-up). (a) Transmittance vs. Frequency [THz], (b) Absorption Loss [dB] vs. Frequency [THz], (c) Total path Loss [dB] vs. Frequency [THz], and (d) Mean Total Path Loss [dB] vs. Zenith Angle (θ_{ZA}) [degrees].

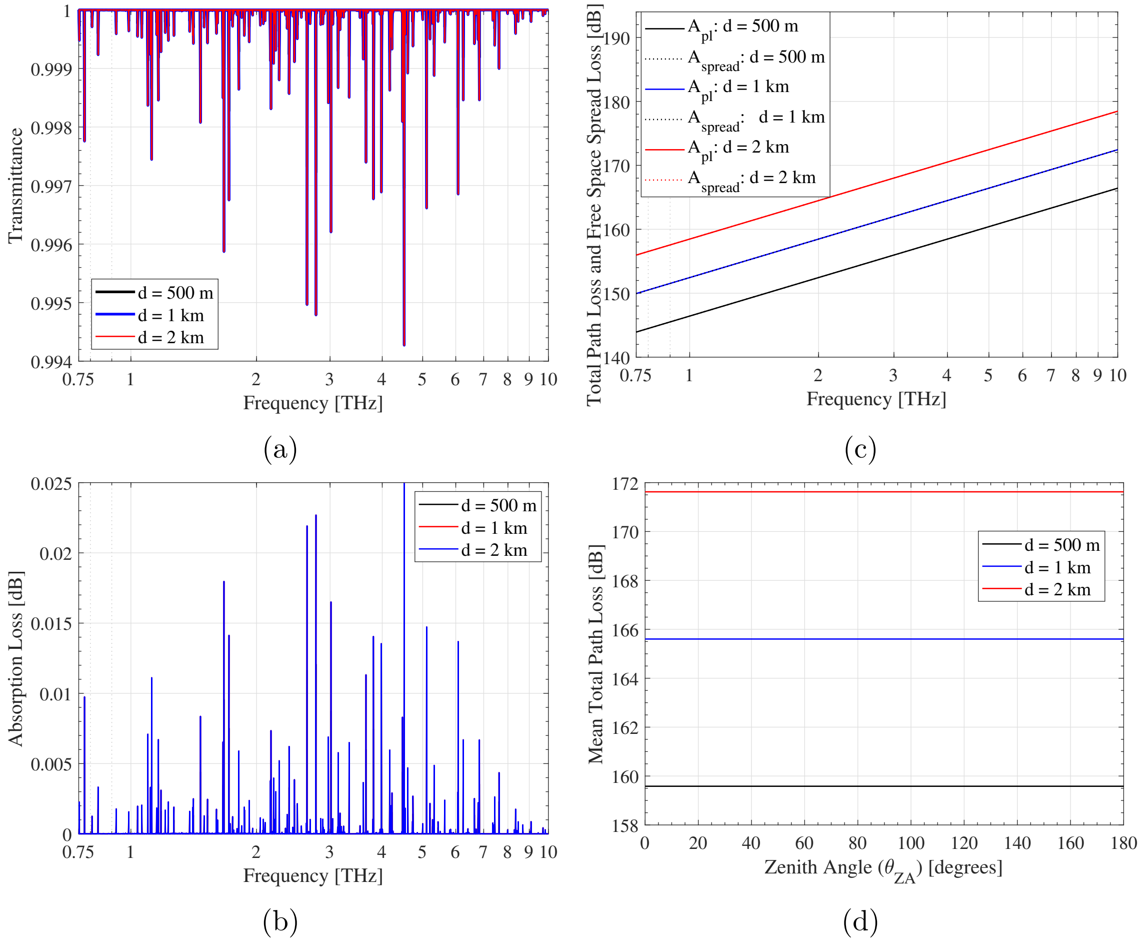

Figure 3.6 Space to Space S2S communication: d = 500 m, 1 km and 2 km, θ_{ZA} = 0^0 (vertically-up). (a) Transmittance vs. Frequency [THz], (b) Absorption Loss [dB] vs. Frequency [THz], (c) Total path Loss [dB] vs. Frequency [THz], and (d) Mean Total Path Loss [dB] vs. Zenith Angle (θ_{ZA}) [degrees].

Moreover, these high rate links can also be realized among airborne high altitude platforms and orbiting satellites [32], which can provide an intermediate relay link between the satellite and the ground station networks. Results presented in this section can also be used as a benchmark for the CubeSats [64, 74], which is a new and innovation satellite technology. Figure 3.6c illustrates that the the Space to Space S2S communication case exhibit merely the free space spread loss values, whereas the effect of the zenith angles over the mean total path loss is seen to be negligible in Figure 3.6d, identically to the U2U case.

3.3 Total Usable Bandwidth Analysis

In this section, we obtain total usable bandwidth for each of the four aerial vehicle communication case as well as for sea-level by considering the vertically-up communication (i.e. $\theta_{ZA} = 0^0$). As the first step, we compute Signal-to-Noise Ratio (γ) as:

$$\gamma = P_{tx} + G_{tot} - A_{pl} - P_n \ , \tag{3.9}$$

where P_{tx} is the transmit power level, which is equally-distributed across all bands, $G_{tot} = G_{tx} + G_{rx}$ refers to the total transmit and receiver antenna gains, A_{pl} is the total path loss from (3.7), while the P_n is the noise power level. Following the approach as in [75, 76], we compute P_n by considering the bandwidth, B equal to the spectral resolution of the LBLRTM, 0.3 GHz as:

$$P_n = k_B T B \ . \tag{3.10}$$

Here k_B corresponds to the Boltzmann constant $= 1.38E - 23 \ m^2 kgs^{-2} K^{-1}$ and T is the thermal noise temperature in kelvin. By considering $T = 293 \ K$, (3.10) in dBm becomes,

$$P_n[dBm] = -174 + 10log_{10}B \ = -89.23 \ dBm \ . \tag{3.11}$$

In this chapter, we assume the constant noise model in (3.10) and (3.11). The above assumption of considering the bandwidth equal to the LBLRTM's spectral resolution means that, irrespective of the total available bandwidth across the considered THz band (0.75-10 THz), we assess several fractional channels, each of them has a bandwidth of 0.3 GHz [75].

It is worth-mentioning here that in this work, γ values are considered to be at the front of the receiver. In regards to the practical THz receiver design, Noise Figure (NF) should also be introduced in (3.9). For instance, typical NF values considered in the literature for THz band receivers vary from 0 dB (ideal receiver) to 9.56 dB [77]. Hence, for practical THz receivers, adding (in dB) the NF contribution with P_n into (3.9) would result in a substantial decrease in γ values across the THz band (0.75-10 THz). Therefore, P_{tx} and G_{tot} values should be adjusted/increased accordingly to achieve acceptable γ levels.

For successful communication, SNR, γ should be above a given threshold SNR, γ_{th}. In other words,

$$\gamma \geq \gamma_{th} \ . \tag{3.12}$$

Subsequently, the maximum acceptable path loss, namely path loss threshold,

$A_{pl}^{th}(f,d)$ can be computed as [76]:

$$A_{pl}^{th}(f,d)[dB] = P_{tx} + G_{tot} - \gamma_{th} - P_n \ . \tag{3.13}$$

The path loss threshold for the sea-level communication as well as for the four atmospheric altitude cases are obtained using (3.13) based on the transmit power, gain and SNR threshold as provided in Table 3.1 and noise power from (3.11).

The total usable bandwidth (W_{tot}) is computed as [76]:

$$W_{tot} = \sum_j W_j \ , \ \forall \ j \ where \ A_{pl} < A_{pl}^{th} \ . \tag{3.14}$$

Here, W_j refers to the usable bandwidth across j^{th} band, whose corresponding total path loss values, A_{pl} are less than the total path loss threshold, A_{pl}^{th}. As an example, the computation of W_j for the Dr2Dr communication case for $d = 10$ m is illustrated

Table 3.1 Physical parameters considered in the chapter for the sea-level [76, 78], Dr2Dr [79], J2J [80], U2U [81] and S2S [72, 82] communication cases.

Symbol	Parameter	Value					Unit
		Sea-level	Dr2Dr	J2J	U2U	S2S	
P_{tx}	Transmit power	10	24	37	30	33.6	dBm
G_{tx}	Transmit antenna gain	[0,20,40]					dBi
G_{rx}	Receive antenna gain	[0,20,40]					dBi
γ_{th}	SNR threshold	10					dB
P_n	Noise and interference power	-89.23					dBm

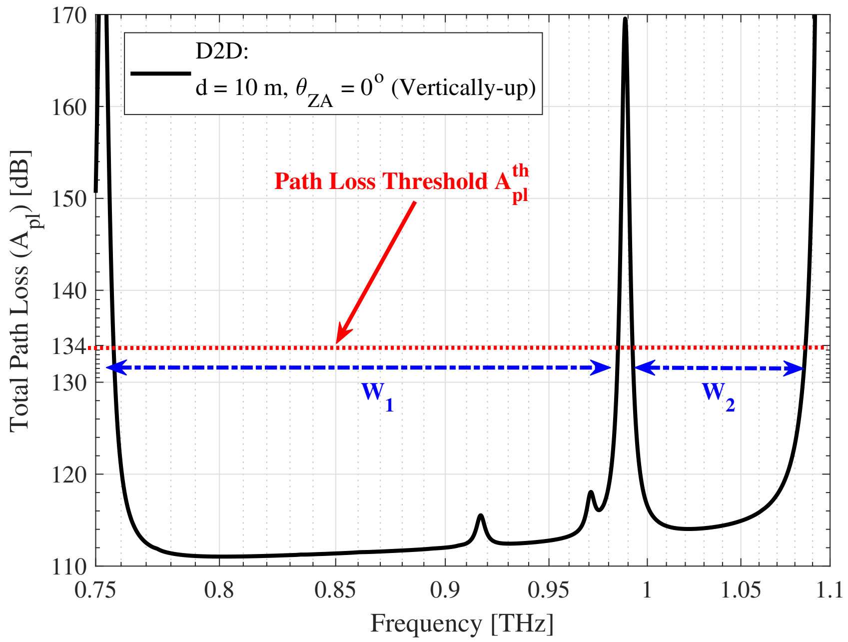

Figure 3.7 Visual illustration of the total usable bandwidth: Total path loss vs. frequency [0.75-1.1 THz] for the Dr2Dr case with d = 10 m and $\theta_{ZA} = 0^0$ (vertically-up.)

in Figure 3.7 (zoomed-in version of Figure 3.3c over the frequency range of 0.75-1.1 THz). Using the parameters of the Dr2Dr communication case from the Table 3.1, A_{pl}^{th} from (3.13) corresponds to 134 dB. Hence, for the considered frequency range, W_{tot} is obtained as the sum of the bandwidths W_1 and W_2. It is to be noted here that this approach only provides the approximate upper bound of the total usable bandwidth. Evaluating the exact total available bandwidth for the each case requires considering the applicability of the state-of-the-art communication systems, which is left as a future study.

Figure 3.8 illustrates the total usable bandwidth for the sea-level communication. Clearly from Figure 3.8a, it can be seen that there is no usable bandwidth available corresponding to the total antenna gain of 0 dBi, since the absorption losses are huge at the sea-level. For 20 dBi total antenna gain, a total usable bandwidth of 0.2184 THz can be obtained at the transmission distance of 8 m, with a bandwidth decrease rate of 496.74 GHz/m. While considering a 40 dBi gain provides a bandwidth of 1.192 THz corresponding to the same distance (i.e. 8 m), while the transmission distance is increased up to 58 m, offering 16.22 GHz, with the decrease rate about 145.29 GHz/m. For a very high total antenna gain of 60 dBi (Figure 3.8b), a transmission distance of up to 100 m can be supported with 0.1732 THz of the bandwidth at 100 m. The observed decrease rate of 85.725 GHz/m for the 60 dBi gain. This shows that the THz band can be employed at the sea-level up to 100 m provided that highly directional antennas are employed.

Figure 3.9 illustrates the total usable bandwidth for the Dr2Dr communication case up to the transmission distance of 100 m as considered in Section 3.2.2. Interestingly,

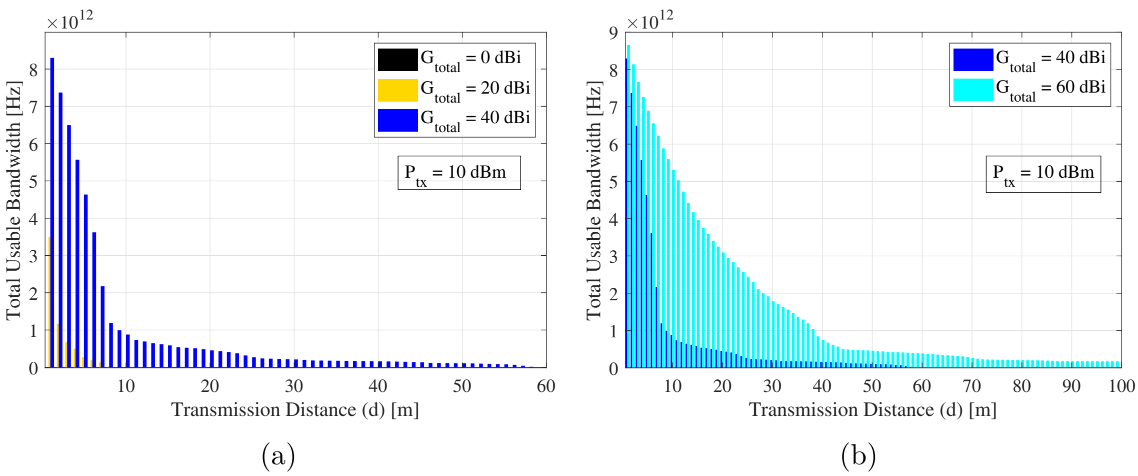

Figure 3.8 Total usable bandwidth for the sea-level communication in the THz band (0.75-10 THz): (a) Total antenna gain = 0 dBi, 20 dBi, 40 dBi, (b) Total antenna gain = 40 dBi, 60 dBi.

it can be seen from Figure 3.9a that unlike the sea-level communication case, even by considering the total antenna gain of 0 dBi, a bandwidth of 82.48 GHz is now usable for a transmission distance of 4 m for the Dr2Dr communications. If the gain is increased up to 20 dBi, a total usable bandwidth of 3.531 THz can be achieved corresponding to the same distance of 4 m. While the identical 20 dBi gain supports the transmission distance of up to 35 m, offering 0.05887 THz (58.87 GHz) of the total usable bandwidth. The bandwidth decreasing rate observed against 20 dBi gain is approximately 244.1 GHz/m. Higher gains of 40 dBi and 60 dBi are considered in Figure 3.9b, showing the potential of the THz band communications among the drone-based communications. It can be observed that providing the 40 dBi gain can support the effective transmission distance up to 100 m, supporting 0.1728 THz of the total usable bandwidth. If we further increase the total antenna gains up to 60 dBi, 8.926 THz, 8.065 THz, 3.745 THz and 1.185 THz of the total usable bandwidths are achievable against the transmission distances of 1 m, 4 m, 35 m and 100 m respectively. The decrease rate against for the 60 dBi gain from 1 m till 100 m is about 78.19 GHz/m.

Figure 3.10 provides the total usable bandwidth for the J2J communication case over the THz band, against the transmission distances up to 2 km as considered in section 3.2.3. Clearly, Figure 3.10a depicts that against the total antenna gains of 0 dBi, there is no usable bandwidth achievable. For 20 dBi, 0.235 THz of the usable bandwidth can be supported having a decrease rate of 17.65 GHz/m. Against 40 dBi, up to 18.02 GHz of the bandwidth is available at 1900 m. The decrease rate against the 40 dBi gain from 50 m to 1900 m is approximately 4.88 GHz/m. By increasing the gain up to 60 dBi, the total usable bandwidth (d = 1900 m) broadens from

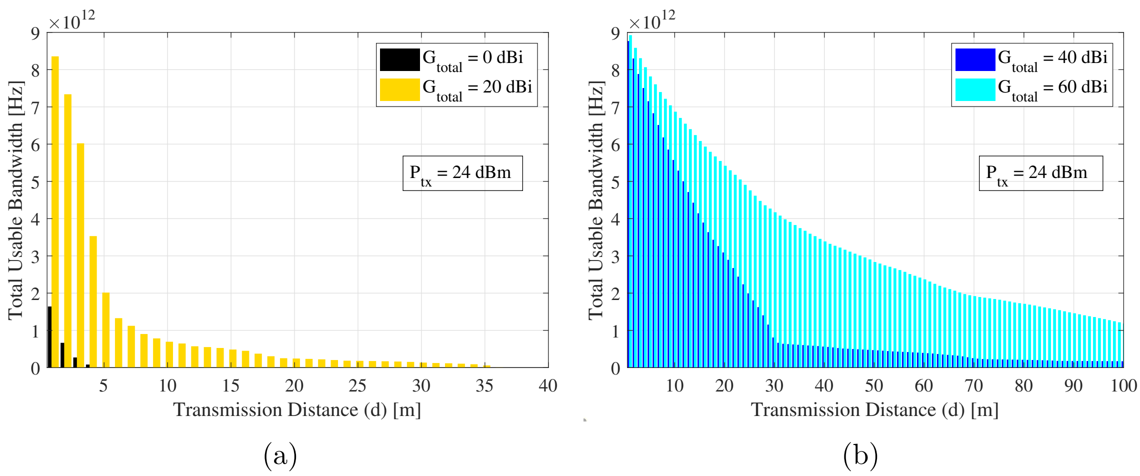

Figure 3.9 Total usable bandwidth for the Dr2Dr communication in the THz band (0.75-10 THz): (a) Total antenna gain = 0 dBi, 20 dBi, (b) Total antenna gain = 40 dBi, 60 dBi.

18.02 GHz (against 40 dBi) to 4.739 THz. Moreover, the supported transmission distance is further extended, with 4.311 THz of the usable bandwidth at 2 km. Figure 3.10b also includes a higher total antenna gain of 80 dBi, showing that even at the transmission distance of 2 km, the total usable bandwidth is about 8.218 THz, while the decreasing rate from 50 m to 2 km is about 0.5 GHz/m. Hence, promising a great potential of utilizing the THz band among the jet plane communications, offering Tbps data rates. The availability of such a large total usable bandwidth can be described by the fact that the altitude of water vapor scale across the earth's atmosphere is about 2 km, meaning that an altitude of 6 km is approximately over 95 % of the entire water vapor concentration [32].

Figure 3.11 shows the total usable bandwidth for the U2U communication case up to 2 km as considered in Section 3.2.4. The total antenna gains of 0 dBi can not offer any usable bandwidth up to 50 m as shown in Figure 3.11a. For 20 dBi gain, 9.261 THz of the bandwidth is usable at 50 m. Against 40 dBi gain and at 50 m, 9.261 THz of the total usable bandwidth is achievable supporting a maximum transmission distance of up to 850 m with 57.09 GHz of the bandwidth, with a decreasing rate of about 11.5 GHz/m. Having a higher gain of 60 dBi, 7.187 THz of the bandwidth is usable at 850 m which is about 7.13 THz greater than the 40 dBi gain, supporting the bandwidth of 2.512 THz for even up 2 km. The decreasing rate is approximately 3.455 GHz/m. If a highly directional total antenna gain of 80 dBi is provided as depicted in Figure 3.11b, interestingly, it can be seen that for the entire-considered transmission distances from 50 m up to 2 km, the total usable bandwidth maintain a near-constant of greater than 9 THz with a minute decrease rate of 55.38 MHz/m. This shows that the THz band can be highly leveraged at the

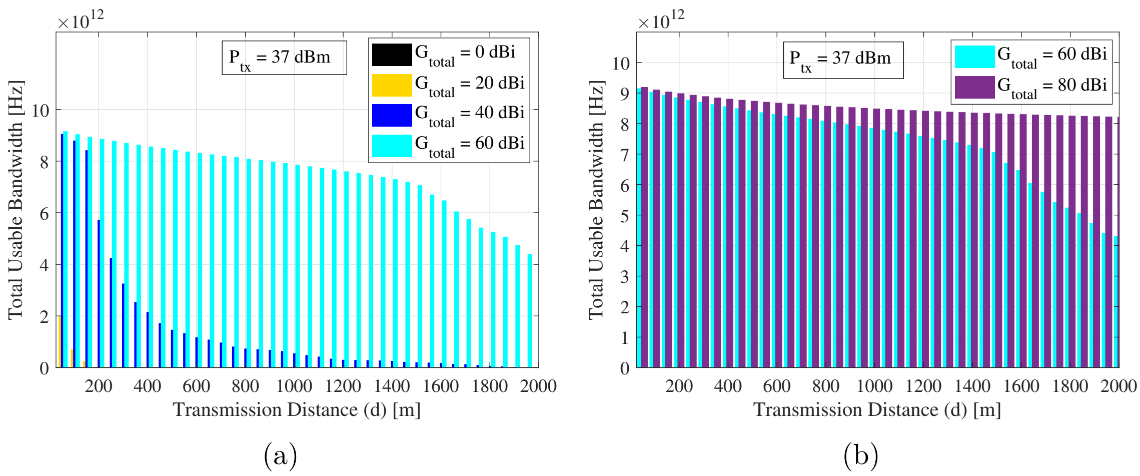

Figure 3.10 Total usable bandwidth for the J2J Communication in the THz band (0.75-10 THz): (a) Total antenna gain = 0 dBi, 20, 40, 60 dBi, (b) Total antenna gain = 60 dBi, 80 dBi.

altitudes of 16 km and above, supporting high bandwidth links among the UAVs and High-Altitude Platforms (HAPs) [69, 83].

For the Space to Space S2S communication case, the total usable bandwidths are depicted in Figure 3.12. Similar to the J2J and U2U cases, there is no usable bandwidth available against the total antenna gains of 0 dBi at 50 m, as shown in Figure 3.12a. For 20 dBi gain, 0.295 THz of the bandwidth is available at 100 m, with a decrease rate of 20.9 GHz/m. The 40 dBi gain can support a bandwidth of 24.06 GHz at 1350 m, observing a decrease rate of about 7.096 GHz/m. Increasing the gain up to 60 dBi provides 6.991 THz of the bandwidth at the distance of 1350 m, which is 6.967 THz greater as supported with the 40 dBi gain. Even at a 2 km

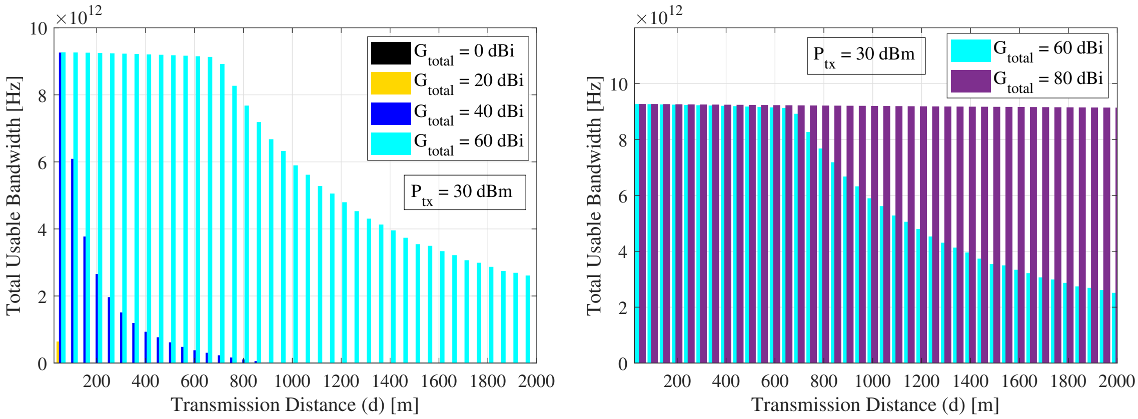

(a) (b)

Figure 3.11 Total usable bandwidth for the U2U communication in the THz band (0.75-10 THz): (a) Total antenna gain = 0 dBi, 20, 40, 60 dBi, (b) Total antenna gain = 60 dBi, 80 dBi.

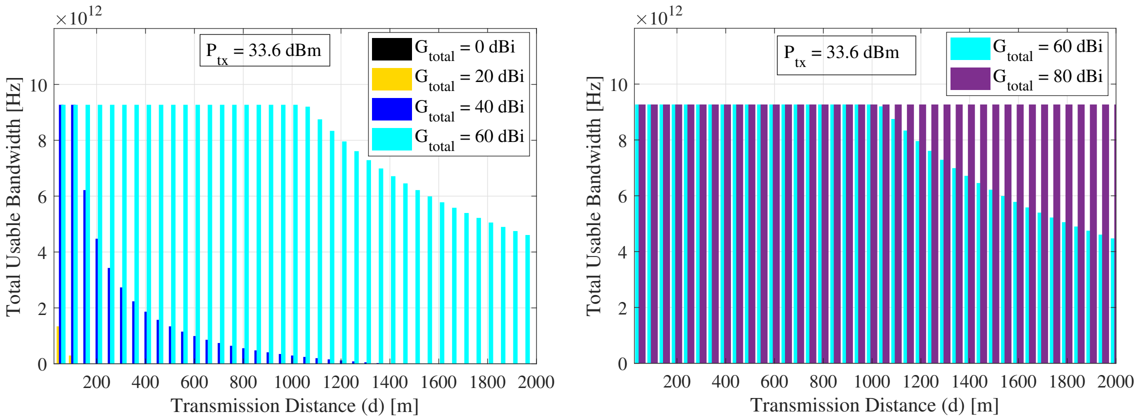

(a) (b)

Figure 3.12 Total usable bandwidth for the Space to Space S2S communication in the THz band (0.75-10 THz): (a) Total antenna gain = 0 dBi, 20, 40, 60 dBi, (b) Total antenna gain = 60 dBi, 80 dBi.

distance, 4.475 THz of the total usable bandwidth can be utilized against 60 dBi, having about 2.45 GHz/m of the decrease rate. If a very high total antenna gain of 80 dBi is provided as shown in Figure 3.12b, a constant total usable bandwidth of the entire 9.25 THz can be supported for the transmission distances from 100 m up to 2 km, i.e. corresponding to 0 GHz/m decrease rate. This shows that the THz band (0.75-10 THz) is an effective and efficient candidate for the ISLs among the traditional satellites as well as CubeSats, providing Tbps links [64]. The achievable total usable bandwidths together with the first transmission windows for each of the four aerial vehicle communication case including the sea-level benchmark are summarized in Table 3.2.

Table 3.2 Summary of the total usable bandwidth of the aerial vehicle communications cases over the THz band (0.75-10 THz).

Case [Altitude]	Total Usable Bandwidth [Hz]	Max. Tx. Distance [m / km]	Total Antenna Gains [dBi]	First Tx. Window [THz]
Sea-level [0 km]	N/A	N/A	0 dBi	[N/A]
	0.02184 THz	8 m	20 dBi	[0.7590-0.7808]
	0.01622 THz	58 m	40 dBi	[0.799-0.8152]
	0.1732 THz	100 m	60 dBi	[0.7927-0.9041]
Dr2Dr [1 km]	0.08248 THz	4 m	0 dBi	[0.8211-0.8669]
	0.05887 THz	35 m	20 dBi	[0.8190-0.8560]
	0.1728 THz	100 m	40 dBi	[0.8192-0.8559]
	1.185 THz	100 m	60 dBi	[0.7697-0.9145]
J2J [10 km]	N/A	N/A	0 dBi	N/A
	0.2535 THz	150 m	20 dBi	[0.7640-0.7711]
	0.01809 THz	1.9 km	40 dBi	[0.7637-0.7725]
	4.311 THz	2 km	60 dBi	[0.7562-0.7739]
	8.218 THz	2 km	80 dBi	[0.7548-0.9868]
U2U [16 km]	N/A	N/A	0 dBi	N/A
	0.6302 THz	50 m	20 dBi	[0.75-0.7505]
	0.05709 THz	850 m	40 dBi	[0.75-0.7515]
	2.512 THz	2 km	60 dBi	[0.75-0.7519]
	9.142 THz	2 km	80 dBi	[0.75-0.7525]
Space to Space S2S [99 km]	N/A	N/A	0 dBi	N/A
	0.295 THz	100 m	20 dBi	[0.75-0.8005]
	0.02406 THz	1.35 km	40 dBi	[0.75-0.7740]
	4.475 THz	2 km	60 dBi	[0.75-1.805]
	9.25 THz	2 km	80 dBi	[0.75-10]

In this chapter, we have provided the extensive path loss analysis over the THz band (0.75-10 THz) for various atmospheric altitudes and we have obtained the total usable bandwidth over the THz band (0.75-10 THz) at those altitudes, for the first time in the literature. With this study, we have highlighted the effectiveness of the THz band at higher altitudes, where the absorption loss values are minimal, providing high bandwidth and data rate links among flying aerial vehicles, including drones, jet planes, UAVs and up to the orbiting satellites. Hence, this study can serve as a reference for researchers studying the THz band communications among aerial vehicles for realizing/manufacturing practical THz band transceivers.

It has been observed that between the altitudes of 1 km and 10 km, the zenith angle influences the THz band transmittance considerably, particularly for greater transmission distances. This effect has been highly observed across the 10 km altitude (J2J case) among the other atmospheric altitude cases. As the altitude is further increased, the zenith angle influence on the transmittance becomes less significant due to the negligible absorption losses at the higher altitudes, and as such, the total path loss starts exhibiting to be merely the free space spread loss, as observed in the U2U (altitude = 16 km) and Space to Space S2S (altitude = 99 km) communication cases. It has also been noticed that for all of the four atmospheric altitude cases, the vertically-up communication ($\theta_{ZA} = 0^0$) offers the lowest total mean path losses in comparison to the other directions. Furthermore, the transmittance, absorption loss and path loss values have been provided in the thesis as a guideline for the researchers studying aerial vehicle communications in the THz band (0.75-10 THz). Finally, it has been deduced that increasing the altitude of the THz band communication also increases the total usable bandwidth, due to the lower absorption losses at the higher altitudes.

Numerical results show that for the altitudes of 16 km and above, the entire THz band (0.75-10 THz) is usable as a single transmission window, as the absorption loss values are negligible at such high altitudes. The altitude of 10 km still offers a total usable bandwidth of 8.218 THz up to the transmission distance of 2 km provided that a very high total antenna gain of 80 dBi is supported. For the sea-level case up to 1 km altitude (Dr2Dr case), the initial THz band window (0.75-1 THz) is feasible for communication.

Having analyzed the total usable bandwidths of various aerial communication cases by considering the constant noise model and practical physical parameters, exploitation of this usable THz bandwidth across the THz band (0.75-10 THz) for capacity computations using colored noise model under realistic beam misalignment fading and multi path fading is covered in the following Chapter 4 of this dissertation.

Chapter 4

VARIABLE-BANDWIDTH MODEL AND CAPACITY ANALYSIS FOR TERAHERTZ AERIAL COMMUNICATIONS

In this chapter, first, the THz propagation modeling in the atmosphere using LBLRTM is presented. Then, altitude-dependent channel model with fading is provided. Additionally, the colored noise model is considered for SNR and capacity computations. For each aerial scenario under fading, Beam Misalignment (BM) fading is considered while for near ground THz communications, i.e., drones, Multi path (MP) fading is also considered into the channel model. Finally, the variable-bandwidth approach is presented, which is also compared with the standard narrow-band approach in terms of capacity for various practical aerial scenarios at different altitudes, directions of communications, and ranges.

4.1 System Model

4.1.1 Communication Scenarios

As shown in Fig. 4.1 and Fig. 4.2, we consider aerial communications, where an aerial vehicle (transmitter) is at an altitude, z_1, transmitting to another aerial vehicle (receiver) at z_2 over a transmission distance, d. The receiver can be at an arbitrary zenith angle, θ_{ZA} from the transmitter, which varies from $0°$ to $180°$, indicating vertically-up and vertically-down directions, respectively, as depicted in Fig. 4.2. Directive antennas are considered both at the transmitter and receiver with narrow

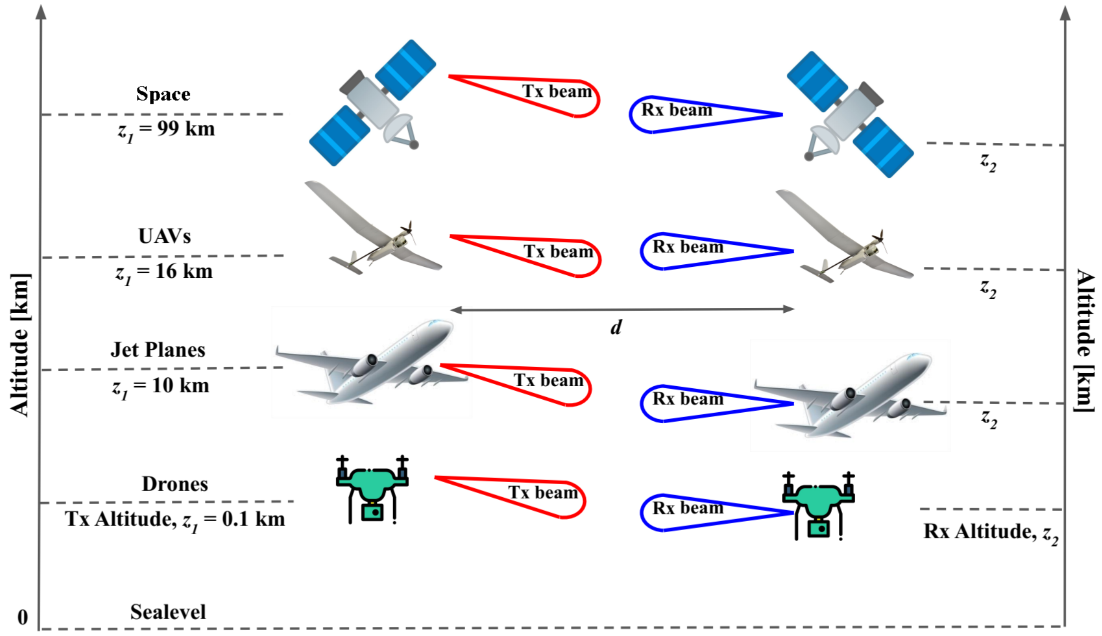

Figure 4.1 Communication among various practical aerial vehicles at different atmospheric altitudes, z_1, z_2.

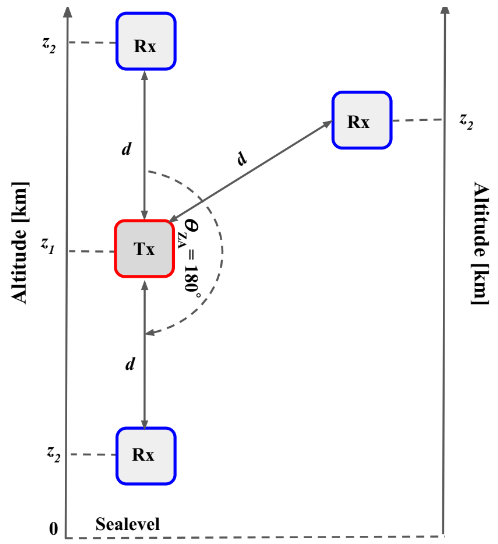

Figure 4.2 Illustration of zenith angle, θ_{ZA} between transmitting and receiving aerial vehicles and how it effects z_2 for given z_1 and d values.

(Tx-Rx) beams pointing towards each other. Within this general model, we consider four practical aerial communication scenarios at the following realistic, practical altitudes: Drone-to-Drone (Dr2Dr) communication at z_1 = 100 m [84], commercial Jet Plane-to-Jet Plane (J2J) communication at z_1 = 10 km [33], high altitude UAV-to-UAV (U2U) at z_1 = 16 km [69], and Space-to-Space communication (S2S) at z_1 = 99 km [64].

Next, we present the THz band channel and colored noise models, both incorporating the effect of altitude in atmospheric propagation. Fading effects are considered in the channel model, considering 1) fading due to Tx-Rx BM, which can occur in all of the scenarios, and 2) MP fading due to reflections, for the Dr2Dr scenario due to obstacles, such as buildings, foilage, etc. which exist only at that altitude.

4.1.2 Channel Model With Fading

To characterize the THz channel between the transmitter and receiver in Fig. 4.1 and Fig. 4.2, we incorporate the path gain (free space spread and absorption), BM fading and MP fading, in the total channel coefficient, h, as:

$$h = h_l h_p h_f, \tag{4.1}$$

where h_l, h_p and h_f are the path gain coefficient, BM fading coefficient, and the MP fading coefficient, respectively.

Path Gain

The path gain in aerial THz communications depends not only on frequency and distance, but also on the altitude through variations of temperature and water vapor concentration (see Fig. 2.3), both of which affect THz propagation. The deterministic path gain coefficient, $h_l(f, z_1, z_2, d)$ is calculated as:

$$h_l(f, z_1, z_2, d) = h_s(f, d) h_a(f, z_1, z_2, d) \ , \tag{4.2}$$

where f is the frequency of the EM wave in hertz, z_1 and z_2 are the atmospheric altitudes in meters of the transmitter and the receiver, respectively, and d refers to the transmission distance in meters.

$h_s(f, d)$ refers to the free space spread gain coefficient caused by the attenuation experienced by the THz wave atmospheric propagation with the isotropic antenna, which is calculated as [21]:

$$h_s(f, d) = \frac{c}{4\pi f d} \ , \tag{4.3}$$

where $c = 299792458 \ m/s$ is the speed of the EM wave in free space.

The absorption gain, $h_a(f, z_1, z_2, d)$ on the THz band electromagnetic (EM) wave, which is mainly caused by the water vapor molecules in the atmosphere, can be obtained as [17, 18, 33]:

$$h_a(f, z_1, z_2, d) = \left(\tau(f, T(z_1, z_2), v(z_1, z_2), d)\right)^{1/2} , \tag{4.4}$$

where $T(z_1, z_2)$ is the atmospheric temperature in Kelvin, and $v(z_1, z_2)$ is the water vapor concentration across altitudes z_1, z_2. $\tau(f, T(z_1, z_2), v(z_1, z_2), d)$ is the medium's transmittance defined as the ratio of the radiated to the incident EM powers, as per the Beer-Lambert's Law [54]. In this thesis, we employ the radiative transfer theory [52] by obtaining the transmittance from LBLRTM for computing the attenuation and noise of the EM wave, which is mainly caused by the water vapor molecules present in the atmosphere. For the non-horizontal cases, i.e., z_1 is not equal to z_2, LBLRTM averages $T(z_1, z_2)$ and $v(z_1, z_2)$ over the various atmospheric layers that exist across z_1 and z_2, thereby providing average transmittance values, i.e. $\overline{\tau}(f, T(z_1, z_2), v(z_1, z_2), d)$. Moreover, since the atmospheric concentration changes gradually (see Fig. 2.3), the bending phenomenon of the propagating THz waves can be neglected.

Beam Misalignment

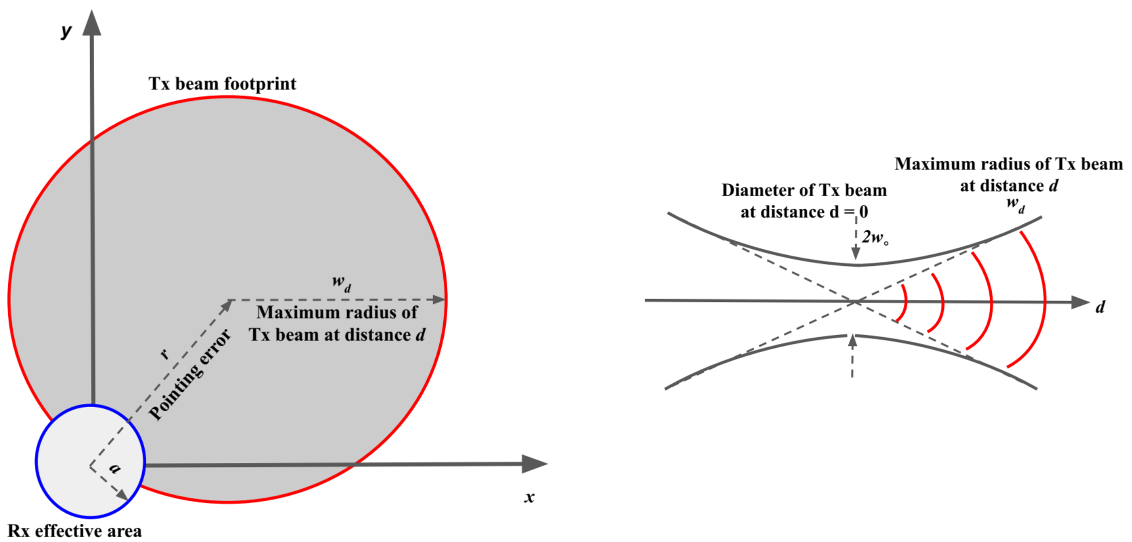

(a) (b)

Figure 4.3 THz beam propagation: (a) Effective area of the Tx-Rx beam footprints at a transmission distance, d with Tx-Rx BM, and (b) Tx beam spread.

As depicted in Fig. 4.3, it is assumed that the receiver antenna (Rx) has a circular beam detector with radius a, spanning over an effective area, A. Similarly, we also assume a circular beam for transmitter antenna (Tx) with a radius ρ at a distance, d, where w_d is the beam's radius at d. Moreover, both the Tx and Rx beams are taken to be on the positive x-y plane, while r is the BM error defined as the radial distance among the Tx and Rx beams. Because of the symmetry of both the Tx and Rx beams, h_p is only dependent on $r = |r|$. Hence, we further assume that r is located over the x-axis. Consequently, the BM fading coefficient, h_p representing the fractional power collected across Rx with area, A at d can be expressed as [85]:

$$h_p(r, d) = A_0 \; exp\left(-\frac{2r^2}{w_{eq}^2}\right) \; . \tag{4.5}$$

Here, w_{eq} is the equivalent beam-width of Tx, A_0 is fractional power collected by Rx at $r = 0$, which can be expressed as $A_0 = [erf(u)]^2$, where $u = \frac{\sqrt{\pi}a}{\sqrt{2}w_d}$. Here, a is the radius of the Rx's effective area, w_d is the Tx beam footprint at distance, d. Furthermore, w_{eq}^2 and w_d^2 are interrelated via $w_{eq}^2 = w_d^2 \frac{erf(u)}{2u \; exp(-u^2)}$.

By considering independent and identically distributed Gaussian distributions for the horizontal and the vertical displacement, one can obtain the probability density function (pdf) of the radial displacement, r at Rx as the Rayleigh distribution as follows:

$$f_r(r) = \frac{r}{\sigma_s^2} exp\left(\frac{r^2}{2\sigma_s^2}\right) \; . \tag{4.6}$$

Here, σ_s is BM error displacement (jitter) along Rx. By combining (4.5) and (4.6), the pdf of h_p can be expressed as

$$f_{h_p}(x) = \frac{\zeta^2}{{A_0}^{\zeta^2}} x^{\zeta^2 - 1} \; , \tag{4.7}$$

where $\zeta = \frac{w_{eq}}{2\sigma_s}$. It is worth-mentioning here, that this BM fading model has been employed extensively in various works on free space optical systems [85], as well as in a recent work on THz wireless systems [21].

Multipath Fading

For accommodating the MP fading effect, we model h_f generically as α - μ distribution, having pdf as follows [86]:

$$f_{h_f}(x) = \frac{\alpha\mu^{\mu}}{\hat{h}_f^{\alpha\mu}\Gamma(\mu)} x^{\alpha\mu-1} exp\left(-\mu\frac{x^{\alpha}}{\hat{h}_f^{\alpha}}\right) , \tag{4.8}$$

here, $\alpha > 0$ is a fading parameter, whereas μ and $\hat{h_f}$ denote the fading channel envelope's normalized variance and α-root mean value, respectively. It is to be noted here that the α - μ distribution is a generalized form of many well-known fading distributions e.g., Rayleigh ($\alpha = 2$, $\mu = 1$), Nakagami-m ($\alpha = 2$, and μ is the fading parameter) etc [86].

4.1.3 Colored Noise

The molecules present in the atmosphere not only induce attenuation, but they also introduce noise [87]. This fact is considered as a noise factor affecting the EM wave propagation across the THz band, and the parameter for measuring this is known as the channel's emissivity, ϵ [18], mathematically expressed as

$$\epsilon(f, z_1, z_2, d) = 1 - \tau(f, T(z_1, z_2), v(z_1, z_2), d) . \tag{4.9}$$

The molecular absorption-based equivalent noise temperature T_{noise} (Kelvin), being the chief source of noise across the THz band is calculated as

$$T_{noise}(f, z_1, z_2, d) = T_0\epsilon(f, z_1, z_2, d) , \tag{4.10}$$

where T_0 denotes the reference temperature in Kelvin. It is to be noted here that $T_{noise}(f, z_1, z_2, d)$ is mainly present across those THz band frequencies, where the atmospheric absorption (mainly due to the water vapor molecules) is significantly large.

For computing the equivalent noise power at the Rx side, the transmission bandwidth needs to be specified, which depends on the atmospheric medium's composition as well as d. Therefore, for a bandwidth, Δf, the equivalent noise power,

$P_n(f, z_1, z_2, d, \Delta f)$ (in Watts) can be computed as

$$\begin{aligned} P_n(f, z_1, z_2, d, \Delta f) &= \int_{\Delta f} N(f, z_1, z_2, d) df \\ &= k_B \int_{\Delta f} T_{noise}(f, z_1, z_2, d) df, \end{aligned} \tag{4.11}$$

where N is the noise PSD in Watts/Hz, k_{B} refers to the Boltzmann constant, (1.38E$-$23 m^{2}kgs^{-2}K^{-1}). Please refer to Appendix A for an in-depth analysis of the deterministic path gain and noise across various atmospheric altitudes, transmission ranges, and zenith angles. Towards this end, we have provided the THz band specific channel model for the total channel coefficient and the noise formulations, which will be required for the SNR computations in the subsequent section.

4.2 Altitude-Dependent Variable Bandwidth Model

As already discussed in Section 4.1 and shown in Appendix A, Fig. A.1 and Fig. A.2 in particular, not only the absorption gain across the THz band, but also the noise is colored. For a simplified communication model, both the deterministic path gain and the noise should be flat over a given transmission band, as the flatness over the path gain implies flat fading, while the whiteness of the noise implies uncorrelated noise samples, both of which simplify channel estimation and receiver design [88]. This leads up to our goal of finding those bands across the THz band (0.75-10 THz), where both the path gain and the noise satisfy flatness within an acceptable level. Naturally, the commonly flat bands vary with the atmospheric altitudes, which results in our proposed altitude-dependent variable bandwidth model.

As an example of illustrating common flat bands among the total path gain and the noise, we consider the settings, $z_1 = z_2 = 100$ m, $d = 100$ m, $\theta_{ZA} = 90°$ (horizontal) using US Standard 1976 weather profile in LBLRTM. Fig. 4.4 shows the path gain (left y-axis) and the noise PSD (right y-axis) with the first two common flat bands (highlighted as red). The first common flat band is found as $(\Delta f)_i = 0.1127$ THz i.e. , [0.7902-0.9029 THz] centered at $f_i = 0.8465$ THz, while the second one is $(\Delta f)_{(i+1)} = 0.0228$ THz i.e. , [0.9278-0.9506 THz] centered at $f_{(i+1)} = 0.9392$ THz.

We determine the commonly flat bands over the entire THz band (0.75-10 THz), in an adaptive fashion with respect to the atmospheric altitude and the transmission distance. We propose a method for computing common flat bands $(\Delta f)_i$ centered

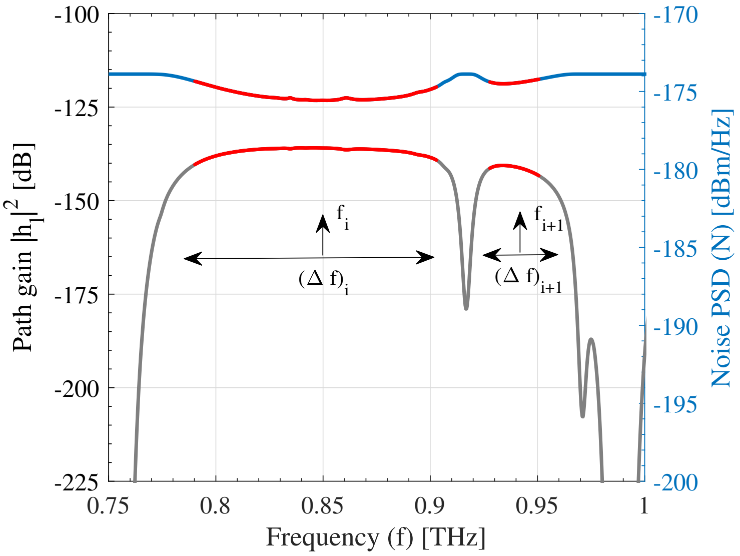

Figure 4.4 Visual illustration of the common flat bands among the path gain and the noise: $z_1 = z_2 = 100$ m, i.e., $\theta_{ZA} = 90°$ (horizontal), $d = 100$ m, reference temperature, $T_0 = 296$ K.

Algorithm 1: Finding common flat bands among path gain and noise

1 **Initialization:** Choose $(\Delta f)_{min}$, η, and set $i = 1$
2 *Step 1:* Define search set X containing all path gain narrowbands
3 **while** $i > 1$ *and* $(\Delta f)_i$ *is not empty* **do**
4   *Step 2:* Find first f_{min}, f_{max} from X under $(\Delta f)_{min}$ and η conditions
5   *Step 3:* $(\Delta f)_i^X = f_{max} - f_{min}$
6   *Step 4:* Delete *range*(f_{min}, f_{max}) from X
7     $i \leftarrow i + 1$
8 **end**
9 **end while**
10 Repeat Line 2 to Line 8 for Y containing all noise narrowbands, obtaining $(\Delta f)_i^Y$
11 $(\Delta f)_i = (\Delta f)_i^X \cap (\Delta f)_i^Y$
12 $f_i = f_{min}$ (of Line 10) + $\frac{(\Delta f)_i}{2}$

at f_i, where $i = 1, 2, 3 \ldots I$ among $|h_l|^2$ and N. The LBLRTM's spectral resolution, $\Delta f = 0.3$ GHz, which is an extremely fine narrowband. Therefore, in order to maintain a flatness characteristic and to particularly avoid the peak transitions being considered into a flat band, we consider a minimum bandwidth of 3 GHz, expressed as $(\Delta f)_{min}$. For defining the cut-off frequencies, i.e., f_{min} and f_{max} of a flat band, a threshold needs to be defined. In [4], a threshold of 10 dB/km on the absorption loss is considered to define a transmission window based on the total path loss analysis. In this thesis, we define the distance-altitude adaptive threshold, η, taken to be 10 dB/km across $|h_l|^2$ and N, for each. Subsequently, we define a search set, X storing all $|h_l|^2$ narrowbands, for obtaining the flat bands over $|h_l|^2$, as $(\Delta f)_i^X$ satisfying both $(\Delta f)_{min}$ and η. This procedure is repeated for N using a search set, Y for obtaining $(\Delta f)_i^Y$. Finally, the common flat bands across $|h_l|^2$ and N are obtained as $(\Delta f)_i$ centered at f_i. It is to be noted here that η and $(\Delta f)_{min}$ are the design parameters, and the SNR and capacity results presented in this thesis also depend on these parameters.

Having computed the common flat bands among the path gain and the noise, the SNR, γ across the i^{th} common flat band, where $i(z_1, z_2, d) = 1, 2, 3...I$ across the THz band (0.75-10 THz) can be expressed as

$$\gamma(f_i, z_1, z_2, d, (\Delta f)_i)) = \frac{P_T^i \; |h(f_i, z_1, z_2, d)|^2 \; G_T}{P_n(f_i, z_1, z_2, d, (\Delta f)_i)} \; , \tag{4.12}$$

where P_T^i refers to the transmit power across the i^{th} common flat band (i.e. , $(\Delta f)_i$), while P_T here is the total transmit power in Watts. Naturally, the γ computation would change with respect to a chosen power assignment, which are explained in the subsequent section in detail. $|h|^2$ is the total channel gain derived from (4.1), G_T refers to the total antenna gains, and P_n is the noise power in Watts across $(\Delta f)_i$ from (4.11). It is to be mentioned here that in this work, γ values are considered to be at the front of the receiver. In regards to the practical THz receiver design, Noise Figure (NF) should also be introduced in (4.12). For instance, typical NF values considered in the literature for THz band receivers vary from 0 dB (ideal receiver) to 9.56 dB [77]. Hence, for practical THz receivers, adding (in dB) the NF contribution with P_n into (4.12) would result in a substantial decrease in γ values across the THz band (0.75-10 THz). Therefore, P_T and G_T values should be adjusted/increased accordingly to achieve acceptable γ levels.

4.3 Capacity Analysis

In this section, we assess capacity, hence the potential of communication over the THz band (0.75-10 THz) among the aerial vehicles by considering the realistic THz band channel model as discussed in Section 4.1. The LBLRTM tool is used to obtain the transmittance values, $\tau(f, T(z_1, z_2), v(z_1, z_2), d)$ to obtain absorption gain and emissivity, as required in (4.4) and in (4.9), respectively, for the four practical aerial vehicle communication scenarios at various altitudes, zenith angles and transmission distances.

Firstly assuming no fading, i.e., $h = h_l$, we introduce an alternative capacity computation which makes use of the common flat bands, $(\Delta f)_i$ among the path gain, $|h_l|^2$ and the noise PSD, N obtained by Algorithm 1. More precisely, the i^{th} common flat band having a variable bandwidth, $(\Delta f)_i$ is tuned around the frequency f_i, where $i(z_1, z_2, d) = 1, 2, 3, ..., I$. In this way, the channel considered for transmission comprises of only those bands, which are flat in common, i.e. , across both $|h_l|^2$ and N. Hence, the sum capacity, C_{V-BW}, of the altitude-dependent variable bandwidth model at a transmission distance, d and between Tx and Rx altitudes, z_1 and z_2, respectively, is calculated as:

$$\begin{aligned} C_{V-BW}(z_1, z_2, d) &= \sum_{i=1}^{I} (\Delta f)_i \ log_2 \left[1 + \gamma(f_i, z_1, z_2, d, (\Delta f)_i)\right] \\ &= \sum_{i=1}^{I} (\Delta f)_i \ log_2 \left[1 + \frac{P_T^i \ |h(f_i, z_1, z_2, d)|^2 \ G_T}{P_n(f_i, z_1, z_2, d, (\Delta f)_i)}\right] \ . \end{aligned} \tag{4.13}$$

We consider two different power allocation schemes for dividing the total power within frequency bands: In the EP allocation scheme, power of each common flat band is found as $P_T^i = \frac{P_T}{\sum_{i=1}^{I} (\Delta f)_i} (\Delta f)_i$. In the second scheme, WF power allocation is performed in two stages for our variable bandwidth approach. At the first stage, WF is performed among all common flat bands, $i(z_1, z_2, d) = 1, 2, 3, ..., I$, with respect to the average SNR, $\overline{\gamma_i}$ of each i (i.e., the average SNR of all $\Delta f = 0.3$ GHz present in i), as follows [88]:

$$\frac{P_T^i}{P_T} = \begin{cases} \frac{1}{\gamma_\circ} - \frac{1}{\overline{\gamma_i}} & , \overline{\gamma_i} \geq \gamma_\circ \quad \text{s.t. } \sum_{i=1}^{I} P_T^i \leq P_T \\ 0 & , \overline{\gamma_i} < \gamma_\circ \ , \end{cases} \tag{4.14}$$

where P_T^i is the optimal power assigned to the common flat band, $\gamma_\circ$ denotes the SNR threshold, and is obtained by satisfying $\sum_{i=1}^{I} \left(\frac{1}{\gamma_\circ} - \frac{1}{\overline{\gamma_i}}\right) = 1$. Subsequently as the second stage, we again perform WF by optimally distributing P_T^i within each common flat band, i, comprising of $\Delta f = 0.3$ GHz, which is the spectral resolution of LBLRTM [18, 19, 50, 51].

According to the standard approach, the altitude dependent capacity, C_{STD} is computed as:

$$C_{STD}(z_1, z_2, d) = \sum_{k=1}^{K} \Delta f \ log_2 \left[1 + \frac{P_T^k \ |h(f_k, z_1, z_2, d)|^2 \ G_T}{P_n(f_k, z_1, z_2, d, (\Delta f))}\right] \ , \tag{4.15}$$

where f_k is a function of f_i with k = 1, 2, 3,...,K. Here, with the EP allocation,

P_T is equally distributed over the entire THz band (0.75-10 THz), i.e., it is divided among all constant narrowbands with $\Delta f = 0.3$ GHz. The WF power allocation is performed in a single stage by optimally distributing P_T over (0.75-10 THz) across all constant narrowbands, $k = 1, 2, 3, ..., K$, each 0.3 GHz wide, by following the similar approach as in (4.14), with P_T^k as the optimal power assigned to the constant narrowband, k, $\gamma_\circ$ denotes the SNR threshold, γ_k is the SNR of k by considering that it is allocated the entire power budget. Here, $\gamma_\circ$ is computed by satisfying $\sum_{k=1}^{K}\left(\frac{1}{\gamma_\circ} - \frac{1}{\gamma_k}\right) = 1$ [88].

For capacity under fading, we consider the ergodic capacity, by incorporating the BM and the MP fading models in the channel coefficient, as $h = h_l h_p h_f$, as provided in Section 4.1.2. The ergodic capacity of the variable bandwidth approach, $C^E_{V-BW}(z_1, z_2, d)$ is obtained by modifying (4.13) as

$$C^E_{V-BW}(z_1, z_2, d) = \mathbb{E}\left(\sum_{i=1}^{I}(\Delta f)_i \ log_2\left[1 + \frac{P_T^i \ |h(f_i,z_1,z_2,d)|^2 \ G_T}{P_n(f_i,z_1,z_2,d,(\Delta f)_i)}\right]\right) \ , \tag{4.16}$$

where $\mathbb{E}(.)$ denotes the expectation over random realizations of the channel h subject to fading.

Likewise, the ergodic capacity of the standard approach, $C^E_{STD}(z_1, z_2, d)$ is computed by modifying (4.15) as

$$C^E_{STD}(z_1, z_2, d) = \Delta f \ \mathbb{E}\left(\sum_{k=1}^{K} \ log_2\left[1 + \frac{P_T^k \ |h(f_k,z_1,z_2,d)|^2 \ G_T}{P_n(f_k,z_1,z_2,d,(\Delta f))}\right]\right) \ . \tag{4.17}$$

In the following subsections, we first investigate the effect of altitude(s) on the capacity in general, assuming no fading. Then, we consider the specific four aerial communication scenarios under no fading and fading conditions. In all cases, the proposed variable bandwidth capacity computation is compared to the standard capacity computation, considering EP and WF power allocation schemes. At the end, a summary table is provided for benchmarking horizontal communications at different altitudes, corresponding to each scenario, also including the sea-level case for comparison.

4.3.1 Effect of Altitude on Capacity

The variation of atmospheric conditions with altitude shown in Fig. 2.3 can be leveraged for communications over the THz band (0.75-10 THz) due to the receded

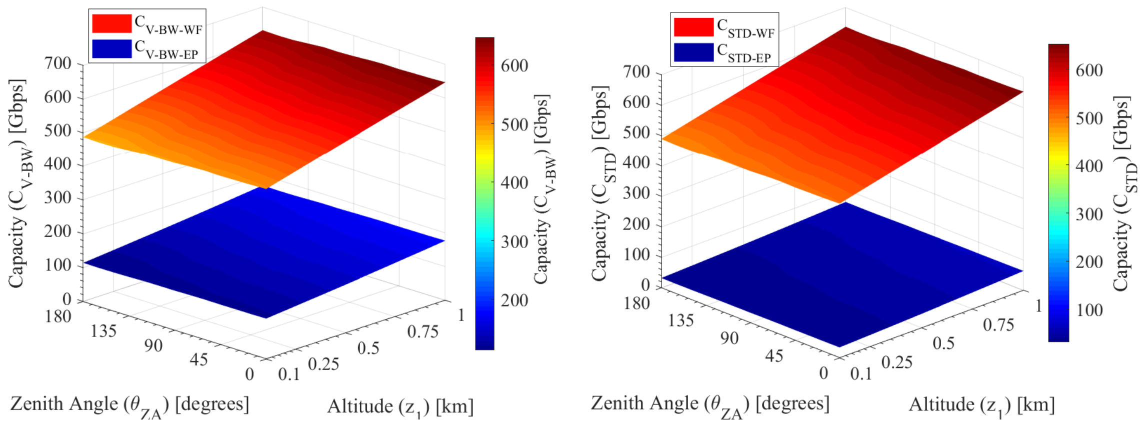

(a) Variable bandwidth approach. (b) Standard approach.

Figure 4.5 Channel capacity (no fading) as the function of Tx altitude, z_1 and zenith angle, θ_{ZA} at $d = 0.1$ km. For a given z_1 and θ_{ZA} pair, z_2 is found according to the transmission distance d.

absorption effect as compared to that at the sea-level. In order to quantify this potential, we consider the two channel capacity computations, C_{V-BW} and C_{STD} approaches given in equations (13) and (15), respectively, as joint functions of z_1 and θ_{ZA} from 0° to 180° and d. For a given z_1 and θ_{ZA} pair, z_2 is found according to the transmission distance d, and US Standard 1976 model is selected as the weather profile in LBLRTM. EP and WF power allocations are considered for each approach, as explained in the previous section.

For assessing the joint impact of z_1 and θ_{ZA} on the capacity for the lower altitude, Dr2Dr communications, Fig. 4.5(a) illustrates the C_{V-BW} as the function of z_1 from 0 to 1 km, and θ_{ZA} over 0°-180°, at $d = 0.1$ km. P_T is set as 24 dBm [79] and G_T is taken as 60 dBi [89]. As depicted in this figure, employing the WF scheme promises the highest capacity. For instance, at $z_1 = 0.1$ km and $\theta_{ZA} = 0°$, $C_{V-BW-WF}$ offers 503.4 Gbps while with EP, it stands at 119.8 Gbps. Moreover, particularly for $\theta_{ZA} = 0°$, capacity values of both the power allocation schemes increment with increasing z_1 from 0.1 km to 1 km, as the atmospheric concentration starts decreasing with the altitude. For comparing C_{V-BW} approach, Fig. 4.5(b) shows the capacity with the standard computation benchmark approach, i.e., C_{STD} over the identical settings as chosen in Fig. 4.5(a). Evidently, both the C_{V-BW} and C_{STD} approaches with WF offer similar capacity values, whereas the C_{V-BW} with EP allocation visibly outperforms its standard approach counterpart over the entire considered Tx altitude and zenith angle ranges. For instance, at $z_1 = 0.1$ km and $\theta_{ZA} = 0°$, C_{STD} with EP offers 34.52 Gbps, which is 28.8 % of the capacity as offered by its variable bandwidth counterpart. This infers that when only the EP allocation is provisioned, the proposed variable bandwidth approach promises to be a viable approach to achieve higher capacity among Dr2Dr communications.

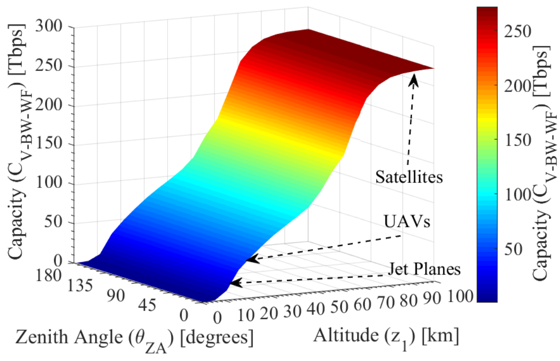

(a) Variable bandwidth approach with water-filling.

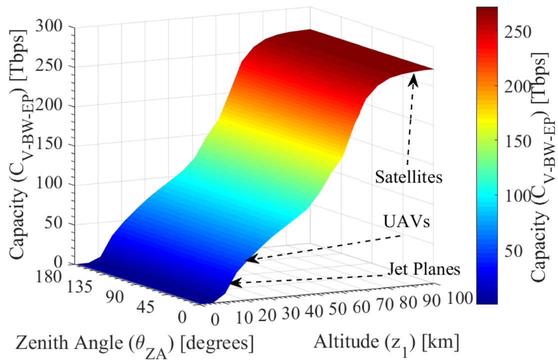

(b) Variable bandwidth approach with equal power.

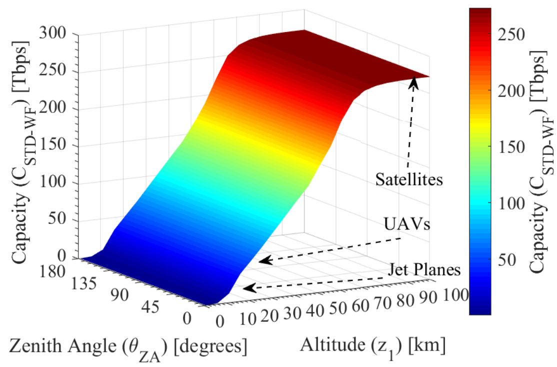

(c) Standard approach with water-filling.

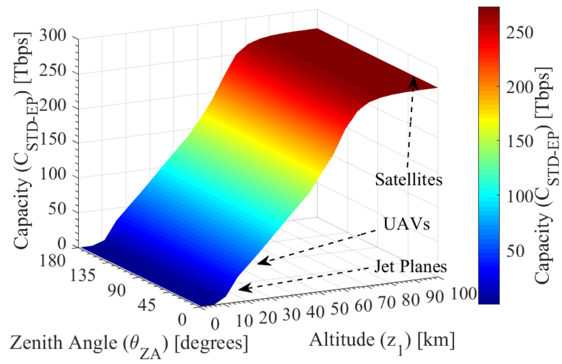

(d) Standard approach with equal power.

Figure 4.6 Channel capacity (no fading) as the function of Tx altitude, z_1 and zenith angle, θ_{ZA} at $d = 1$ km. For a given z_1 and θ_{ZA} pair, z_2 is found according to the transmission distance d.

Fig. 4.6 shows the variation of capacity with z_1 and θ_{ZA} for higher altitudes, where z_1 is varying from 1 to 100 km, transmission distance is set as, $d = 1$ km, P_T set as 30 dBm [81], and G_T is taken as 80 dBi [90]. Fig. 4.6(a) and Fig. 4.6(b) show capacity graphs of C_{V-BW} approach with WF and EP allocations, respectively. Clearly, there is no considerable capacity available over the entire considered zenith angle ranging from 0° (vertically-up) to 180° (vertically-down) at $z_1 = 0$ km (sea-level). $z_1 = 10$ km depicts a visible capacity increase, which is 10.7 Tbps with the EP scheme. This exponential increasing trend continues up to the $z_1 = 30$ km, after which a decline in the capacity increase can be observed up to the 50 km altitude. The main reason behind this fact is due to the increase in the atmospheric temperature across the 30 km to 50 km altitudes, as shown earlier in Fig. 2.3(a) and Fig. A.1 (Appendix A). This temperature increase causes the transmittance to be more colored, which in turn increases the noise color, resulting in fewer flat bands across the noise. Hence, the total number of the common flat bands among the path gain and the noise are decreased. Beyond $z_1 = 60$ km, the temperature declines again making the noise less colored, subsequently widening the common flat band, thereby increasing the capacity. Starting $z_1 = 90$ km, capacity values of greater than 300 Tbps are achievable. Fig. 4.6(c) and Fig. 4.6(d) illustrate the capacity 3D graphs of C_{STD} computation with WF and EP schemes, respectively. Unlike the C_{V-BW}, C_{STD} is not substantially influenced by the temperature changes with respect to the altitudes, as the standard capacity computation follows the constant narrowband approach. However, as z_1 is further increased up to 90 km, the gap between the two approaches reduces to even less than a Tbps. Having analyzed the joint influence of the altitude and zenith angle over the channel capacity under no fading, next, we investigate the capacity in four aerial communication scenarios (at the mentioned altitudes in Fig. 4.6), also considering fading.

4.3.2 Aerial Communication Scenarios

In this part, we assess the channel capacity performance of the four aerial scenarios without fading by using (4.13) and (4.15), and with fading by considering (4.16) and (4.17).

Drones

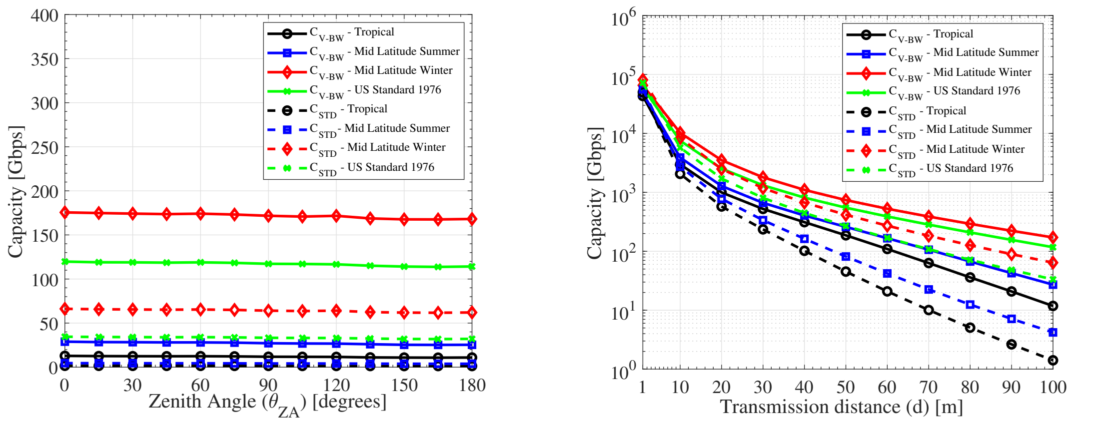

(a) Capacity vs. zenith angle: $z_1 = 100$ m, $d = 100$ m.

(b) Capacity vs. distance: $z_1 = z_2 = 100$ m, $\theta_{ZA} = 90°$.

Figure 4.7 Dr2Dr communication (no fading): Capacity analysis considering variable bandwidth and standard approaches with EP allocation. Four weather profiles are considered in LBLRTM.

As the first aerial vehicle communication scenario, we consider realistic Drone-to-Drone (Dr2Dr) communication, where the Tx drone is at $z_1 = 100$ m, $d = 100$ m

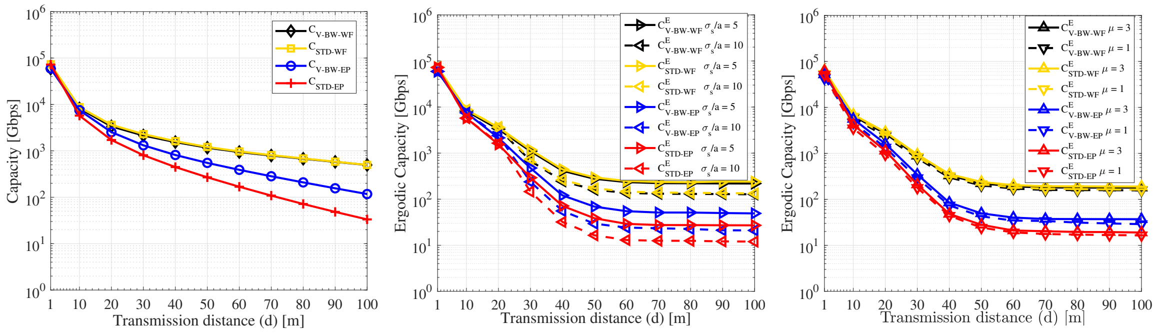

(a) Capacity under no fading.

(b) Ergodic capacity under BM fading only.

(c) Ergodic capacity under both BM fading and MP fading.

Figure 4.8 Dr2Dr communication (without and with fading): Capacity vs. distance considering variable bandwidth and standard approaches with WF and EP allocations. US Standard 1976 weather profile is set in LBLRTM with $z_1 = z_2 = 0.1$ km, $\theta_{ZA} = 90°$.

between Tx-Rx drones, and the altitude of the Rx drone, z_2 is determined by variable zenith angle, θ_{ZA}. P_T is set as 24 dBm [79] and G_T as 60 dBi [89]. Fig. 4.7 shows channel capacity under no fading, considering the water vapor effect via four weather profiles in LBLRTM for both the variable bandwidth and standard computations with EP allocation. Fig. 4.7 (a) depicts that over the entire θ_{ZA} range from 0° (vertically-up) to 180° (vertically-down, which corresponds to the drone to sea-level case), no considerable variation in the capacity is seen, as the atmosphere is dense and homogeneous around the lower (near-ground) altitudes, as shown earlier in Fig. 2.3(a). The proposed variable bandwidth approach offers higher capacity values than the standard benchmark, as at such lower atmospheric altitudes, water vapor based absorption is huge, hence, transmitting equally over the entire THz band (0.75-10 THz), irrespective of the flat bands or the peaks, is not a viable option. Instead, transmitting over the common flat bands promises a substantially higher capacity. The highest capacity is offered by the C_{V-BW} approach using Mid Latitude Winter weather profile with 175.6 Gbps, while the standard approach stands at 66.16 Gbps, both at $\theta_{ZA} = 0°$. Fig. 4.7(b) illustrates the Dr2Dr capacity trend as the function of the d from 1 m up to 100 m with $\theta_{ZA} = 90°$ (horizontal). At $d = 1$ m, both the capacity approaches offer near identically 81 Tbps. As d increases, the leverage of the variable bandwidth approach over the standard benchmark becomes more evident due to the absorption effect at the greater ranges. This shows that the THz band promises to be an ideal candidate among drone-to-drone or even from drone-to-ground communications for various practical applications including post disaster monitoring, unexpected traffic demands and war technology, promising capacity values in order of several 100 Gbps.

Fig. 4.8(a) shows the capacity curves for the same settings as in Fig. 4.7(b) considering WF and EP power allocation schemes. As shown by this figure, applying WF in both variable bandwidth and standard approaches provides similar capacity values e.g., 497.7 Gbps at d = 100 m. For the case of the EP allocation, the C_{V-BW} outperforms C_{STD} at the ranges greater than 10 m. For instance, at d = 100 m, C_{V-BW} stands at 117.2 Gbps, which is 83.9 Gbps greater than C_{STD} at the identical range. For analyzing the effect of fading, we consider first BM errors as we obtain the ergodic capacity numerically by averaging capacity computations over 50 realizations of BM fading model as provided in Fig. 4.8(b) considering σ_s/a = 5 (medium) and 10 (worst) with a = 0.1 m [85]. Here, increasing σ_s/a decreases the ergodic capacity substantially. As an example, at d = 100 m and σ_s/a = 10, C^E_{V-BW} with WF is 133.2 Gbps, which is just 26.7 % of the identical approach with the no BM fading case (Fig. 4.8(a)). Similarly, C^E_{V-BW} with EP at d = 100 m and σ_s/a = 10 is 21 Gbps, i.e., a considerable 96.2 Gbps capacity decline as compared to the no BM fading case. With the EP allocation, still, the C^E_{V-BW} outperforms the C^E_{STD}.

Next, we assess additional impact MP effect and in Fig. 4.8(c), we present the ergodic capacity (average of 50 channel realizations), considering MP fading model with α = 2, μ = 1 i.e., pure NLOS (Rayleigh) case and for α = 2, μ = 3 case (where a weak LOS component present), each applied with BM fading with σ_s/a = 5. In general, increasing μ from 1 to 3, which implies an improved LOS component, increases the ergodic capacity by 17 % for both the C^E_{V-BW} and C^E_{STD} computations with WF, 28.07 % for C^E_{V-BW} with EP and 14.8 % for C^E_{STD} with EP, each at d = 100 m. Furthermore, the ergodic capacity curves in Fig. 4.8(c) offer lower values as compared to the only BM fading case (Fig. 4.8(b) with σ/a = 5). For example, at d = 100 m, C^E_{V-BW} with EP with μ = 1 offers 28.89 Gbps, while with the case of no MP fading (Fig. 4.8(b), it stands at 49.15 Gbps. Finally, it can be concluded from (Fig. 4.8(b)) and (Fig. 4.8(c)) that for the Dr2Dr scenario, the BM fading poses a more severe deteriorating impact on the ergodic capacity as compared to the MP fading.

Jet Planes

Another possible communication scenario over the THz band (0.75-10 THz) is among cruising jet planes, flying at an altitude of 10 km and above, which is the boundary of troposphere and stratosphere [33]. We consider the Jet Plane-to-Jet Plane (J2J) communication scenario, where a Tx jet plane is cruising at z_1 = 10 km, while the Rx jet plane is at a radial transmission distance, d and varying θ_{ZA} (hence varying z_2) observed for the same four weather profiles (as drones). P_T = 37 dBm as in [80] and $G_T = 80$ dBi [91]. Fig. 4.9(a) provides the channel capacity (with no fading) with EP allocation as the function of θ_{ZA} at $d = 1$ km. Due to lower water vapor concentration across 10 km altitudes in all four considered weather profiles as previously shown in Fig. 2.3(b), capacity values in the order of tens of Tbps are realizable for this scenario. Precisely, highest capacity values are observed at $\theta_{ZA} = 0°$ by the Mid Latitude Winter weather profile, which are 23.37 Tbps and 22.62 Tbps using C_{V-BW} and C_{STD}, respectively. Evidently, increasing θ_{ZA} from 0° towards 180° exhibits a capacity declining trend, which is justifiable by the fact that establishing the THz band communication towards higher altitudes costs lower absorption loss as compared to the transmission towards the lower altitudes. Similarly for the two weather profiles of Mid Summer and Tropical, the capacity values of both the C_{V-BW} and C_{STD} approaches are fairly close, converging to a value of about 4.5 Tbps as θ_{ZA} approaches 180°. This depicts that employing the constant narrowband i.e. , the standard approach starts approximating the capacity curves of the proposed variable bandwidth approach due to the negligible absorption gain contributions, promising the THz band to establish large data rate links in the order of 10 s of Tbps among cruising jet planes. Fig. 4.9(b) provides the J2J capacity with EP allocation vs. d at $\theta_{ZA} = 90°$ (horizontal). Capacity values of greater than 1.3 Tbps are achievable at $d = 2$ km and 20 Gbps even at $d = 10$ km. This highlights that the THz band can be effectively employed among cruising jet planes, establishing high data rate links at practical transmission ranges.

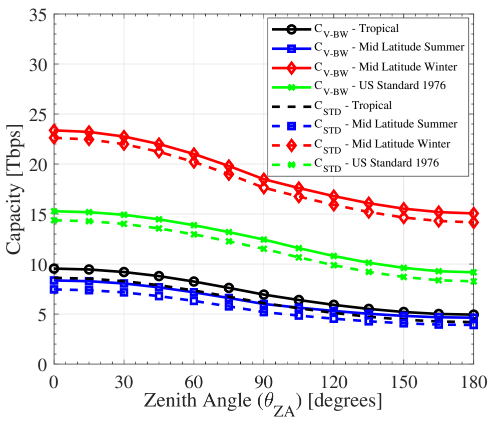

(a) Capacity vs. zenith angle: $z_1 = 10$ km, $d = 1$ km.

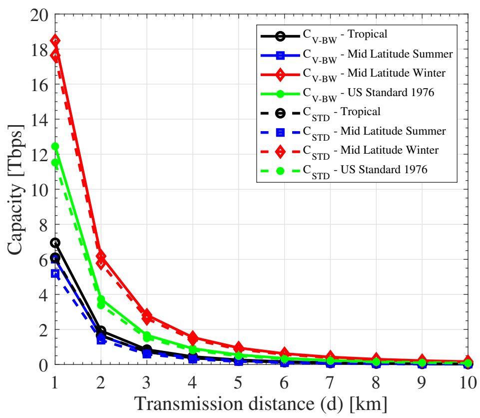

(b) Capacity vs. distance: $z_1 = z_2 = 10$ km, $\theta_{ZA} = 90°$.

Figure 4.9 J2J communication (no fading): Capacity analysis considering variable bandwidth and standard approaches with EP allocation. Four weather profiles are considered in LBLRTM.

Fig. 4.10(a) provides the capacity results with C_{V-BW} and C_{STD} approaches employing WF and EP allocation schemes for the J2J communication scenario, considering no fading and BM fading channels. Similar to Fig. 4.9(b), the capacity

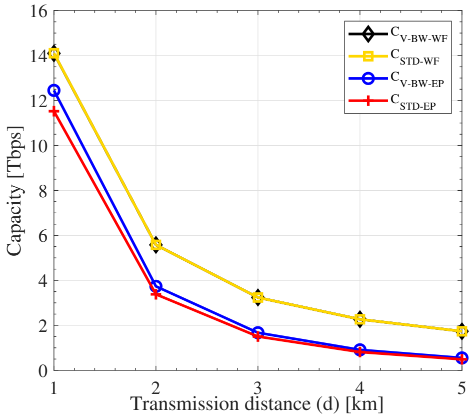

(a) Capacity under no fading.

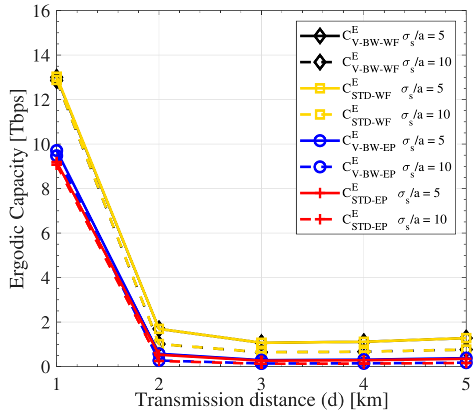

(b) Ergodic capacity under BM fading.

Figure 4.10 J2J communication (without and with fading): Capacity vs. distance considering variable bandwidth and standard approaches with WF and EP allocations. US Standard 1976 weather profile is set in LBLRTM with $z_1 = z_2 = 10$ km, $\theta_{ZA} = 90°$.

drastically decreases, as the range is increased to the order of kilometers. Also, both capacity approaches with WF depict similar values, standing at 13 Tbps at $d = 1$ km, which is 50% above that of the capacity results with EP. In Fig. 4.10(b) ergodic capacity is obtained by BM fading model with $\sigma_s/a = 5$ and 10 with $a = 0.5$ m [92] (again providing results which were averaged over 50 realizations). Numerically, at $d = 2$ km with $\sigma_s/a = 5$, ergodic capacity of C_{V-BW} with EP stands at 0.54 Tbps, while it is 3.734 Tbps with no fading (Fig. 4.10(a)).

UAV

THz band can also be ideal for communicating UAVs and High Altitude Platform (HAPs), which typically fly across 16 km altitude and above, i.e. , across the stratospheric atmospheric region [33]. The altitude on and above 16 km, in particular, observe imperceptible water vapor levels, promising the THz band to be an ideal candidate for Tbps links among various realistic UAV scenarios [3]. We consider such a UAV-to-UAV (U2U) scenario, where the Tx UAV is at $z_1 = 16$ km and the Rx UAV is at a range, d and varying θ_{ZA} range as earlier, hence varying z_2. P_T is set as 30 dBm [81] and G_T as 80 dBi [90]. Fig. 4.11(a) shows the capacity under no fading with EP allocation as the function of θ_{ZA} at $d = 1$ km with the four identical weather profiles as in drones and jet planes scenarios. Interestingly, it can be seen that the capacity curves of all of the four weather profiles closely approximate each other with the C_{V-BW} approach with the US Standard 1976 offering the highest capacity of 36.42 Tbps at $\theta_{ZA} = 0°$ among the other weather profiles. The capacity curves of the standard approach here, closely approximates the variable bandwidth computation, as the absorption is negligible at such a high altitude. Hence, transmitting over the entire THz band (0.75-10 THz) divided into constant narrowbands approximates the common flat bands approach. Fig. 4.11(b) provides the U2U capacity under no fading EP allocation as the function of the transmission range from 1 km up to 10 km considering $\theta_{ZA} = 90°$. Furthermore, it can be noticed that for the entire considered range, the capacity results corresponding to all of the four weather profiles with both the variable bandwidth and standard approaches follow nearly identical exponential decaying trend. This is due to the fact that the altitude of 16 km observe negligible absorption effect due to absence of the water vapor molecules at such a high altitude, promising the THz band to be an ideal communication band candidate among high altitude UAVs and HAPs [69].

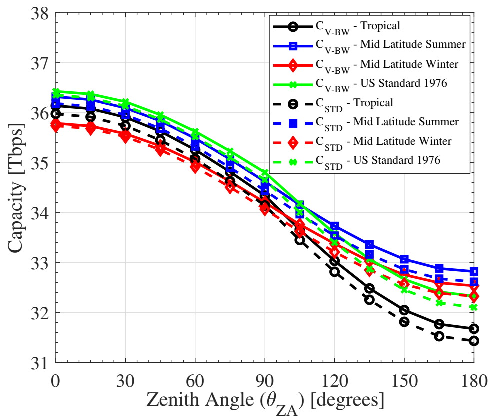

(a) Capacity vs. zenith angle: $z_1 = 16$ km, $d = 1$ km.

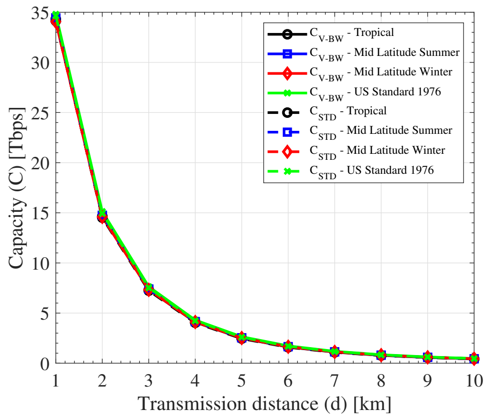

(b) Capacity vs. distance: $z_1 = z_2 = 16$ km, $\theta_{ZA} = 90°$.

Figure 4.11 U2U communication (no fading): Capacity analysis considering variable bandwidth and standard approaches with EP allocation. Four weather profiles are considered in LBLRTM.

Fig. 4.12(a) provides the capacity trend of the U2U scenario, considering both the variable bandwidth and standard approaches with WF and EP allocation schemes for each. Identically to the Dr2Dr and J2J scenario, for both the schemes with WF closely approach their respective EP counter parts, as the atmosphere at 16 km lacks substantial amount of water vapor concentration. Fig. 4.12(b) illustrates the BM fading impact on the ergodic capacity of the U2U scenario. Similar to the scenarios of Dr2Dr and J2J, σ_s/a = 5 and 10 are considered with a = 0.5 m [92]. Clearly, the BM fading significantly degrades capacity. For instance, at d = 2 km with σ_s/a = 5, the ergodic capacity is an order of magnitude smaller than the capacity of no fading case (Fig. 4.12(a)).

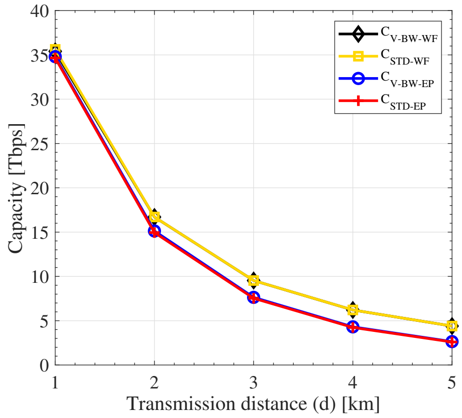

(a) Capacity under no fading.

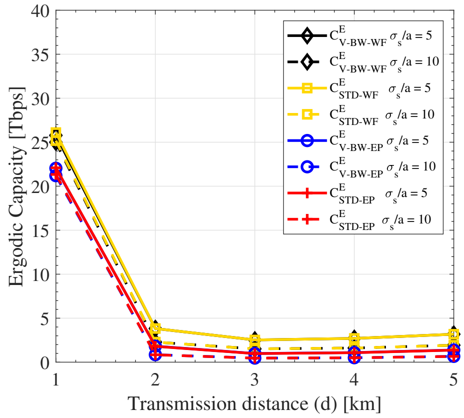

(b) Ergodic capacity under BM fading.

Figure 4.12 U2U communication (without and with fading): Capacity vs. distance considering variable bandwidth and standard approaches with WF and WP allocations. US Standard 1976 weather profile is set in LBLRTM with $z_1 = z_2 = 16$ km, $\theta_{ZA} = 90°$.

Space

As our fourth aerial communication scenario, we consider a possible Space-to-Space (S2S) communication scenario, where a low perigee Tx satellite orbiting at $z_1 = 99$ km is communicating with the Rx satellite at z_2. $P_T = 33.6$ dBm [82] and $G_T = 80$ dBi [90].

Fig. 4.13(a) provides the capacity under no fading with respect to θ_{ZA} at $d = 1$ km. Evidently, due to the lack of atmosphere at such a high altitude, no significant capacity variation is observed among all of the four LBLRTM weather profiles with C_{STD} now offering a negligibly higher capacity of about 0.2 % than C_{V-BW}. This is due to the near negligible absorption across 99 km altitude, the path gain exhibits merely the spread gain with the noise almost flat with a few sharp peaks. Hence, the C_{STD} starts approximating the C_{V-BW} with huge capacity values of greater than 282.5 Tbps being achievable. Furthermore, unlike the U2U scenario, θ_{ZA} variations does not incur perceivable effect on the capacity, further reiterating the absence of atmosphere across the space boundary. Fig. 4.13(b) depicts the capacity vs. distance trend ranging from 1 km to 100 km. Thanks to the THz band, capacity values as high as 221.8 Tbps are achievable even at $d = 10$ km. Even at the largest considered range of 100 km, up to 159 Tbps of capacity is usable. Capacity results of the S2S scenario infer that the THz band is a strong candidate for inter-satellite links (ISL) among conventional satellites [73] and even among cubesats [64], orbiting over the Low Earth Orbit (LEO) as an example, communication links in the order of several hundreds of Tbps.

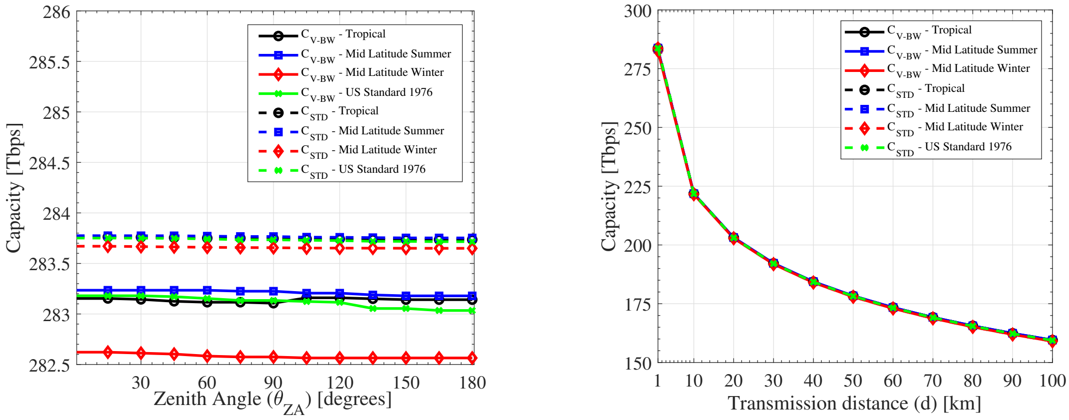

(a) Capacity vs. zenith angle: $z_1 = 99$ km, $d = 1$ km.

(b) Capacity vs. distance: $z_1 = z_2 = 99$ km, $\theta_{ZA} = 90°$.

Figure 4.13 S2S communication (no fading): Capacity analysis considering variable bandwidth and standard approaches with EP allocation. Four weather profiles are considered in LBLRTM.

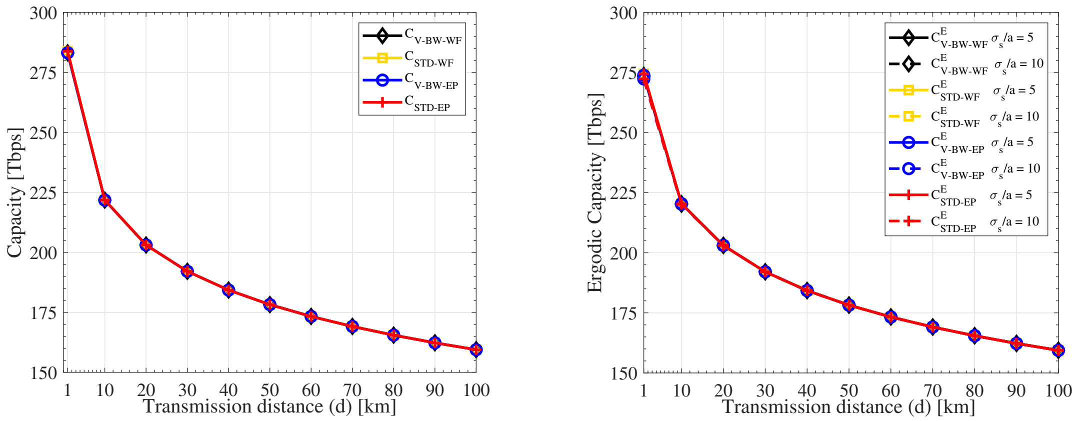

(a) Capacity under no fading.

(b) Ergodic capacity under BM fading.

Figure 4.14 S2S communication (without and with fading): Capacity vs. distance considering variable bandwidth and standard approaches with WF and EP allocations. US Standard 1976 weather profile is set in LBLRTM with $z_1 = z_2 = 99$ km, $\theta_{ZA} = 90°$.

Fig. 4.14(a) depicts the capacity of the proposed variable bandwidth and standard approaches with both the WF and EP allocation schemes under no fading. Evidently, the capacity of all of the four instances offer near identical capacity values varying from 283.7 Tbps to 159.4 Tbps for d ranging from 1 km to 100 km, respectively. For analyzing the impact of the BM fading on the ergodic capacity of the S2S scenario, Fig. 4.14(b) shows the ergodic capacity as the function of the identical transmission range as considered in Fig. 4.14(a), with σ_s/a = 5 and 10, where a = 0.5 m [93, 94]. In this scenario, BM fading slightly reduces the capacity with no fading by about 3.2 % for the variable bandwidth and standard computations. After

10 km range, interestingly, the impact of the BM fading diminishes and the ergodic capacity are close to the capacity values under no fading (Fig. 4.14(a)). This is due to the fact that increasing the transmission range results in a larger Tx beam footprint, w_d, coupled with lower fractional receive power, A_0. When w_d becomes considerably larger than the Rx beam and a given σ_s, forcing the fraction $\zeta = \frac{w_{eq}}{2\sigma_s}$ to a larger value, we end up with no BM fading [95]. For this reason, THz band can be preferred especially for long hauled ISLs [73] and cubesats [64], as link rates in the order of hundreds of Tbps can be provided even under BM fading.

Table 4.1 provides a summary of the capacity and ergodic capacity results of the considered aerial communication scenarios, also considering the sea-level communication [14], under both no fading and fading cases. Clearly, as compared to the no fading cases in each scenario, the BM fading degrades the ergodic capacity of the aerial links by about 3.2 % to 38 % due to random fluctuations. These fluctuations in the communicating aerial vehicles mainly induce Tx-Rx antenna gain mismatches, which should be kept minimized, although can not be completed eliminated in practical aerial links [96]. One way to minimize the BM fading effect is to employ Tx-Rx antenna stabilizers into the communicating aerial vehicles [30]. Another way to subside the BM fading impact is to provision higher transmit power levels, causing the Tx antenna to collect more of the transmitted power [21]. Moreover, both the approaches with WF power allocation exhibits similar ergodic values, with the standard approach narrowly outperforming the proposed variable bandwidth approach by 0.21 % to 6.37 %. However, it is evident that under the EP allocation, the ergodic capacity of the variable bandwidth approach under both the BM fading and the MP fading outperforms its standard counterpart by 80 % and 32 % at sea-level and 100 m altitude (drones), respectively. Finally, it can be concluded that even under the BM fading, the ergodic values of several 10s of Tbps are realizable for J2J and U2U scenarios, and even up to several 100s of Tbps for the S2S, truly depicting the potential of the THz band for aerial communications.

In this chapter, we have provided an extensive analysis of the THz band (0.75-10 THz) communication for four practical aerial vehicle scenarios, namely, drones, jet planes, high altitude UAVs, and satellites, at various practical altitudes, transmission distances, zenith angles, and considering fading conditions of MP fading and BM fading. Incorporating LBLRTM, a channel model for aerial communications at THz band has been obtained to calculate frequency-selective path gain and the colored noise spectrums, where both are severely affected by the water vapor concentrations across the atmosphere. We have also proposed a novel approach for computing THz capacity by considering only the common flat-bands among the path gain and the noise PSD, in comparison with the standard approach based on only flat channel

Table 4.1 Capacity and ergodic capacity (in Tbps) for horizontal aerial communication scenarios in comparison with horizontal sea-level communication under US Standard 1976 weather profile, $\alpha = 2$, $\mu = 1$ for MP fading and $\sigma_s/a = 5$ for BM fading.

Capacity computation [Tbps]	**Power allocation**	**Sea-level** $z_1 = z_2 =$ **0 km** $d =$ **10 m**		**Drones** $z_1 = z_2 =$ **0.1 km** $d =$ **10 m**		**Jet Planes** $z_1 = z_2 =$ **10 km** $d =$ **1 km**		**UAVs** $z_1 = z_2 =$ **16 km** $d =$ **1 km**		**Satellites** $z_1 = z_2 =$ **99 km** $d =$ **1 km**	
		Capacity (No Fading)	**Ergodic Capacity (MP Fading and BM Fading)**	**Capacity (No Fading)**	**Ergodic Capacity (MP Fading and BM Fading)**	**Capacity (No Fading)**	**Ergodic Capacity (BM Fading only)**	**Capacity (No Fading)**	**Ergodic Capacity (BM Fading only)**	**Capacity (No Fading)**	**Ergodic Capacity (BM Fading only)**
V-BW	**WF**	1.24	1.02	8.19	5.88	14.10	13.00	35.40	25.78	283.10	273.80
STD		1.26	1.04	8.72	6.28	14.10	13.03	35.62	26.10	283.70	274.40
V-BW	**EP**	0.45	0.32	7.51	4.65	12.45	9.70	34.80	22.04	283.10	273.80
STD		0.25	0.17	5.74	3.51	11.53	9.20	34.65	22.09	283.70	274.40

response, both considered with WF and EP allocations.

The capacity analysis points out that the THz channel capacity without fading is improved under both WF and EP allocations at higher atmospheric altitudes: For both the proposed and the standard approaches, the sea-level capacity is enhanced by an order of magnitude for the drones, which is doubled for the jet plane scenario, which is further tripled for UAVs, which is again increased by another order of magnitude for the space communications. When ergodic capacity is computed for the fading scenarios, it is shown that the impact of fading vanishes at higher altitudes. Sea-level ergodic capacity is increased by an order of magnitude for drone-to-drone communications, providing several Tbps at 10 m, while 10s of Tbps is achievable among jet planes and UAVs, and several 100s of Tbps is possible for satellites/cubesats at 1 km under fading, suggesting that THz band is a promising alternative for aerial communications. The BM fading can be minimized by employing Tx-Rx antenna stabilizers, or by increasing the transmit power levels. Nevertheless, for the longer ranges, the BM fading diminishes as the Tx beam footprint becomes larger than the Rx beam.

Having presented the THz capacity of various aerial communication cases by considering the colored noise model and practical physical parameters under both ideal and fading channel environments, exploitation of the large THz bandwidth in a cognitive fashion and the problem of beam misalignment under mobility for a special case aerial vehicles, i.e., drones are covered in the Chapter 5 of this dissertation.

Chapter 5

CHANNEL SELECTION SCHEME FOR TERAHERTZ-ENABLED DRONE COMMUNICATIONS

In this chapter, drones for THz communications are considered under various mobility instances. Similar to Chapter 3 and Chapter 4, LBLRTM tool is employed for obtaining realistic transmittance values at various altitudes, ranges and directions of communications. First, a 3D communication model of THz-enabled Dr2Dr link is considered, with Tx-Rx misalignment instances due to mobility. Then, a capacity maximization problem is formulated by jointly selecting THz channels and the Tx-Rx 3D antenna beamwidths of a realistic 3D sectored antenna model. Subsequently, a channel selection scheme is proposed for solving the capacity maximization problem. Finally, for various realistic Dr2Dr mobility scenarios, the proposed channel selection scheme is compared in terms of capacity and spectral efficiency with the CFB and STD approaches under both WF and EP allocations. Furthermore, real mobility traces and practical THz antennas are considered for truly revealing the potential of THz band for drone communications.

We consider realistic THz band Dr2Dr communication, where a drone Tx is at an altitude, z_{Tx}, transmitting to another drone Rx at z_{Rx} altitude over a transmission distance, d as shown in Fig. 4.1. The Rx drone can be at an arbitrary zenith angle, ϕ_{Rx} from the transmitter, which varies from $0°$ to $180°$, indicating vertically-up and vertically-down directions, respectively, as depicted in Fig. 4.2.

5.1 Channel Model

As presented in Chapter 4, we consider the channel model among drones without fading, i.e., LOS channel. Therefore, with $h = h_l$ into (4.1), the SNR at time, t, γ^t across the k^{th} narrowband, where k = 1, 2, 3...K across the THz band (0.75-4.4 THz) can be expressed as

$$\gamma^t(f_k, z_{Tx}, z_{Rx}, d, (\Delta f)) = \frac{P^k_{Total}\ |h(f_k, z_{Tx}, z_{Rx}, d)|^2\ G^t_{Total}}{P_n(f_k, z_{Tx}, z_{Rx}, d, (\Delta f))}\ , \tag{5.1}$$

where P^k_{Total} refers to the transmit power of the k^{th} narrowband (i.e. , (Δf)), while P_{Total} denotes the total transmit power in Watts. Evidently, the γ computation would vary with respect to a chosen power allocation, which are explained in the following in detail. $|h(f_k, z_{Tx}, z_{Rx}, d)|^2$ is the path gain derived from (4.2), P_n denotes the noise power in Watts across (Δf) from (4.11), and G^t_{Total} is the total antenna gains (Tx and Rx antennas combined).

In this chapter, identical directive antennas are considered both at the Tx and Rx with narrow Tx-Rx beams pointing towards each other, which may get misaligned due to mobility of the Tx and Rx drone, as depicted in Fig. 5.1. For obtaining G^t_{Total} for γ^t computations in (5.1), in the following, we consider 3D and 2D sectored antenna models for realistic directional THz propagation, in detail.

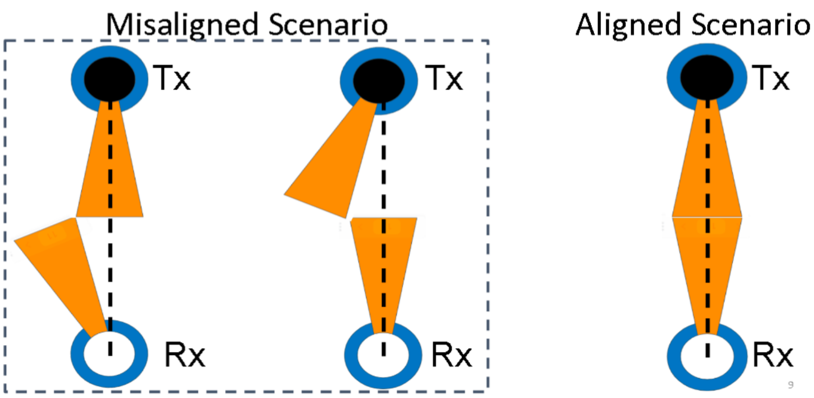

Figure 5.1 Illustration of Tx-Rx antenna boresights under misalignment and perfect alignment.

5.2 Antenna Models

For incorporating the effect of mobility on Tx and Rx antenna beam misalignment and its subsequent effect on SNR computations, we consider sectored 3D antenna model and sectored 2D antenna modelfor realizing high gain THz Tx and Rx beams.

In what follows, we provide computations of the total antenna gains based on different antenna alignments due to mobility by employing each of the two antenna model.

5.2.1 Sectored 3D Antenna Model

We consider the 3D sectored antenna model for the antenna gain computations [97]. The gain can be computed as: 1) Significant sidelobe gain and 2) Negligible sidelobe gain.

Without Side Lobe Gain

In this model, the antenna is able to transmit in 3D, i.e., in all six directions. The gain is high in a direction specified by 3D elevation and azimuth beamwidths, while for the other directions, a low sidelobe gain is defined. Mathematically,

$$G_{\psi^t_{\phi-Tx},\psi^t_{\theta-Tx}} = \begin{cases} \frac{4\pi}{\psi^t_{\phi-Tx}\psi^t_{\theta-Tx}}, & if\left|\Delta\phi^t_{Rx-Tx}\right| \leq \frac{\psi^t_{\phi-Tx}}{2} \; and \; \left|\Delta\theta^t_{Rx-Tx}\right| \leq \frac{\psi^t_{\theta-Tx}}{2}. \\ z, & otherwise \end{cases} \tag{5.2}$$

Similarly, the antenna gain of the receiver is obtained as,

$$G_{\psi^t_{\phi-Rx},\psi^t_{\theta-Rx}} = \begin{cases} \frac{4\pi}{\psi^t_{\phi-Rx}\psi^t_{\theta-Rx}}, & if\left|\Delta\phi^t_{Rx-Tx}\right| \leq \frac{\psi^t_{\phi-Rx}}{2} \; and \; \left|\Delta\theta^t_{Rx-Tx}\right| \leq \frac{\psi^t_{\theta-Rx}}{2}. \\ z, & otherwise \end{cases} \tag{5.3}$$

where $G_{\psi^t_{\phi-Tx},\psi^t_{\theta-Tx}}$ and $G_{\psi^t_{\phi-Rx},\psi^t_{\theta-Rx}}$ denote the antenna gains of the transmitter and the receiver, respectively, at time, t, $\psi^t_{\phi-Tx}$ $\psi^t_{\theta-Tx}$ are the elevation and azimuth beamwidths of the transmitter, and $\psi^t_{\phi-Rx}$ $\psi^t_{\theta-Rx}$ are the elevation and azimuth beamwidths of the receiver. $\Delta\phi^t_{Tx-Rx}$, $\Delta\theta^t_{Tx-Rx}$, are the angular differences (elevation and azimuth, respectively) of the transmit and the receive antennas with respect to the bore-sight lines, and z is the gain of side lobe level over a range of $0 \leq z \ll 1$.

With Side Lobe Gain

In this model, a high gain mainlobe antenna gain is considered. Therefore, the sidelobe antenna gain subtraction from the main lobe gain can be neglected. Mathematically,

$$G_{\psi^t_{\phi-Tx},\psi^t_{\theta-Tx}} = \begin{cases} \frac{4\pi-(4\pi-\psi^t_{\phi-Tx},\psi^t_{\theta-Tx})z}{\psi^t_{\phi-Tx}\psi^t_{\theta-Tx}}, & if\left|\Delta\phi^t_{Rx-Tx}\right| \leq \frac{\psi^t_{\phi-Tx}}{2} \; and \; \left|\Delta\theta^t_{Rx-Tx}\right| \leq \frac{\psi^t_{\theta-Tx}}{2}. \\ z, & otherwise \end{cases} \tag{5.4}$$

Likewise, the antenna gain of the receiver is obtained as,

$$G_{\psi^t_{\phi-Rx},\psi^t_{\theta-Rx}} = \begin{cases} \frac{4\pi-(4\pi-\psi^t_{\phi-Rx},\psi^t_{\theta-Rx})z}{\psi^t_{\phi-Rx}\psi^t_{\theta-Rx}}, & if\left|\Delta\phi^t_{Rx-Tx}\right| \leq \frac{\psi^t_{\phi-Rx}}{2} \; and \; \left|\Delta\theta^t_{Rx-Tx}\right| \leq \frac{\psi^t_{\theta-Rx}}{2}. \\ z, & otherwise \end{cases} \tag{5.5}$$

5.2.2 Sectored 2D Antenna Model

We also consider the well-known 2D sectored antenna model for the antenna gain computations [98]. 2D sectored antenna is a slice of a 3D sectored antenna at a given planar direction. Here, the antenna gain of the transmitter is given as;

Without Side Lobe Gain

$$G_{\psi^t_{\theta-Tx}} = \begin{cases} \frac{2\pi}{\psi^t_{\theta-Tx}}, & if\left|\Delta\theta^t_{Rx,Tx}\right| \leq \frac{\psi^t_{\theta-Tx}}{2}. \\ z, & otherwise \end{cases} \tag{5.6}$$

Likewise, the antenna gain of the receiver is obtained as,

$$G_{\psi^t_{\theta-Rx}} = \begin{cases} \frac{2\pi}{\psi^t_{\theta-Rx}}, & if\left|\Delta\theta^t_{Rx,Tx}\right| \leq \frac{\psi^t_{\theta-Rx}2}{,} \\ z, & otherwise \end{cases} \tag{5.7}$$

With Side Lobe Gain

$$G_{\psi^t_{\theta-Tx}} = \begin{cases} \frac{2\pi-\left(2\pi-\psi^t_{\theta-Tx}\right)z}{\psi^t_{\theta-Tx}}, & if\left|\Delta\theta^t_{Rx,Tx}\right| \leq \frac{\psi^t_{\theta-Tx}}{2}. \\ z, & otherwise \end{cases} \tag{5.8}$$

Similarly, the antenna gain of the receiver is obtained as,

$$G_{\psi^t_{\theta-Rx}} = \begin{cases} \frac{2\pi-\left(2\pi-\psi^t_{\theta-Rx}\right)z}{\psi^t_{\theta-Rx}}, & if\left|\Delta\theta^t_{Rx,Tx}\right| \leq \frac{\psi^t_{\theta-Rx}}{2}, \\ z, & otherwise \end{cases} \tag{5.9}$$

In this chapter, we consider sidelobe gain as $z = 0.1$ for Tx and Rx each. Hence, the effect of subtracting the side lobe gain from the main lobe gain is negligible. Therefore, we consider the 3D sectored antenna model with symmetric beamwidths of Tx and Rx each, without side lobe gain subtraction. Additionally, the 3D sectored antenna model with asymmetric Tx and Rx beamwidths are also presented for an example scenario of drone mobility. Moreover, for the comparison purposes, the 2D antenna model is also considered for the ideal mobility scenario, i.e., perfectly aligned mobility, as discussed later in Section 5.4 of this chapter.

$$G^t_{Total} = (G_{\psi^t_{\phi-Tx},\psi^t_{\theta-Tx}})\ (G_{\psi^t_{\phi-Rx},\psi^t_{\theta-Rx}})\ . \tag{5.10}$$

In dB,

$$G^t_{Total}[dB] = 10log_{10}(G^t_{Total})\ . \tag{5.11}$$

We assess capacity, over the THz band (0.75-4.4 THz) between the Dr2Dr link by considering the realistic channel model as discussed in Section 5. The LBLRTM tool is employed to obtain the THz transmittance values, $\tau(f, T(z_{Tx}, z_{Rx}), v(z_{Tx}, z_{Rx}), d)$ for obtaining THz absorption gain and emissivity, as needed in (4.4) for the path gain computations and in (4.9) for the colored noise calculations, respectively, for the realistic THz band Dr2Dr communication scenarios at various elevation/zenith angles, azimuth/horizontal angles, and transmission distances.

The altitude dependent capacity of the CFB scheme, C_{CFB}, at time, t, is given as [15]:

$$\begin{aligned} C^t_{CFB}(z_{Tx}, z_{Rx}, d) &= \sum_{m=1}^{M} (\Delta f)_m\ log_2\left[1 + \gamma^t(f_m, z_{Tx}, z_{Rx}, d, (\Delta f)_m)\right] \\ &= \sum_{m=1}^{M} (\Delta f)_m\ log_2\left[1 + \frac{P^m_{Total}\ |h(f_m, z_{Tx}, z_{Rx}, d)|^2\ G^t_{Total}}{P_n(f_m, z_{Tx}, z_{Rx}, d, (\Delta f)_m)}\right]\ . \end{aligned} \tag{5.12}$$

The WF and EP allocation for the CFB scheme is performed as discussed in Chapter 4.

According to the STD scheme, the altitude dependent capacity, C_{STD} at time, t, is computed as:

$$C^t_{STD}(z_{Tx}, z_{Rx}, d) = \sum_{k=1}^{K} \Delta f \ log_2 \left[1 + \frac{P^k_{Total} \ |h(f_k, z_{Tx}, z_{Rx}, d)|^2 \ G^t_{Total}}{P_n(f_k, z_{Tx}, z_{Rx}, d, (\Delta f))}\right] . \tag{5.13}$$

Here f_k is a function of f_m with $k = 1, 2, 3,...,K$. Here, for the STD scheme, WF and EP allocations are performed as provided earlier in Section 4.

Spectral efficiency at a given time, t, $SE^t(z_{Tx}, z_{Rx}, d)$, is defined as the achievable capacity, C^t per unit bandwidth (Hertz here). Mathematically, For the CFB scheme [15],

$$SE^t_{CFB}(z_{Tx}, z_{Rx}, d) = \sum_{m=1}^{M} log_2 \left[1 + \frac{P^m_{Total} \ G^t_{Total}}{L_{pl}(f_m, z_{Tx}, z_{Rx}, d) \ P_n(f_m, z_{Tx}, z_{Rx}, d, (\Delta f)_m)}\right] (bits/sec/Hz), \tag{5.14}$$

For the STD scheme,

$$SE^t_{STD}(z_{Tx}, z_{Rx}, d) = \sum_{k=1}^{K} log_2 \left[1 + \frac{P^k_{Total} \ G^t_{Total}}{L_{pl}(f_k, z_{Tx}, z_{Rx}, d) \ P_n(f_k, z_{Tx}, z_{Rx}, d, (\Delta f))}\right] (bits/sec/Hz), \tag{5.15}$$

5.3 Channel Selection For Capacity Maximization

To maximize the capacity of the THz-enabled Dr2Dr link under mobility, we incorporate various parameters affecting the capacity at a given time, t, such as the 3D coordinates, elevation and azimuth beamwidths, and azimuth and elevation boresight angles of each of the Tx and Rx drones. Additionally, we consider the THz band, B (0.75-4.4 THz) comprising of the narrowbands, each $\Delta \ f = 0.3$ GHz wide, which is the spectral resolution of the LBLRTM tool. For maximizing the THz-enabled Dr2Dr link capacity over the THz band (0.75-4.4 THz), we formulate the capacity maximization problem by considering the THz narrowbands selection as follows:

Given: P_{Total}, $\Omega^{NB}_f \in \ B$, $\Delta \ f$, $(x^t_{Tx}, y^t_{Tx}, z^t_{Tx})$, $(x^t_{Rx}, y^t_{Rx}, z^t_{Rx})$, ϕ°_{Tx}, θ°_{Tx}, ϕ°_{Rx}, θ°_{Rx},

$\psi^{\circ}_{\phi-Tx}, \psi^{\circ}_{\theta-Tx}, \psi^{\circ}_{\phi-Rx}, \psi^{\circ}_{\theta-Rx}$

$$\max_{\Omega^{NB}_{f^K_{i=1}} \in B} C^t . \tag{5.16}$$

The problem in (5.16) requires permutations over all narrowbands channels (each 0.3 GHz wide) across $B = 0.75$-4.4 THz, which is practically impossible considering the state-of-the-art computations. Therefore, we propose an intelligent way of selecting only those channels, $\Omega^{NB}_{f} \in B$, which would provide the maximum capacity for a given set of Tx-Rx beamwidths, in the subsequent subsection.

5.3.1 MaxActive Scheme

For solving the capacity maximization problem (5.16), we propose a novel way of selecting the channels as given in Algorithm 2, which we have termed as MaxActive channel selection scheme. MaxActive is a Brute force search based algorithm for finding the global maxima of the capacity. Initially, we find the narrowband frequency (channel) corresponding to the maximum SNR, and set it as threshold (line 4). Then, we compute the capacity (line 9) considering the initial channel frequency. Afterwards, we lower the SNR threshold (line 10) and consider all those narroband channel frequencies with the SNR above the updated threshold SNR. These frequencies are named as active frequencies. Next, we find capacity considering all the active frequencies. This process (line 7-11) is repeated till the threshold reaches zero. Finally, we find the maximum capacity among all the capacity values (line 13) that have been computed corresponding to the each considered threshold. This is depicted in Fig. 5.2, where it can be seen that for each iteration j, initially, the capacity is increasing up to a global maxima, after which the capacity values decline, until completing the algorithm loop index, j. Moreover, the MaxActive algorithm returns all the active channels corresponding to the maximum capacity (line 13).

To this end, we have formulated the Dr2Dr link capacity maximization problem in (5.16), which is solved using the proposed MaxActive channel selection algorithm.

For performing the beamwidth adaption, we consider 3D symmetric beams (5.2) and (5.3) by increasing the elevation, azimuth beamwidths of both the Tx and Rx drone antennas, so that the THz communication is sustained within the main lobe of both Tx and Rx under mobility. However, the beamwidth adaptation has a trade-off: On one hand, increasing the beamwidths promises the THz Dr2Dr link within the high gains of the Tx, Rx main lobes as compared to the very low gain of the side spherical lobes. On the other hand, increasing the beamwidths decrease the total

Algorithm 2: MaxActive channel selection scheme for the capacity maximization.

$\Delta f,\ \Delta s$
z_{Tx}, z_{Rx}, d
$j = 1$
$f_\circ \leq f \leq f_K$
$s_j = max\ (\gamma(f, z_{Tx}, z_{Rx}, d, \Delta f))$
$C(j-1) = 0$
while $j\ \leq\ K$ **do**
  Find $f : \gamma(f, z_{Tx}, z_{Rx}, d, \Delta f)\ \geq s_j$
  $C(j) = \sum_{i=1}^{j} \Delta f\ \ log_2(1 + \gamma(f_i, z_{Tx}, z_{Rx}, d, \Delta f))$
  $s_j \leftarrow s_j - \Delta s$
  $j\ =\ j+1$
end
end while
Return $max(C(i) \mid \{i = 1, ..., K\})$

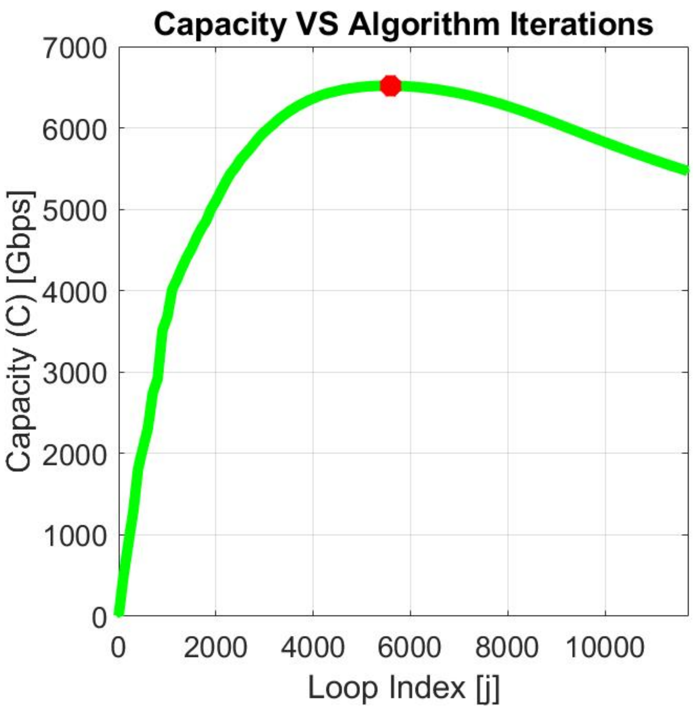

Figure 5.2 Visual depiction of the global maxima of the THz-enabled Dr2Dr link capacity via MaxActive algorithm iterations.

antenna gains.

5.3.2 Joint Channel Selection, Beamwidth Adjustment and Power Control

The problem in (5.16) requires only the channel selection for maximizing the THz-enabled Dr2Dr link capacity, which is solved using the proposed MaxActive Algorithm. However, due to the mobile nature of the drones, the Tx and Rx THz beams can frequently get misaligned, causing to degrade the capacity at a given time instant, t. Hence, the Tx and Rx beamwidth adaptation with respect to the drone mobility will ensure higher capacity values as compared to the fixed beamwidths. Additionally, due to the distance-dependent nature of the THz transmission windows (channels), controlling the transmit power levels of each channel will also promise larger capacity values as compared to the equal power allocation. Therefore, in the following, we provide a joint channel selection, beamwidth adjustment and power control for maximizing the Dr2Dr link capacity, considering that the total antenna gain is independent, whereas the channel selection is dependent on the total antenna gains. we formulate the capacity maximization problem by considering the joint channel selection, beamwidth adjustment, and power control as follows:

Given: P_{Total}, $\Omega_f^{NB} \in B$, Δf, $(x_{Tx}^t, y_{Tx}^t, z_{Tx}^t)$, $(x_{Rx}^t, y_{Rx}^t, z_{Rx}^t)$, ϕ_{Tx}°, θ_{Tx}°, ϕ_{Rx}°, θ_{Rx}°, $\psi_{\phi-Tx}^{\circ}$, $\psi_{\theta-Tx}^{\circ}$, $\psi_{\phi-Rx}^{\circ}$, $\psi_{\theta-Rx}^{\circ}$

$$\max_{\Omega_{f_{i=1}^K}^{NB} \in B, \psi_{\phi,\theta-Tx}, \psi_{\phi,\theta-Rx}, P_{Total}^i} C^t , \tag{5.17a}$$

$$s.t. \quad \psi_{\phi-Tx}^{\circ}, \psi_{\theta-Tx}^{\circ} \leq \psi_{\phi-Tx}^{t}, \psi_{\theta-Tx}^{t} \leq \psi_{\phi-Tx}^{max}, \psi_{\theta-Tx}^{max} , \forall\, t \in T \tag{5.17b}$$

$$s.t. \quad \psi_{\phi-Rx}^{\circ}, \psi_{\theta-Rx}^{\circ} \leq \psi_{\phi-Rx}^{t}, \psi_{\theta-Rx}^{t} \leq \psi_{\phi-Rx}^{max}, \psi_{\theta-Rx}^{max} , \forall\, t \in T \tag{5.17c}$$

$$s.t. \quad \sum_{i=1}^{K} P_{Total}^i \leq P_{Total} \tag{5.17d}$$

For solving the problem in (5.17), we propose a step-by-step process of the joint beamwidth adaptation, power control and channel selection as shown in Flowchart. 5.3. The joint process starts with the first step of the beamwidth adaptation of both the Tx and Rx drone antennas. This process, as described earlier, involves broadening the elevation and azimuth beamwidths of both the Tx (hovering) and Rx (mobile) drone antennas, so as to keep the THz Dr2Dr link under mobility to communicate over the main lobe at the cost of losing some of the total antenna gains. Based on the adjusted beamwidths, at the end of this first step,

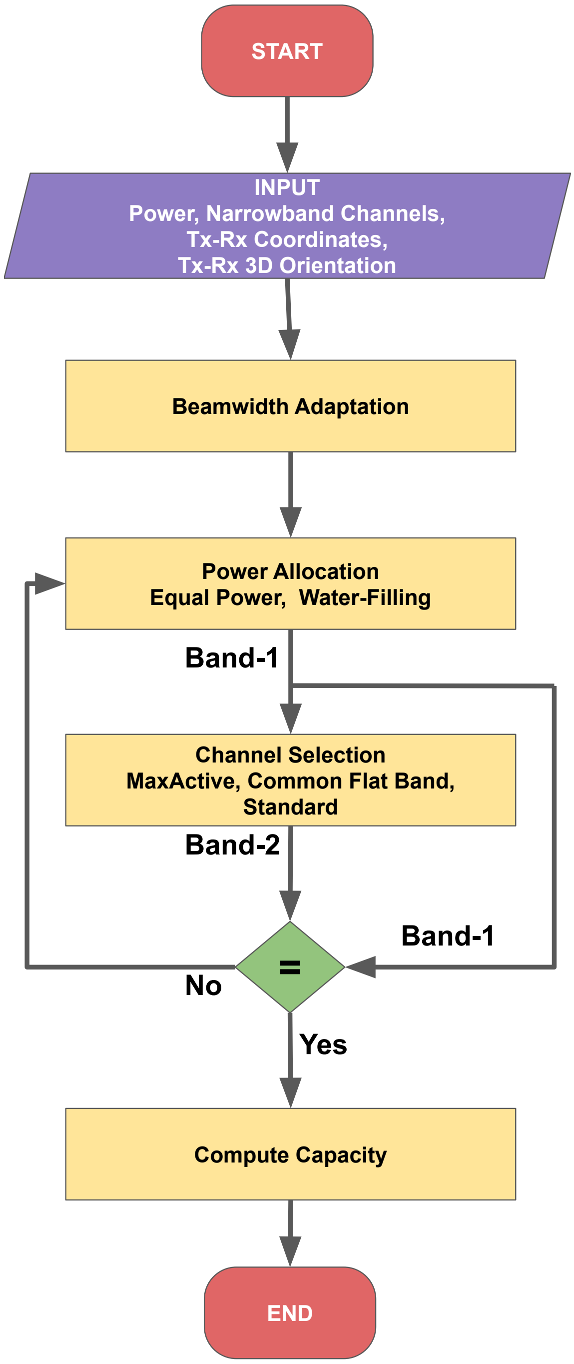

Figure 5.3 Joint channel selection, beamwidth adjustment and power control for the capacity maximization of the THz band Dr2Dr communication: The total antenna gain is independent of selected bandwidth for capacity maximization, while bandwidth selection is dependent on the total antenna gain.

the total antenna gain at time, t is evaluated, which is provided to the second step of power allocation choice, i.e, EP or WF. The EP allocation distributes the total transmit power equally over all the constant narrowbands across 0.75-4.4 THz, whereas the WF, in addition to the optimal power allocation over the narrowbands, also at times, deselect some of the narrowbands, which are usually at very high THz absorption peaks. All in all, the selected bands, called as Band-1, are provided to the MaxActive, CFB, or STD scheme, whichever is selected. MaxActive, as described above, selects only those narrowbands, which provide the maximum capacity. CFB, as proposed earlier in [15], considers common flat bands (which are sets of narrowbands within itself) between the total path gain and noise power spectral density. STD, the benchmark scheme, considers all narrowbands across 0.75-4.4 THz. At the end of this 3rd step, again we select a set of narrowbands, called as Band-2. Here, Band-1 and Band-2 are compared till Band-1 is equal to Band-2, thus providing us the optimal channels, adjusted total antenna gains, and optimal power, all of which are utilized to compute the sum capacity of the THz-enabled Dr2Dr link.

5.4 Performance Under Mobility

Having formulated the joint channel selection, beamwidth adjustment and power control for the capacity maximization of the THz band Dr2Dr communication, in the following section, we consider four realistic mobility scenarios of THz Dr2Dr link, including: (1) Perfectly aligned scenario, (2) Misaligned scenario via diagonal mobility, (3) Misaligned scenario via mobility over azimuth, and (4) Misaligned scenario via mobility over elevation. We assess the performance of THz-enabled Dr2Dr link under the mobility scenarios by evaluating channel capacity and spectral efficiency. Moreover, we also consider real mobility traces for the Dr2Dr link as our fifth scenario. Finally, real THz antennas available over the THz band (0.75-4.4 THz) are also employed under three different mobility scenarios to reveal the potential of THz band for drone communications.

5.4.1 Scenario 1: Perfectly Aligned Scenario

As the ideal, benchmark Dr2Dr mobility scenario, we consider the Tx drone hovering at (0 m,10 m,100 m), while the Rx drone hovering initially at (0 m,11 m,100 m) starts moving away from the Tx drone at V_y 10 m/s as shown in Fig. 5.4(a), whereas the Fig. 5.4(b) shows the Tx-Rx distance from $t = 0$ sec up to $t = 10$ sec. The 3D sectored antenna model is considered with symmetric elevation and azimuth beamwidths for the Tx, Rx drones, which are set as 10° at $t = 0$ sec.

Fig. 5.5(a) and Fig. 5.5(b) depict the trend of the beamwidths and the resulting total

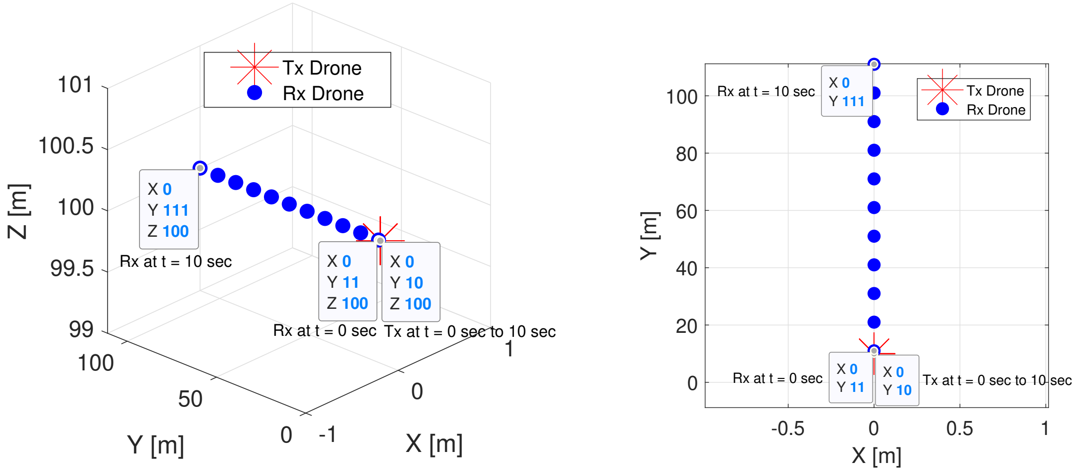

(a) Tx and Rx drones in 3D

(b) Tx and Rx drones in 2D

Figure 5.4 Perfectly aligned scenario: Tx drone is hovering while Rx drone is moving away from Tx.

antenna gains for the perfectly aligned scenario with 3D and 2D sectored antenna models, respectively. It can be seen that due to the perfect alignment of Tx-Rx drones at all t, the transmission is maintained in the initially set 10° azimuth and elevation beamwidths of the Tx and Rx drones, resulting in the total antenna gain of around 52 dB for the 3D antenna model, while it is about 30 dB for the 2D antenna model.

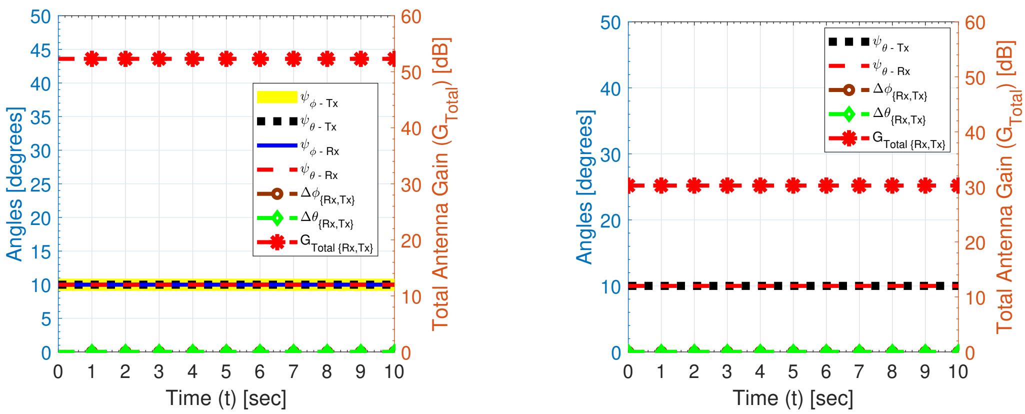

(a) 3D sectored antenna model with symmetric beamwidths

(b) 2D sectored antenna model

Figure 5.5 Trend of the Tx, Rx beamwidths, Tx, Rx boresight differences, and the corresponding total antenna gains for the perfectly aligned mobility scenario.

Fig 5.6 and Fig. 5.7 show the frequency bands with 3D symmetric antenna model and 2D antenna model, respectively, which are obtained using the three considered bandwidth selection schemes with the WF and EP for each. For the case of Max-Active, it can be observed that the bands obtained using both the WF and EP allocation schemes closely approximate each other particularly at the transmission distances greater than 1 m. This is because in the MaxActive scheme, the channels are iteratively selected based on high SNR values, even for the EP, till the maximum capacity is achieved, while the WF is readily the optimal solution for the capacity maximization. From this, we can infer that by using MaxActive, even employing the EP promises the near optimal capacity. For the case of the CFB scheme, WF provides similar bands as compared to the MaxActive approach with WF, as the CFB scheme initially eliminates the high absorption bands, while CFB with EP provides bands with intermittent discontinuities, where the absorption peaks are present. Finally, for the STD scheme, the bands with WF are identical as compared to the MaxActive with WF. Moreover, with EP, the STD scheme considers all narrowbands over 0.75-4.4 THz, which is trivial. However, this is the most inefficient way of channel selection over the THz band, as the channels with the absorption peaks are also selected for transmission, leading to a substantial degradation in the channel capacity.

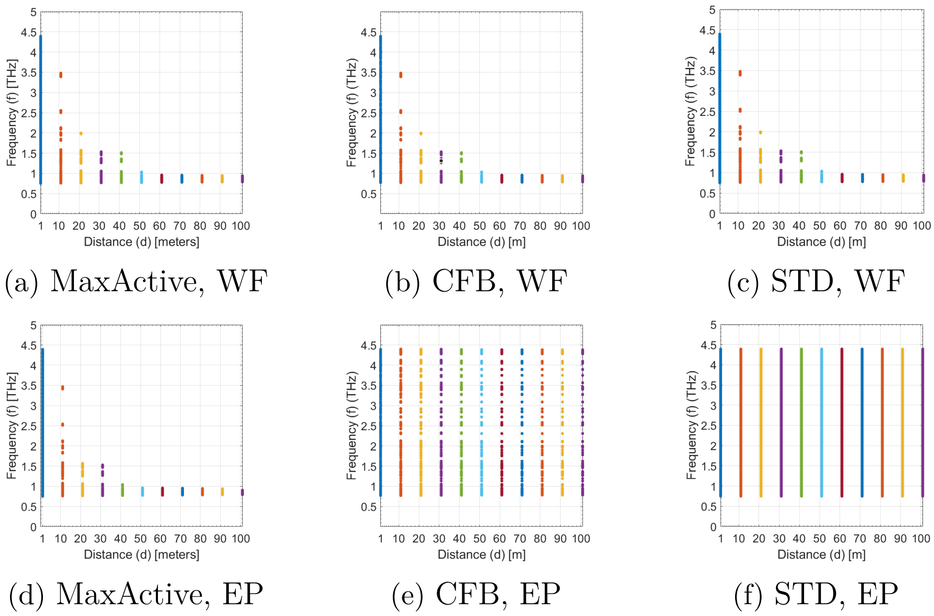

(a) MaxActive, WF (b) CFB, WF (c) STD, WF

(d) MaxActive, EP (e) CFB, EP (f) STD, EP

Figure 5.6 Selected bands for the perfectly aligned scenario with 3D symmetric antenna model.

5.4.2 Scenario 2: Misaligned Scenario via Diagonal Mobility

As the second mobility scenario for THz-enabled Dr2Dr link, we consider the Tx drone hovering at (0 m, 10 m, 100 m) for all observed time instances, i.e., from $t =$ 0 sec to 100 sec, while the Rx drone, which is initially hovering at (0 m, 11 m, 100 m), starts moving away diagonally from the Tx drone, maintaining a step of 10 m at each t, as shown in Fig. 5.8.

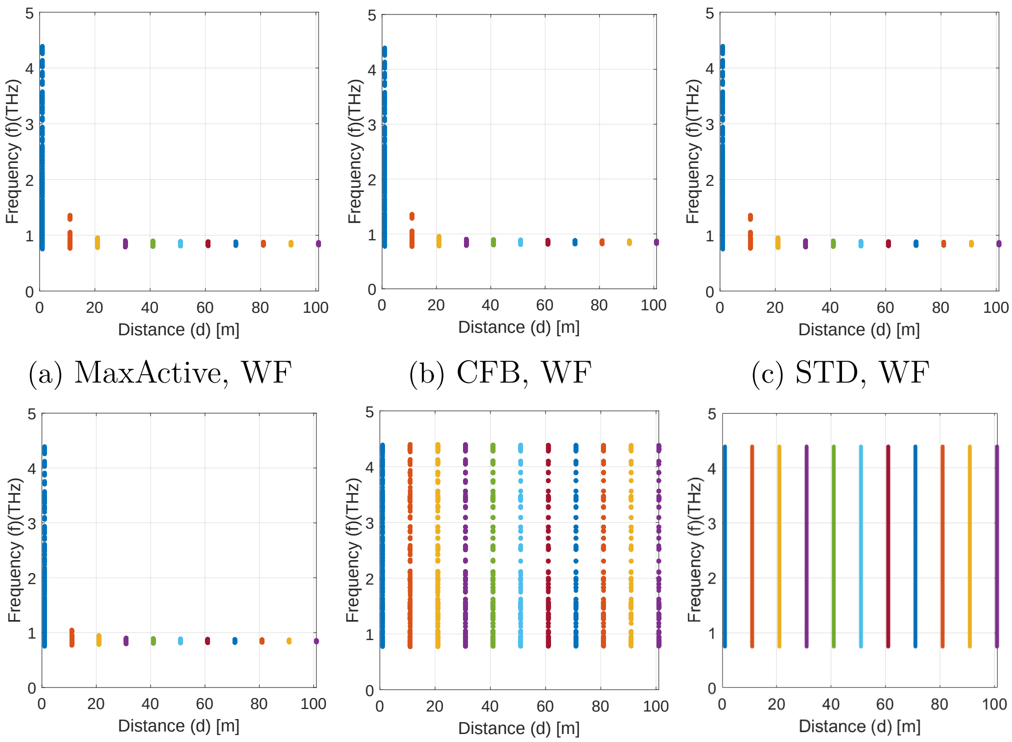

(a) MaxActive, WF (b) CFB, WF (c) STD, WF

(d) MaxActive, EP (e) CFB, EP (f) STD, EP

Figure 5.7 Selected bands for the perfectly aligned scenario with 2D antenna model.

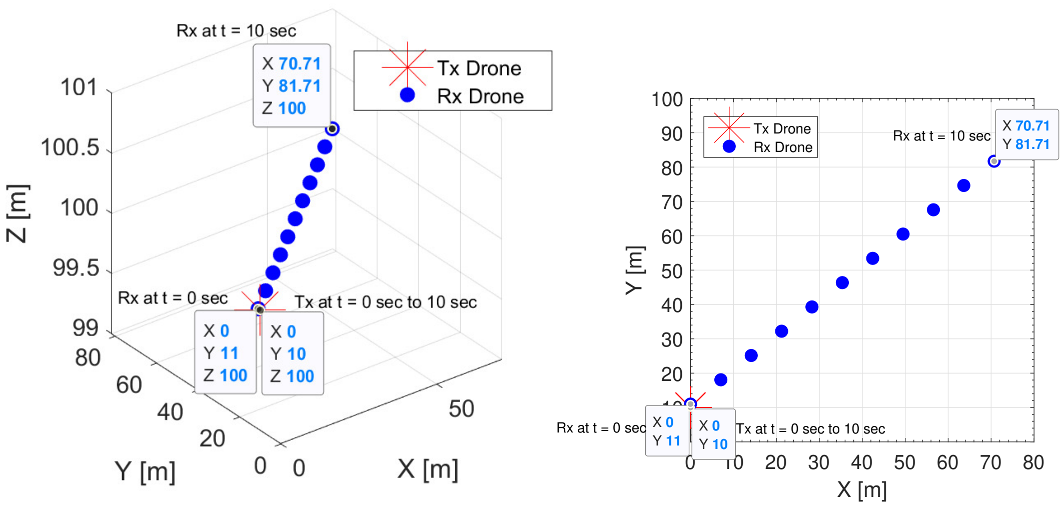

(a) Tx and Rx drones in 3D (b) Tx and Rx drones in 2D

Figure 5.8 Misaligned scenario via diagonal mobility: Tx drone is hovering, Rx is moving away diagonally from Tx.

For the scenario of misaligned via diagonal mobility without beamwidth adjustment, Fig. 5.9(a) shows the trend of the Tx, Rx beamwidths, azimuth and elevation boresights differences and the resulting total antenna gains. It can be seen that due to the diagonal motion of the Rx drone over the XY plane, the azimuth boresight difference, which was initially at 0 degrees at t = 0 sec, starts increasing at t = 1 sec due to the incurred misalignment of the Tx and Rx boresights. This causes the total antenna gain to drop from 52 dB (main lobe gain at t = 0) to -20 dB (side lobe level gain). Hence, there is a need to adjust the Tx-Rx beamwidth adaptively to compensate for the misalignment in the mobile Dr2Dr scenarios. With the beamwidth adjustment, Fig. 5.9(b) provides the trend of adjusting the Tx, Rx beamwidths with respect to the azimuth boresight misalignment. Both the Tx, Rx beamwidths start adaptation at $t = 1$ sec, when the azimuth boresight of the Tx, Rx antennas observe the misalignment. This in turn results the total antenna gain to be maintained within the main lobes, i.e., 14.14 dB, without switching the transmission over the slide lobe levels of -20 dB. This highlights the efficacy of employing the beamwidth adjustment in the mobility where the misalignment can cause substantial degradation in the antenna gains.

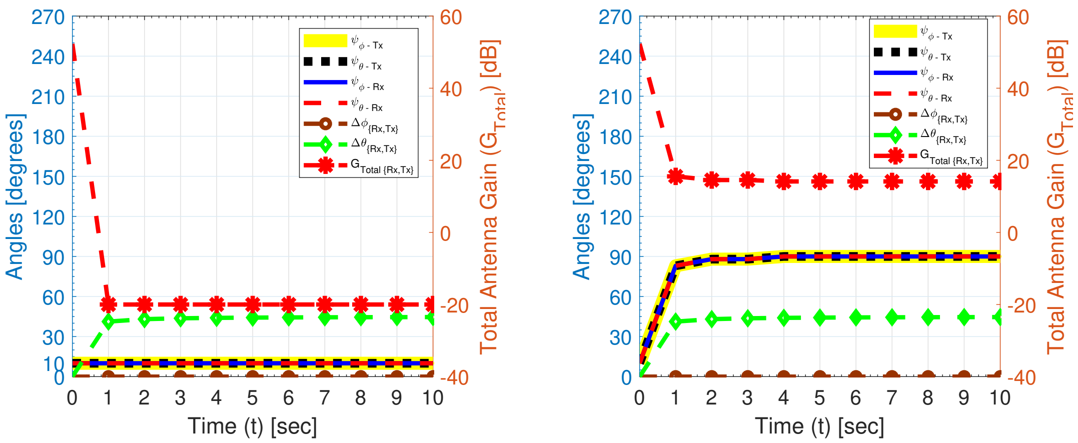

(a) Misaligned, without beamwidth adjustment

(b) Misaligned with beamwidth adjustment.

Figure 5.9 Trend of the Tx, Rx 3D beamwidths, Tx, Rx elevation and azimuth boresight differences, and the corresponding total antenna gains for the misaligned scenario via diagonal mobility.

For the misaligned scenario via diagonal mobility, Fig 5.10 and Fig. 5.11 show the selected bands without and with beamwidth adjustments, respectively, for the three considered band selection schemes with WF and EP for each. WF in all the three schemes depict similar bands as shown earlier in Fig 5.6, with the MaxActive with EP is approximating the WF counterpart. CFB with EP again depicts discontinuities across high absorption frequencies, whereas the STD with EP considers the entire band across 0.75-4.4 THz.

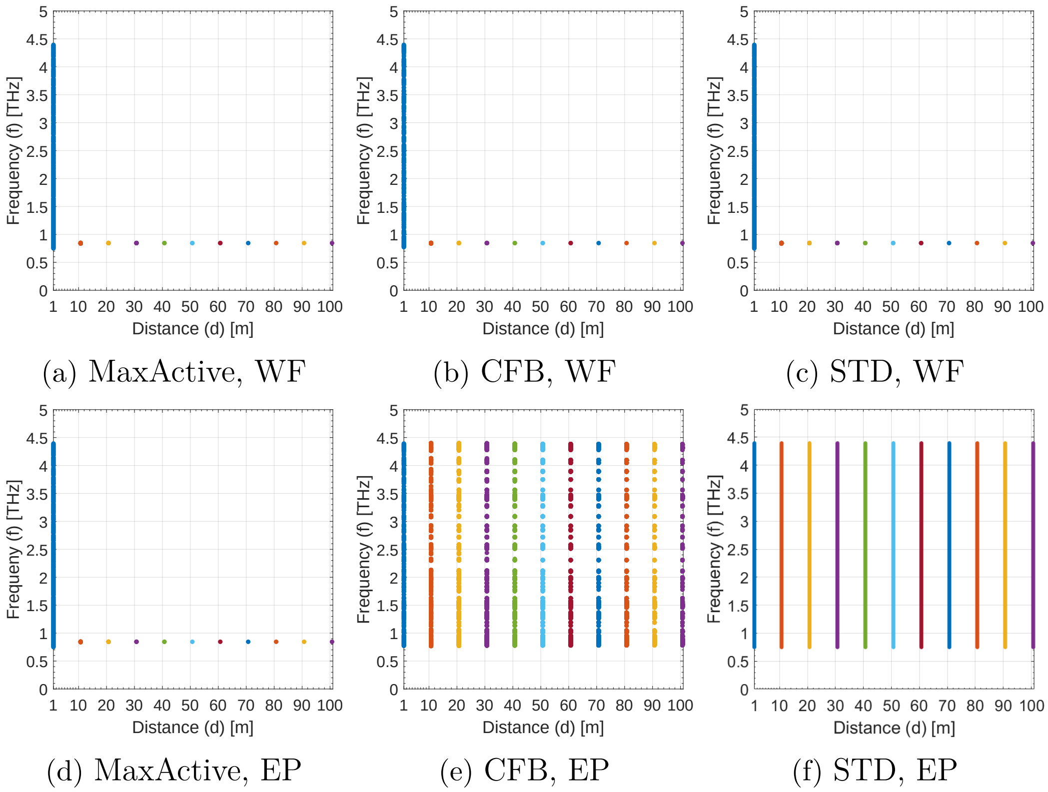

Figure 5.10 Selected bands for the misaligned scenario via diagonal mobility without beamwidth adjustment.

The effect of beam misalignment can be clearly observed in Fig. 5.12 by comparing capacity trend of the cases of perfectly aligned with 3D the symmetric antenna model and the misaligned scenario via the diagonal mobility with the 3D symmetric antenna model. For instance, with the perfect alignment at d = 100 m, capacity values of all of the three considered schemes with WF allocation stands at about 207 Gbps, which is 83.8 Mbps for the case of the misalignment via diagonal mobility with the beamwidth adjustments. Moreover, when the beam adjustment is not provisioned, the capacity further drops down to 32.6 kbps. Similar trend can be observed with the EP allocation for the three considered band allocation schemes. Since the 2D antenna model is only a slice of the actual 3D antenna model in the azimuth plane, which is also evident from the total antenna gains as shown earlier in Fig. 5.5, therefore, the capacity values obtained using the 2D antenna model are lower as compared to the capacity computed using the 3D symmetric antenna model.

Fig 5.13 provide the spectral efficiencies of the perfectly aligned scenario with both 3D symmetric antenna model and 2D antenna model, and misaligned scenario via diagonal mobility with 3D symmetric antenna model without and with beam ad-

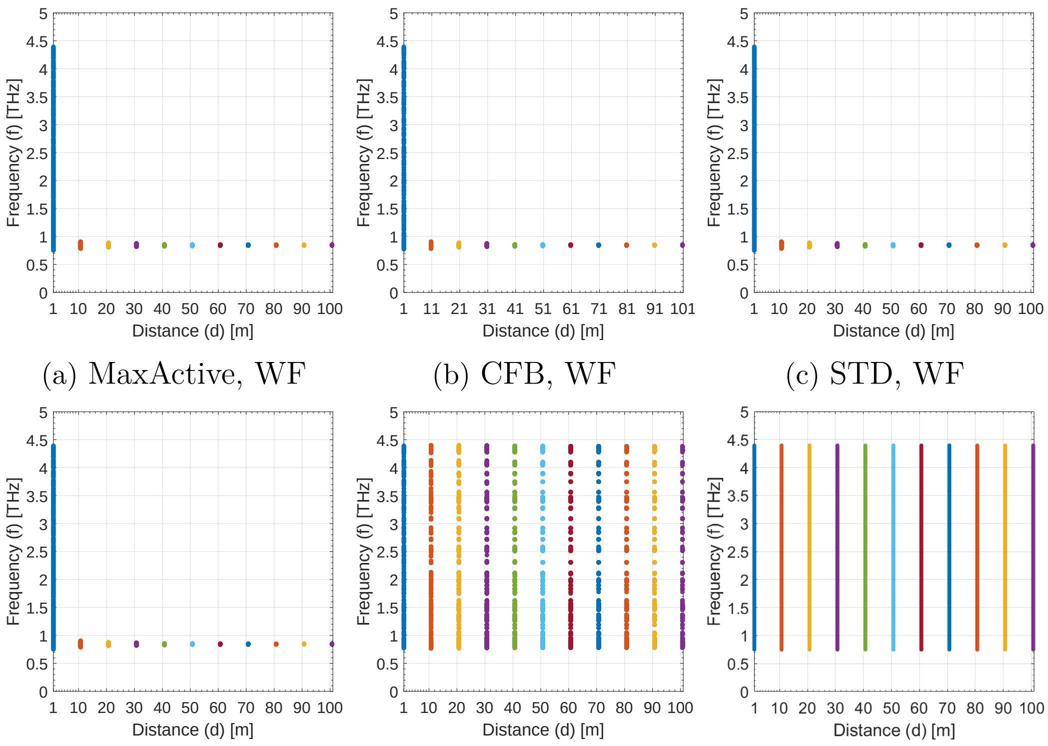

(a) MaxActive, WF (b) CFB, WF (c) STD, WF

(d) MaxActive, EP (e) CFB, EP (f) STD, EP

Figure 5.11 Selected bands for the misaligned scenario via diagonal mobility with beamwidth adjustment.

justment. Evidently, the perfectly aligned (ideal) case promises the highest spectral efficiency values for each of the three band allocation schemes with WF and EP allocations, followed by the misaligned with beam adjustment and misaligned without beam adjustment. For instance, at d = 100 m, MaxActive with EP stands at 1.837 bits/sec/Hz, which drops by two orders of magnitude for the misaligned with beam adjustment case, which is further dropped by two orders of magnitude for the misaligned without beam adjustment case. Similar trends can be observed for the CFB and STD schemes with EP allocations. CFB with EP at d = 100 m for the aligned case is 0.119 bits/sec/Hz, which is dropped by 2 orders of magnitude for the misaligned with the beam adjustment case, which is further decreased by four orders of magnitude for the misaligned without beam adjustment case. Finally, STD with EP at d = 100 m, which is 0.004 bits/sec/Hz, is decreased by four orders of magnitude for the misaligned with beam adjustment case, which is further declined by three orders of magnitude for the case of misalignment without the beam adjustment case. With the 2D antenna model, the perfectly aligned scenario provides lower spectral efficiency values as compared to the 3D symmetric antenna model. Having shown that the 3D symmetric antenna model results are more realistic as compared to the 2D antenna model for the perfectly aligned scenario, in the subsequent scenarios, we consider only the 3D symmetric antenna model for the performance under mobility

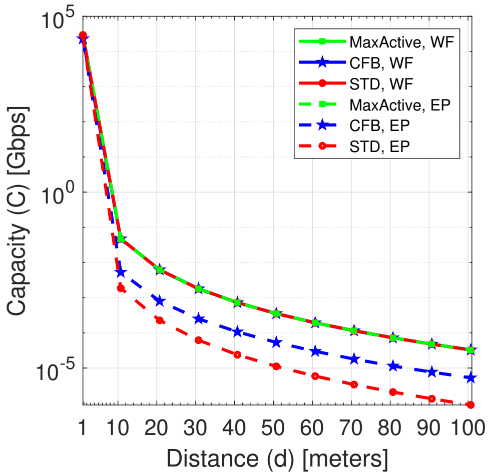

(a) Misaligned with 3D symmetric antenna model and without beamwidth adjustment

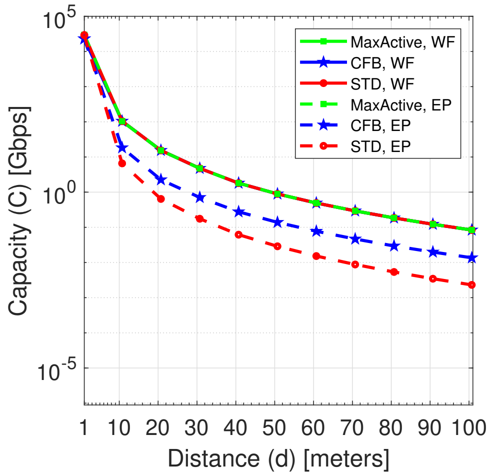

(b) Misaligned with 3D symmetric antenna model and with beamwidth adjustment

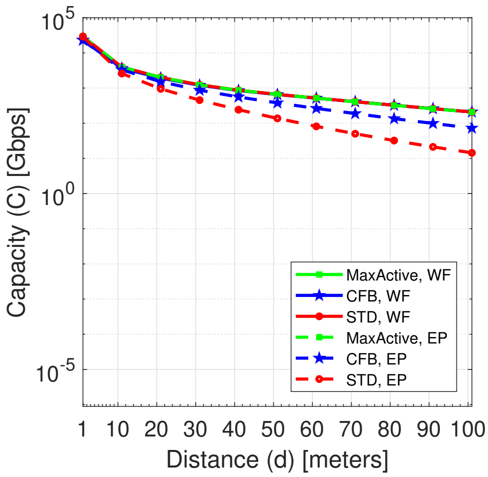

(c) Aligned, with 3D symmetric antenna model

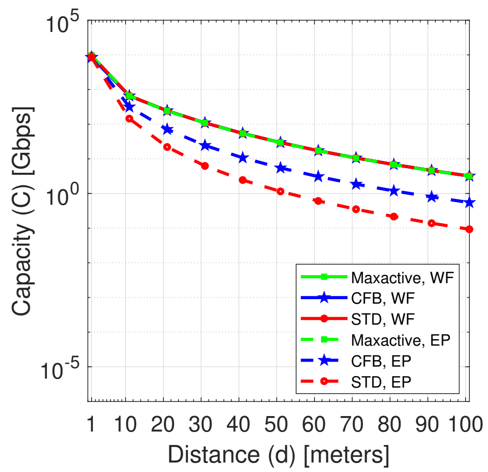

(d) Aligned, with 2D antenna model

Figure 5.12 Capacity comparison of the channel selection schemes with WF and EP allocations for the misaligned scenario via diagonal mobility and the perfectly aligned scenario with 3D symmetric antenna model and 2D antenna model.

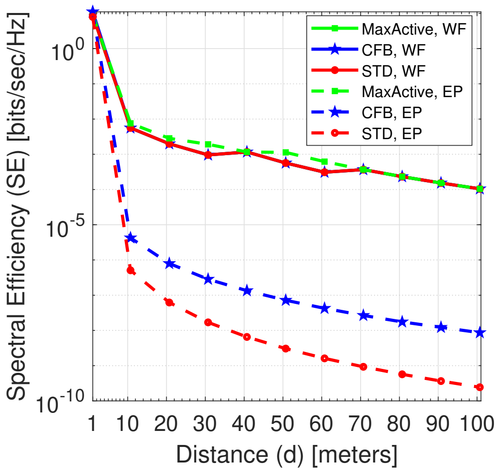

(a) Misaligned with 3D symmetric antenna model and without beamwidth adjustment

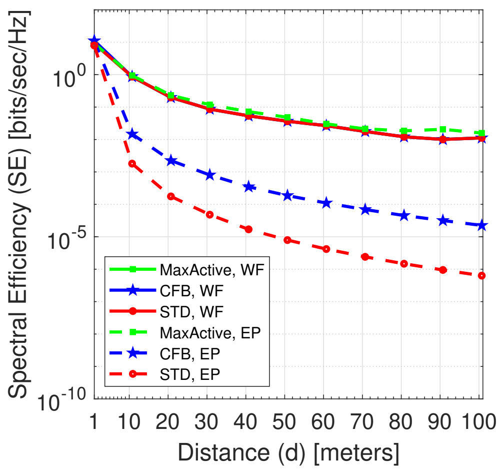

(b) Misaligned with 3D symmetric antenna model and with beamwidth adjustment

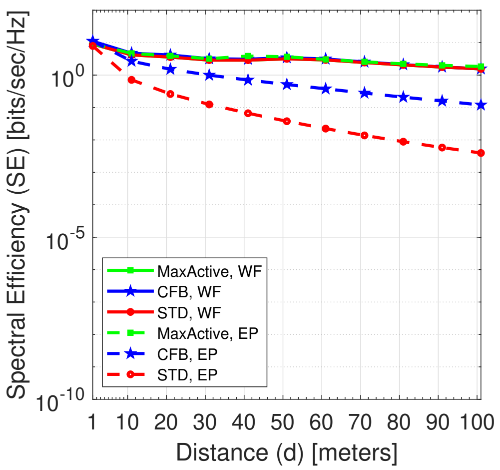

(c) Aligned, with 3D symmetric antenna model

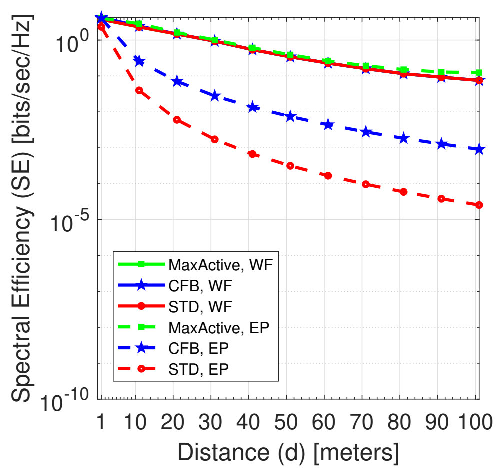

(d) Aligned, with 2D antenna model

Figure 5.13 Spectral efficiency comparison of the channel selection schemes with WF and EP allocations for the misaligned scenario via diagonal mobility and the perfectly aligned scenario with 3D symmetric antenna model and 2D antenna model.

analysis.

5.4.3 Scenario 3: Misaligned Scenario via Mobility Over Azimuth

As the third realistic THz band Dr2Dr communication scenario, we consider the Tx drone hovering at 100 m altitude, whereas the Rx drone is moving across the Tx drone in a semi-circular fashion over the azimuth (horizontal) plane while maintaining the Tx-Rx distance, $d = 20$ m, as shown in Fig. 5.14. At $t = 0$ sec, the boresights of both the Tx and Rx drones are aligned, while starting $t = 1$ sec and on wards, the Rx drone due to the semi-circular mobility starts getting misaligned from the Tx drone.

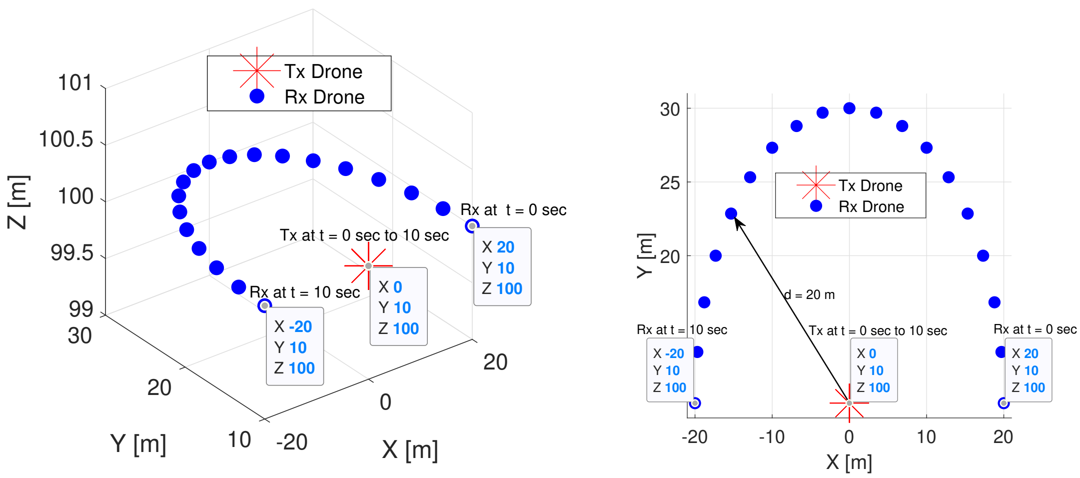

(a) Tx and Rx drones in 3D (b) Tx and Rx drones in 2D

Figure 5.14 Misaligned scenario via mobility over azimuth: Tx drone is hovering, while Rx drone is moving around Tx over the azimuth (horizontal) plane.

For the misaligned scenario via mobility over azimuth, Fig. 5.15 illustrate the trend of the elevation and the azimuth beamwidths of the Tx and Rx antennas, the differences of the boresight elevation and azimuth angles of the Tx and Rx antennas (all at left y-axis), and the total antenna gain (right y-axis) with respect to the elapsed time, t. It can be seen that due to the semi-circular motion of the Rx drone across the Tx drone, the boresight difference of the Tx and Rx azimuth angles is increased starting t = 1 sec, which in turn makes the Tx-Rx beamwidth adjustments so as to keep the THz-enabled Dr2Dr link within the main lobes. Consequently, with the increase in the beamwidths, the total antenna gain drops. This trend continues till $t = 18$ sec, when the Rx drone reaches directly on the opposite side of the Tx drone with respect to its initial position, corresponding to the azimuth boresight difference of 180°. At this instant, the beamwidth adjustment makes the beamwidths (elevation and azimuth) of both the Tx and Rx antennas equal to 360^0, i.e., the isotropic radiation pattern.

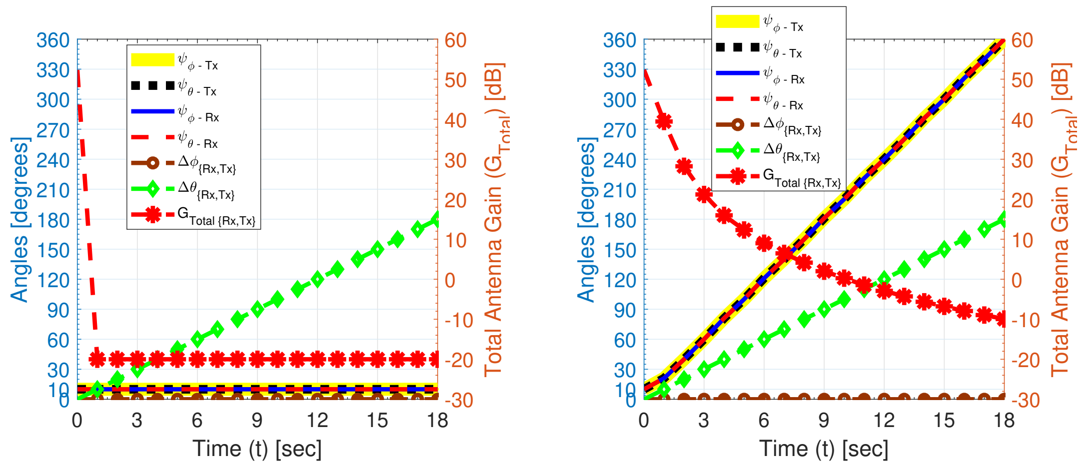

(a) Misaligned, without beamwidth adjustment

(b) Misaligned, with beamwidth adjustment

Figure 5.15 Trend of the Tx, Rx 3D beamwidths, Tx, Rx elevation and azimuth boresight differences, and the corresponding total antenna gains for the misaligned scenario via mobility over azimuth scenario.

Fig. 5.16 and Fig. 5.17 illustrate the trend of the selected bands for the considered scenario without and with beamwidth adjustments, respectively. When compared to Fig. 5.17, for the WF allocation in particular, it can be seen that there is a considerable decrease in the selected bands when no beamwidth adjustment is provided. This is due to the fact that the beamwidh adjustment ensures higher total antenna gains, while without adjusting the beamwidths causes the THz-enabled Dr2Dr link to shift the THz transmission to the slide lobe level of the Tx and Rx antennas. Therefore, adjusted antenna gains favors higher SNR values, leading to larger number of observed/feasible bands for communication with the WF allocation. MaxActive with EP allocation again provides similar bands as compared to the MaxActive with WF allocation, due to the nature of the capacity maximization of the MaxActive algorithm. CFB with EP shows the band discontinuities due to the elimination of the bands across the high THz absorption peaks. Finally, the STD with EP considers the entire band (0.75-4.4 THz) for the transmission, which is trivial.

Fig 5.18(a) provides the capacity of the azimuth scenario without beamwidth adjustment. It can be observed that as soon as the Rx drone starts the azimuth motion across Tx, the Tx and Rx boresights get misaligned, the transmission shifts towards the side spherical lobes of both the Tx and Rx drones. This causes the capacity to drop below to 10 Mbps levels. For instance, for MaxActive EP allocation without beamwidth adjustment, the capacity at $t = 1$ sec is less than 10 Mbps, while with

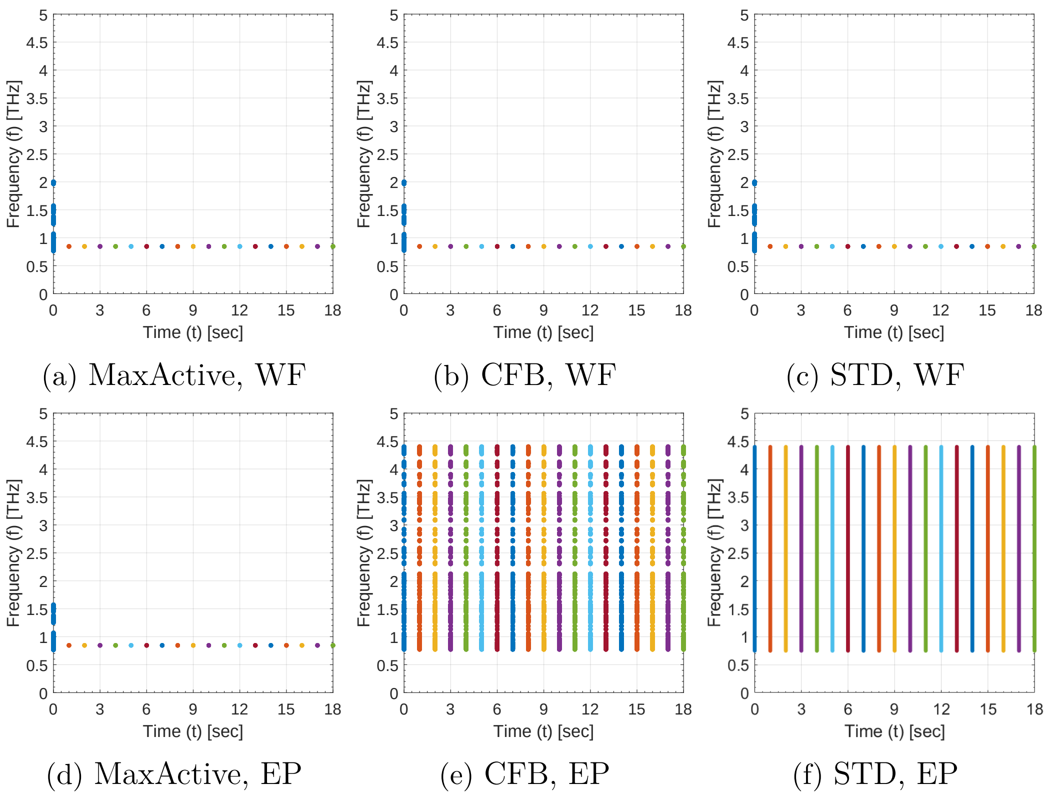

Figure 5.16 Selected bands for the misaligned scenario via azimuth mobility scenario without beamwidth adjustment.

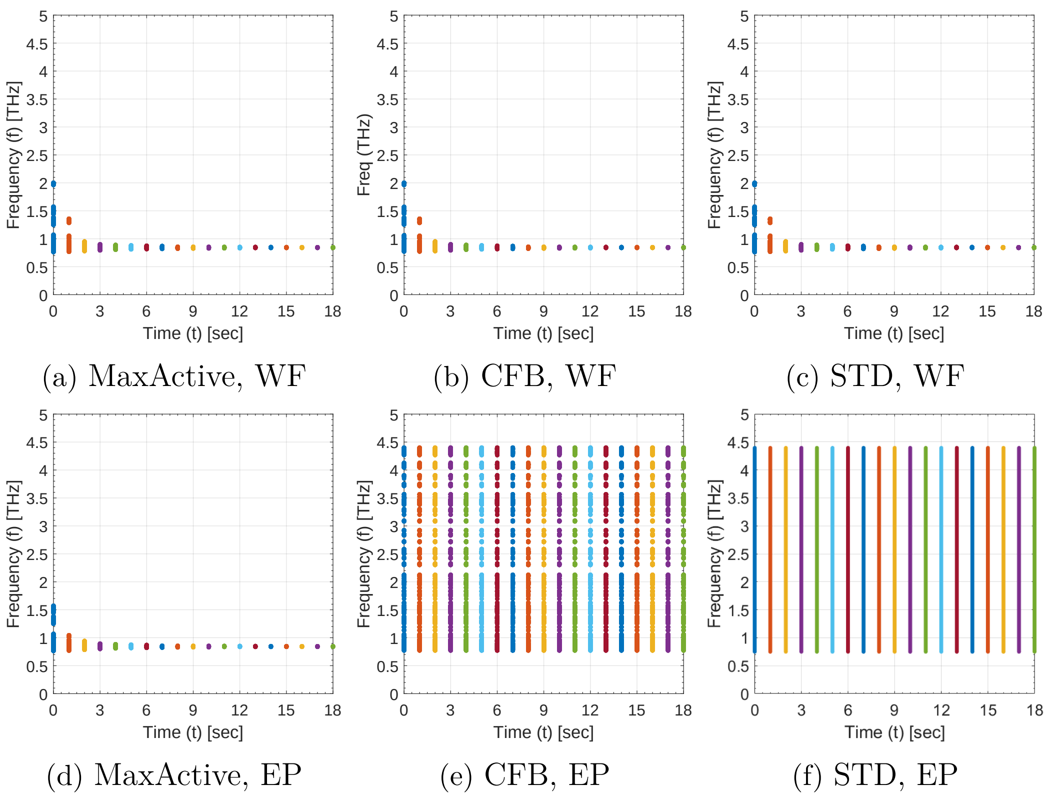

Figure 5.17 Selected bands for the misaligned scenario via azimuth mobility with beamwidth adjustment.

beamwidth adjustment, Fig 5.18(b) depicts that corresponding to the same time instant, the capacity is maintained at substantially higher levels as compared to the no beamwidth adjustment case. i.e., 714 Gbps.

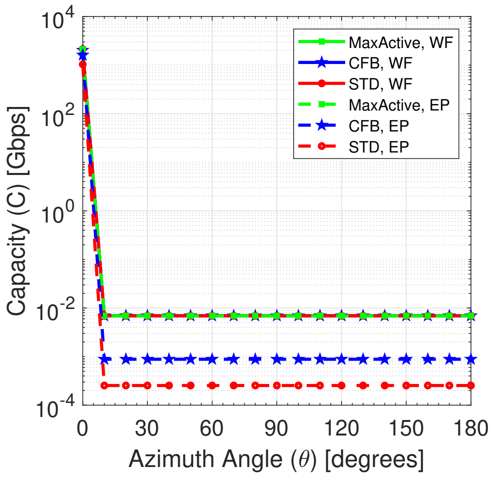

(a) Misaligned, without beamwidth adjustment

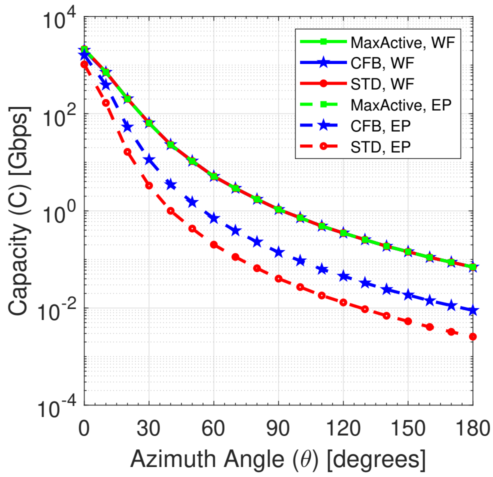

(b) Misaligned, with beamwidth adjustment

Figure 5.18 Capacity comparison of the channel selection schemes with WF and EP allocations for the misaligned scenario via azimuth mobility.

Fig. 5.19(a) illustrates the spectral efficiency for the azimuth scenario under no beamwidth adjustment, where the degradation impact of the azimuth misalignment on the spectral efficiency can be clearly seen. For example, for MaxActive with EP with beamwidth adjustment, as soon as the misalignment over azimuth takes place from $t = 0$ sec to 1 sec, the spectral efficiency drops from 4 bits/sec/Hz to 3 bits/sec/Hz. With beamwidth adjustment, i.e., Fig. 5.19(b), MaxActive with EP from $t = 0$ sec to 1 sec maintains the spectral efficiency values of 4 bits/sec/Hz to 0.003 bits/sec/Hz, i.e., by three order of magnitude.

5.4.4 Scenario 4: Misaligned Scenario via Mobility Over Elevation

For Rx mobility over the elevation/zenith plane, Fig. 5.20(a) and Fig. 5.20(b) illustrate the Tx and Rx drones in 3D and 2D depictions, respectively, where Tx is in hovering position while the Rx drone is moving around the Tx drone over the elevation plane and maintaining the inter-Tx and Rx drone distance, $d = 20$ m.

For the Rx drone motion over the elevation plane, Fig. 5.21(a) and Fig. 5.21(b) illustrates the trend antenna beamwidths, elevation and azimuth boresight angle differences of the Tx and Rx drone antennas, and the corresponding total antenna gains without and with beamwidth adjustment, respectively. For the beamwidth

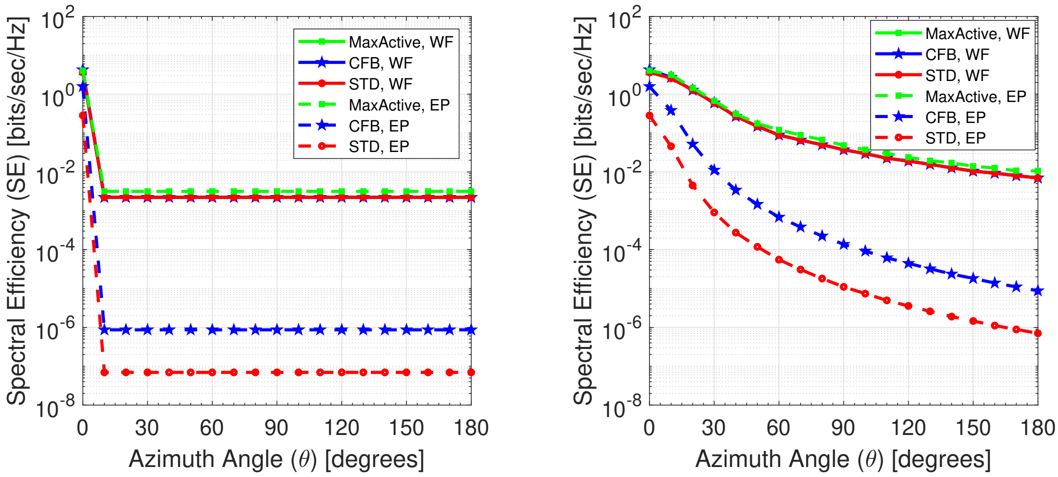

(a) Misaligned, without beamwidth adjustment

(b) Misaligned, with beamwidth adjustment

Figure 5.19 Spectral efficiency comparison of the channel selection schemes with WF and EP allocations for the misaligned scenario via azimuth mobility.

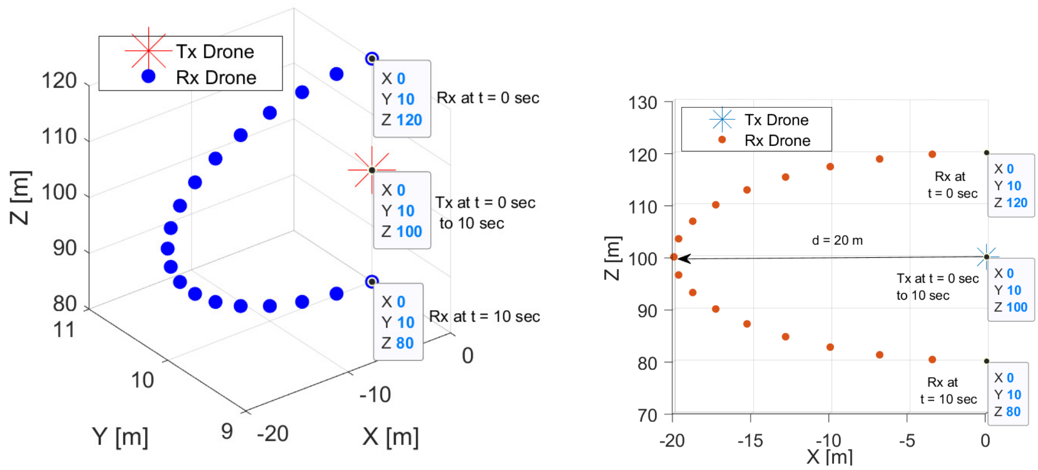

(a) Tx and Rx drones in 3D

(b) Tx and Rx drones in 2D

Figure 5.20 Misaligned scenario via mobility over elevation: Tx is hovering while Rx is moving around Tx over the vertical plane (elevation).

adjustment case, it can be observed that due to the Rx motion over the elevation/zenith plane, the elevation angle difference of the Tx and Tx antenna boresight angles starts increasing at $t = 1$ sec, which in turn leads to the increase in the beamwidths, consequently decreasing the total antenna gains. This trend continues as the Rx drone moves semi-circularly over the elevation plane across the Tx drone, till it reaches directly below the Tx drone at $t = 18$ sec, where the elevation boresight difference reaches 180°, making the adjusted beamwidths to be at 360°, where the corresponding total antenna gains reaches near -10 dB value. This gain is still above the total antenna gain side lobe level of -20 dB, as shown for the no beamwidth adjustment case in Fig. 5.21(a).

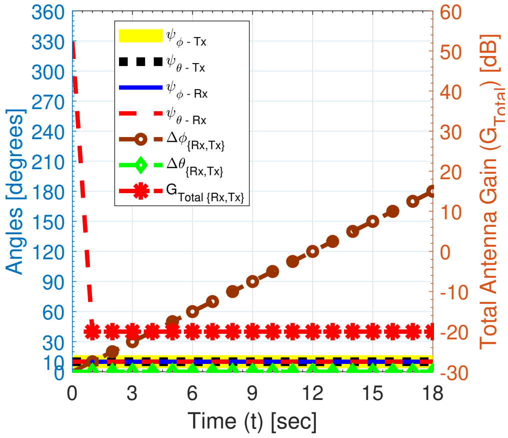

(a) Misaligned, without beamwidth adjustment

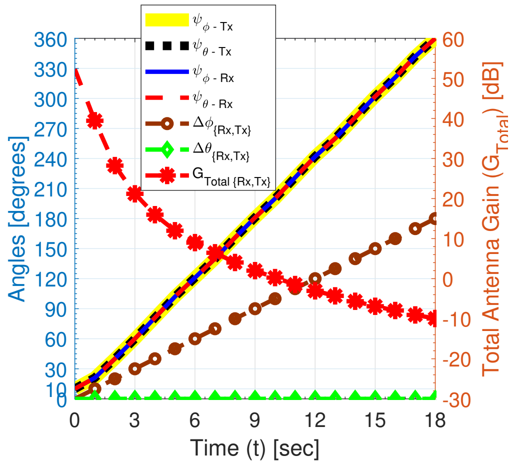

(b) Misaligned, with beamwidth adjustment

Figure 5.21 Trend of the Tx, Rx 3D beamwidths, Tx, Rx elevation and azimuth boresight differences, and the corresponding total antenna gains for the misaligned scenario via mobility over elevation.

Fig. 5.22 provides the trend of selected bands without beamwidth adjustment for the elevation scenario. Similar to the case of the azimuth scenario, all the three channel selection schemes with WF shows a considerable decrement in the bands as compared to the selected bands for the elevation scenario with beamwidth adjustment, due to the adjusted main lobes, hence promising larger antenna gains. Additionally, for the EP allocation, MaxActive depicts similar values as that of MaxActive with WF, while CFB and STD with EP allocation provides similar trends as compared to the earlier mobility scenarios at $d = 20$ m.

Fig. 5.23 provides the trend of the selected bands for the three considered channel selection schemes, each with WF and EP allocations. Similar to the earlier scenarios of the Rx motion over azimuth around Tx, Rx moving diagonally away from Tx, and the perfectly aligned case, WF allocation for each MaxActive, CFB, and STD provide similar bands at $d = 20$ m, whereas the MaxActive with EP again well approximates the selected bands of the MaxActive with WF allocation. Finally, the CFB EP provides discontinuous bands, due to the clipping of the bands across the high THz absorption peaks, and STD with EP considers the entire band for the transmission, as also seen in the earlier mobility scenarios.

For comparing the capacity with and without beamwidth adjustment, Fig. 5.24 provides the capacity with respect to the elevation/zenith angle. Clearly, the beamwidth adjustment maintains the capacity values considerably. It can be observed that the beamwidth adjustment plays a vital role in maintaining higher capacity values as

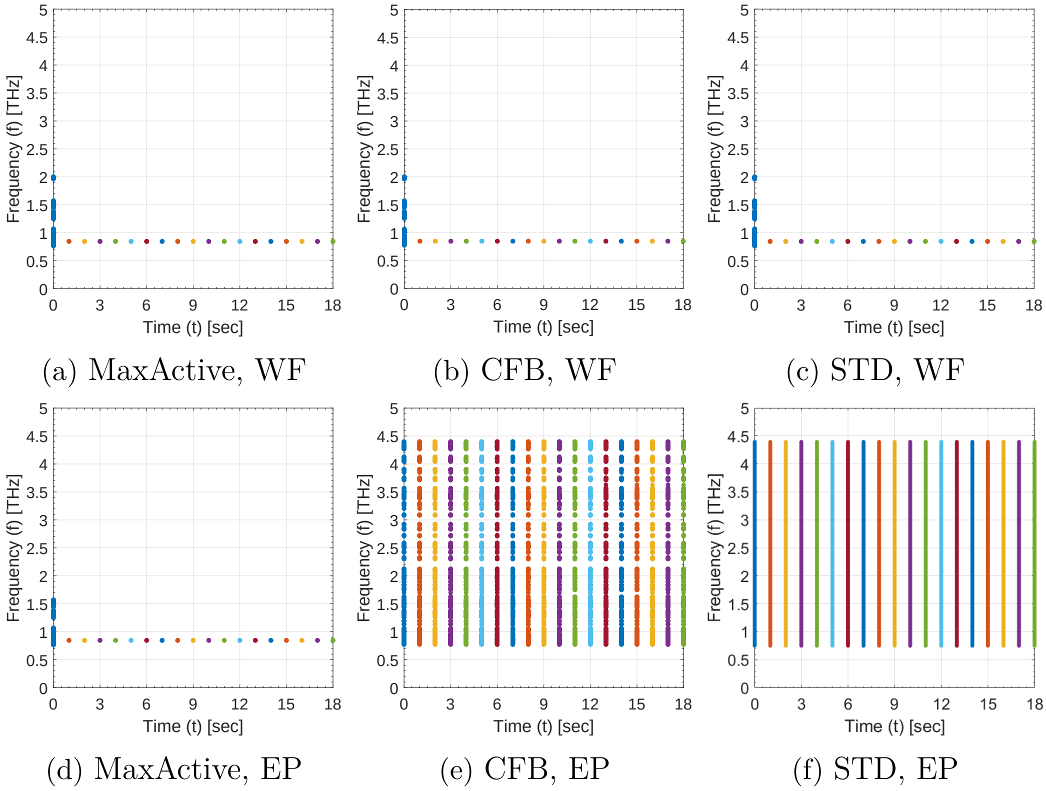

(a) MaxActive, WF (b) CFB, WF (c) STD, WF

(d) MaxActive, EP (e) CFB, EP (f) STD, EP

Figure 5.22 Selected bands for the misaligned scenario via elevation mobility without beamwidth adjustment

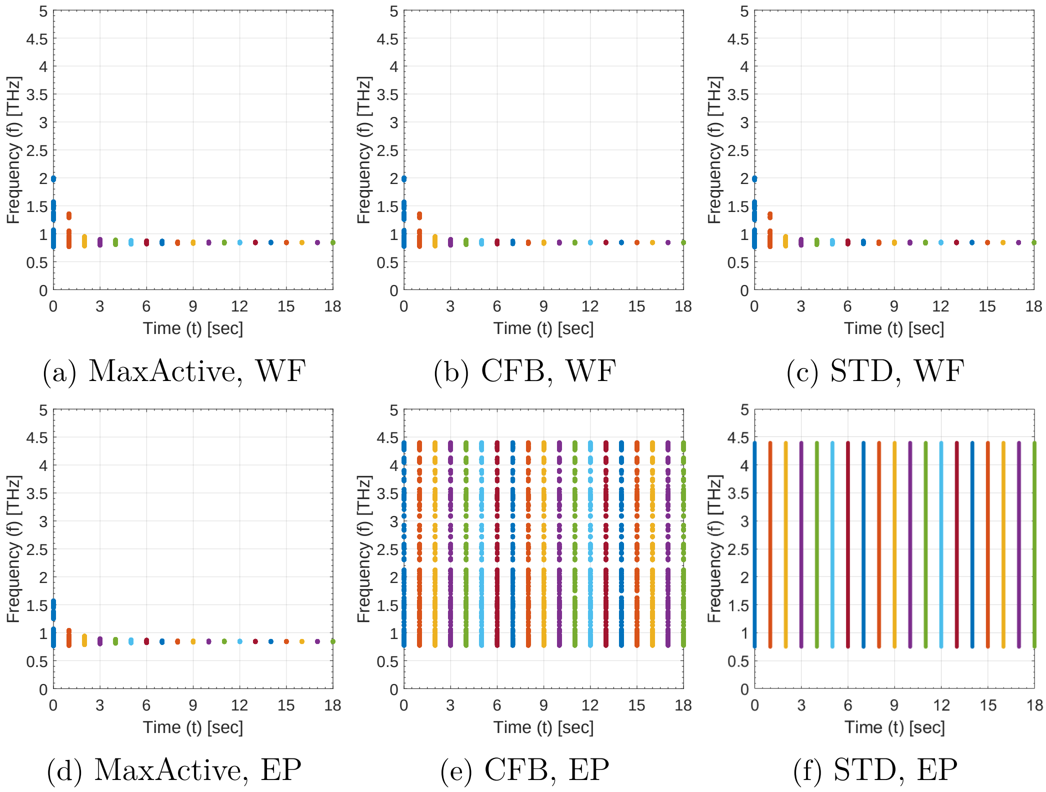

(a) MaxActive, WF (b) CFB, WF (c) STD, WF

(d) MaxActive, EP (e) CFB, EP (f) STD, EP

Figure 5.23 Selected bands for the misaligned scenario via mobility over elevation with beamwidth adjustment.

compared to the no beamwidth adjustment case, where the transmission is sustained in the side spherical lobes of the Tx and Rx drones. For instance, even at 90° elevation angle, the capacity values of MaxActive, EP offers capacity of 1 Gbps for the misaligned with beamwidth adjustment case, whereas for the no beamwidth adjustment case, it stands at 10 Mbps, i.e., a capacity degradation of two orders of the magnitude.

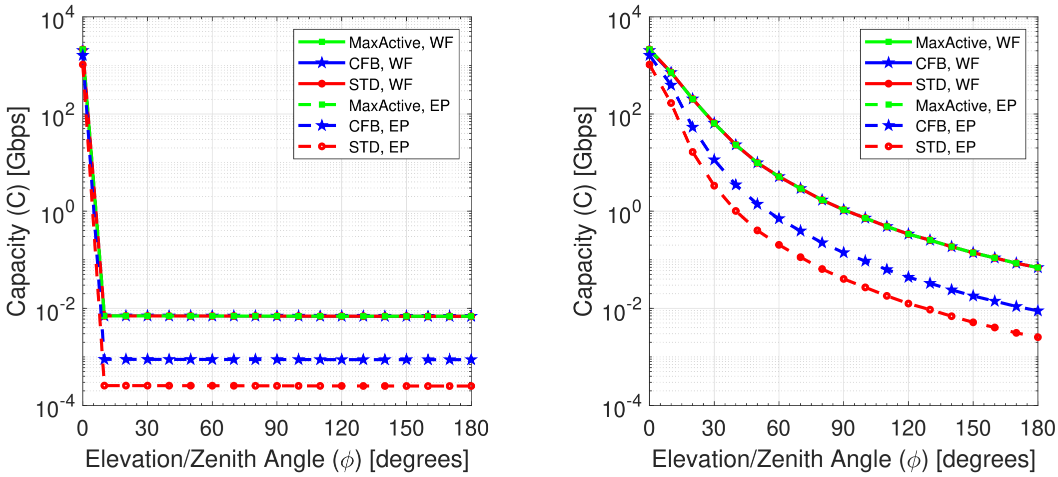

(a) Misaligned, without beamwidth adjustment

(b) Misaligned, with beamwidth adjustment

Figure 5.24 Capacity comparison of the channel selection schemes with WF and EP allocations for the misaligned scenario via mobility over elevation.

For evaluating the spectral efficiency of the three considered channel selection schemes, Fig. 5.25(a) and Fig. 5.25(b) depict that spectral efficiency for the elevation scenario with respect to the elevation angle without and with beamwidth adjustment, respectively. MaxActive with EP offers the highest spectral efficiency values over the entire considered elevation angle range, for both the cases without and with beamwidth adjustments.

Having presented four realistic Dr2Dr mobility scenarios, it is concluded that the beamwidth misalignment caused by the drone mobility highly affects the performance of THz-enabled Dr2Dr links. Provisioning the beamwidth adjustment promises higher capacity and spectral efficiency values, which is a trade-off between the perfectly aligned (ideal) mobility and the misaligned scenario without beamwidth adjustments. Moreover, on comparing the perfectly aligned scenario and the worst case scenario, i.e., motion over azimuth/elevation without and with beamwidth adjustments at $d = 20$ m, the capacity values are degraded by 6 and 5 orders of the magnitudes, respectively.

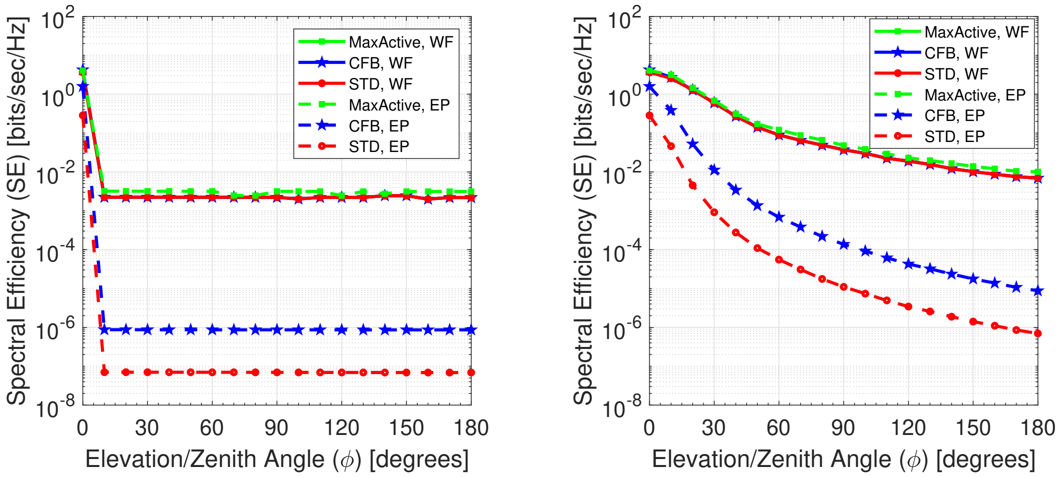

(a) Misaligned, without beamwidth adjustment

(b) Misaligned, with beamwidth adjustment

Figure 5.25 Spectral efficiency comparison of the channel selection schemes with WF and EP allocations for the misaligned scenario via mobility over elevation.

5.4.5 Scenario 5: Misaligned Scenario via Real Mobility Traces

As a special mobility case, we consider real drone mobility traces for THz-enabled Dr2Dr links [49]. Fig. 5.26(a) shows the mobility of Tx and Rx drones with respect to the real drone traces. Initially, at $t = 0$ sec, both Tx and Rx drones are 20 m apart, as depicted in Fig. 5.26(b). Starting $t = 1$ sec, the inter Tx-Rx distance starts varying due to the random mobility from the real traces. This distance keeps increasing up to $t = 3$ sec, when the Tx, Rx drone separation starts decreasing. It is to be noted here that although the drones can come closer to each other due to real traces, however, the initially-aligned Tx and Rx boresights can remain misaligned due to the orientation of the drones.

As the drones move randomly in both elevation and azimuth planes in the real mobility traces scenario, we consider 3D sectored antenna model with asymmetric Tx, Rx beamwidths, so that the beamwidth adjustment can ensure the THz link is maintained in the main lobes, while maintaining highest possible total antenna gains. Fig. 5.27(a) provides the trend of the 3D beamwidths, boresight angle differences and the corresponding total antenna gains for the misaligned scenario via real mobility traces without beamwidth adjustment. It can be observed the as soon as $t = 1$ sec, the Tx, Rx boresights get misaligned due to the random mobility of the drones, causing the THz link to shift to the side lobe transmission, i.e., -20 dB total antenna gains. By provisioning the beamwidth adjustment as depicted in Fig. 5.27(b), due to the boresight misalignments, the 3D asymmetric beamwidths of both Tx and Rx

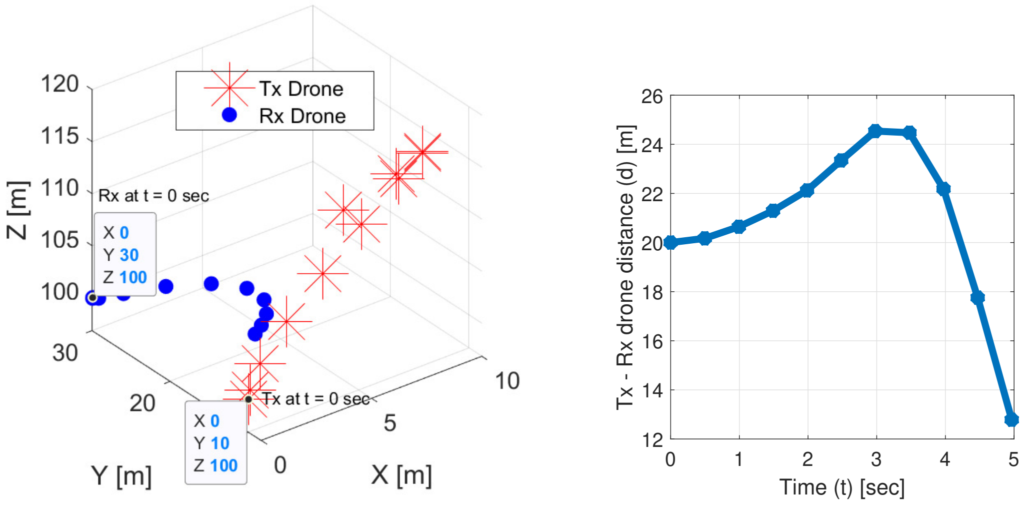

(a) Tx and Rx drones in 3D (b) Tx-Rx drone distance

Figure 5.26 Misaligned scenario via real mobility traces: Both Tx and Rx drones are moving with respect to real mobility traces scenario.

drones perform adjustments, promising the THz link over the main lobes, with higher antenna gains as compared to the no beamwidth adjustment case. For instance, even at t = 5 sec, the beamwidth adjustment offers a total antenna gain of 14.14 dB. Hence, under real mobility instances, the beamwidth adjustment plays a vital role in maintaining the THz links.

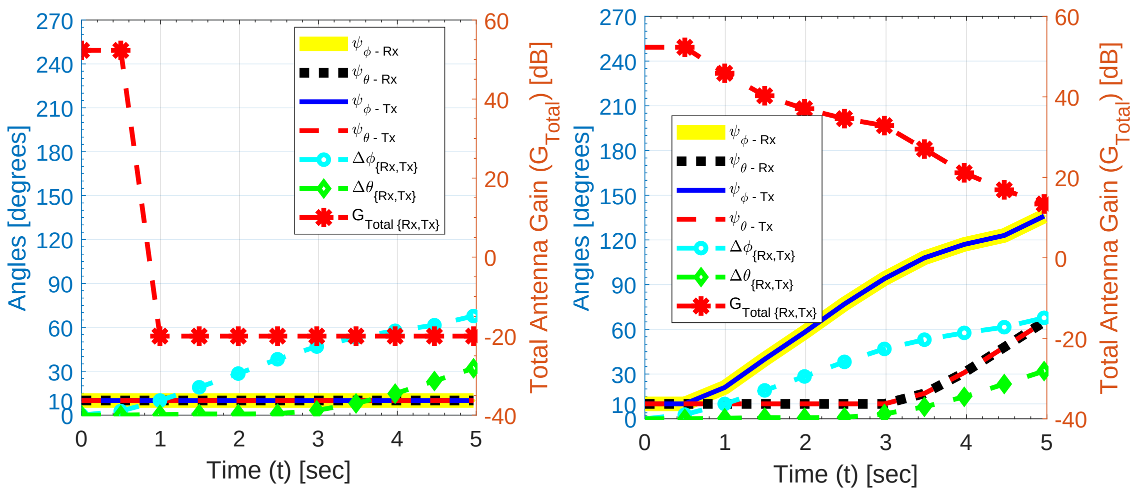

(a) Misaligned, without beamwidth adjustment (b) Misaligned, with beamwidth adjustment

Figure 5.27 Trend of the Tx, Rx 3D asymmetric beamwidths, Tx, Rx elevation and azimuth boresight differences, and the corresponding total antenna gains for the misaligned scenario via real mobility traces.

Fig. 5.28 and Fig. 5.29 provide the trend of the selected bands for the misaligned scenario via real mobility traces without and with beamwidth adjustment, respectively. As seen in earlier mobility scenarios 1-4, the beamwidth adjustment plays an important role in selecting larger number of THz channels in all three channel selection schemes as compared to the no beamwidth adjustment. MaxActive with EP still promises to be the best choice for the channel selection as compared to the CFB and STD schemes. The impact of real mobility on the selected channels is more dominant for the case of no beamwidth adjustment, and can be seen among all the cases with WF and MaxActive with EP. For example, with WF allocation for all the three schemes, the number selected channels decrease with elapsed time due to the incurred misalignment caused by the real mobility traces.

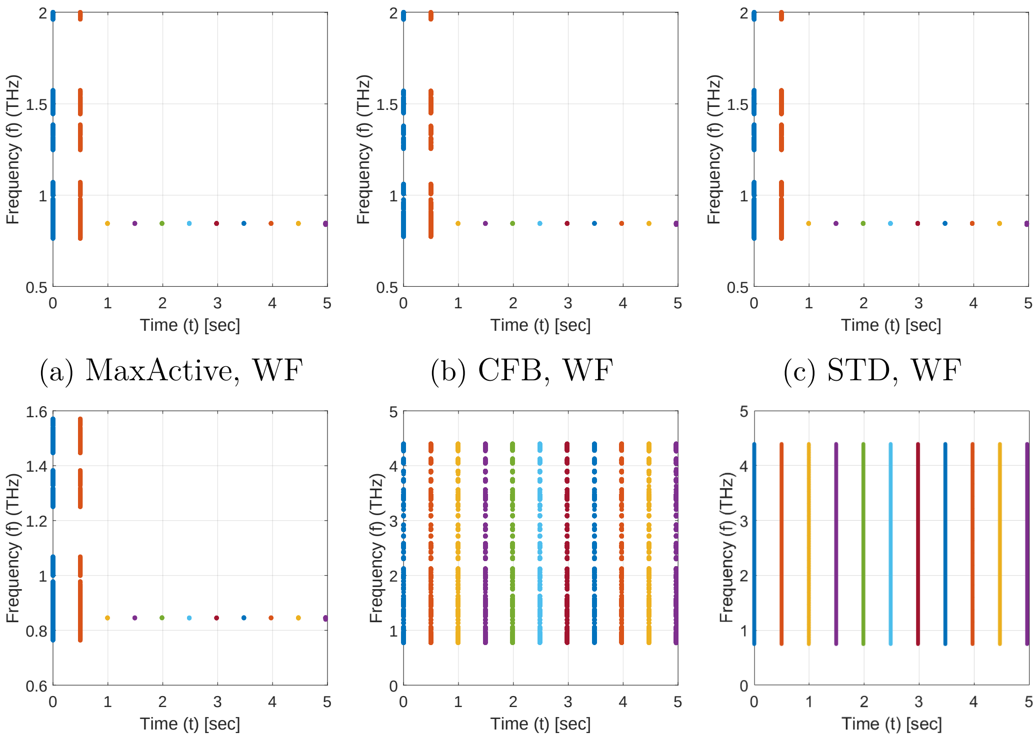

(a) MaxActive, WF (b) CFB, WF (c) STD, WF

(d) MaxActive, EP (e) CFB, EP (f) STD, EP

Figure 5.28 Selected bands for the misaligned scenario via real mobility traces without beamwidth adjustment.

Fig. 5.30(a) provides the capacity of the three channel selection schemes with both WF and EP allocations versus elapsed time for the mobility with real traces scenario. As soon as the Tx and Rx beams get misaligned at $t = 1$ sec, due to no beamwidth adjustment, the THz-enabled Dr2Dr link transmission shift towards the side lobe level, i.e., -20 dB, causing to degrade the capacity of greater than 1 Tbps to less than 10 Mbps. This shows the importance of adapting the Tx and Rx beamwidths to maintain high rate capacity values in real mobility instances. With beamwidth adjustment, Fig. 5.30(b) shows that substantially higher capacity values can be maintained as compared to the no beamwidth adjustment case. For instance, at $t = 5$ sec, MaxActive with EP offers about 70 Gbps, whereas with no beamwidth

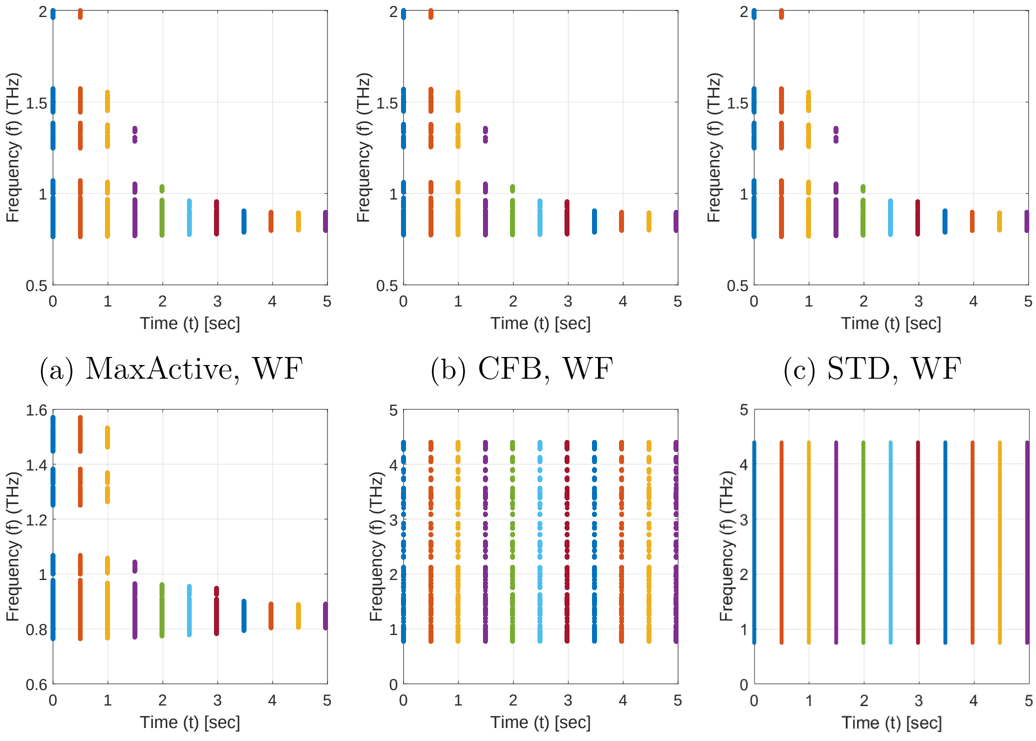

(a) MaxActive, WF (b) CFB, WF (c) STD, WF

(d) MaxActive, EP (e) CFB, EP (f) STD, EP

Figure 5.29 Selected bands for the misaligned scenario via real mobility traces with beamwidth adjustment.

adjustment (Fig. 5.30(a)), it stands at 180 Mbps.

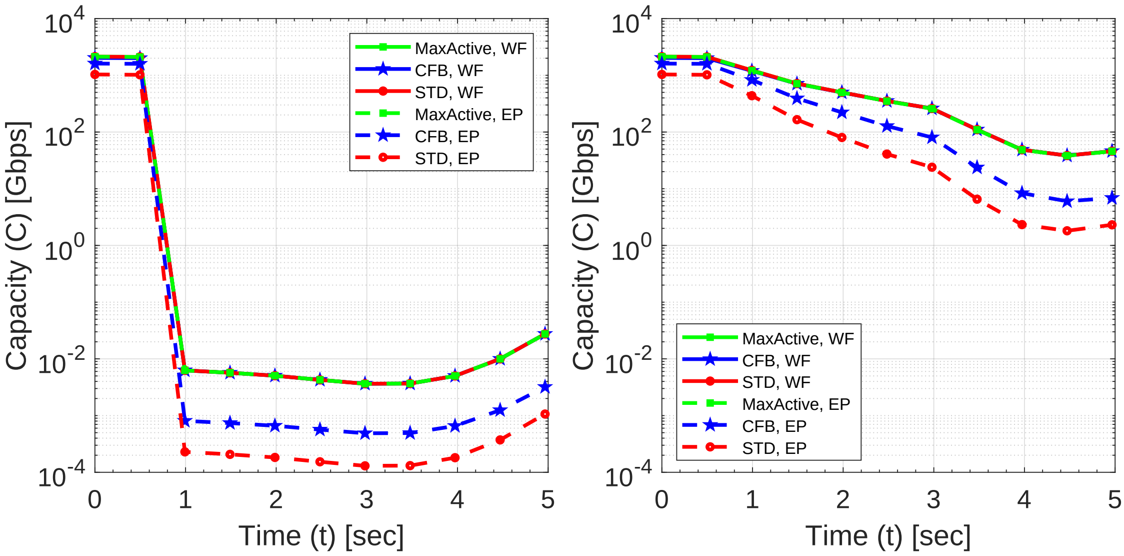

(a) Misaligned, without beamwidth adjustment (b) Misaligned, with beamwidth adjustment

Figure 5.30 Capacity comparison of the channel selection schemes with WF and EP allocations for the misaligned scenario via real mobility traces.

Fig. 5.31(a) illustrates the spectral efficiencies of MaxActive, CFB and STD channel selection schemes with WF and EP allocations for the real mobility trace scenario without bandwidth adjustment. Similar to the earlier mobility scenarios considered in this chapter, the MaxActive with EP offers highest spectral efficiency as compared to all other cases, with both WF and EP allocations. Same trend can be observed for the beamwidth adjustment, i.e., Fig. 5.31(b). However, the beamwidth adjustment ensures that the spectral efficiency values of all the three schemes remain at higher levels as compared to the no beamwidth adjustment provision. For instance, at $t = 3$ sec, MaxActive with EP and beamwidth adjustment offers greater than 1 bit/sec/Hz, while it stands at 0.05 bits/sec/Hz with no beamwidth adjustment provision, clearly depicting the efficacy of provisioning the beamwidth adjustment of THz-enabled Dr2Dr links in the real mobility instances.

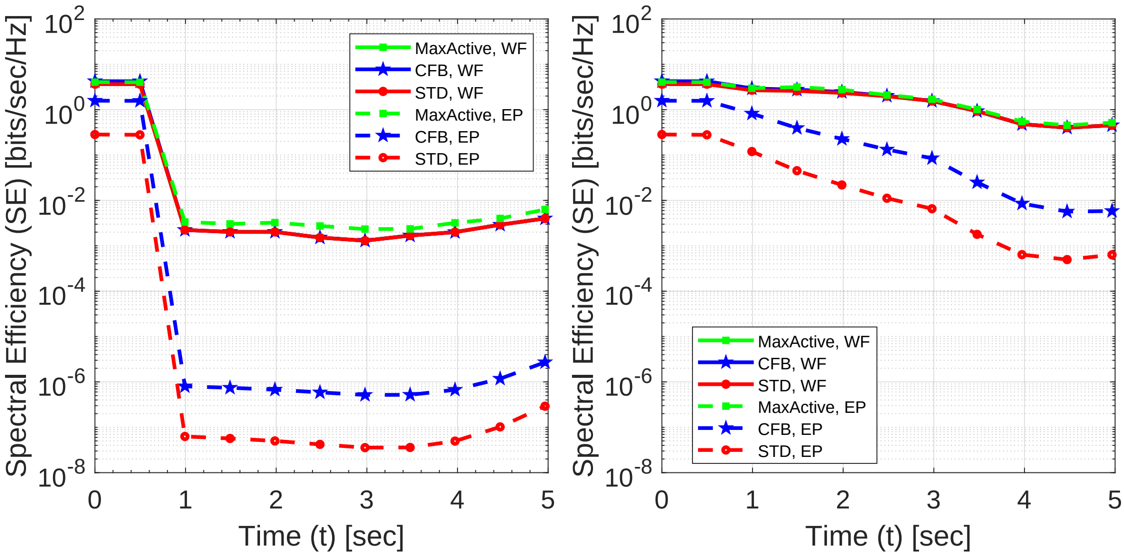

(a) Misaligned, without beamwidth adjustment

(b) Misaligned, with beamwidth adjustment

Figure 5.31 Spectral efficiency comparison of the channel selection schemes with WF and EP allocations for the misaligned scenario via real mobility traces.

Having considered the real mobility for THz-enabled Dr2Dr links, it can be concluded that the real motion of drones highly affect the Tx and Rx boresight misalignments, causing to degrade the capacity without beamwidth adjustment by up to 6 orders of the magnitude even with the WF allocations. However, with the beamwidth adjustment of 3D asymmetric beamwidths, WF-based capacity values of up to 45.7 Gbps are achievable, while the STD scheme with EP offers capacity values of up to 2.3 Gbps.

5.5 Performance Under Mobility With Real THz Antennas

In this section, MaxActive, CFB and STD channel schemes, each with WF and EP allocations are evaluated under three mobility scenarios by employing real THz antennas. We consider practical THz antennas over the frequency range of 0.75-1 THz [99], 1.24-1.4 THz [100], 1.7-2.1 THz [101], and 3.4-4.4 THz [102], as discussed in the following, in detail.

A wide-band THz H-plane dielectric high gain horn antenna based on silicon (Si) technology with an operating frequency ranging from 750 to 1000 GHz is designed by [99]. The measured gain of this antenna is larger than 8 dBi within the operating bandwidth with a peak gain of 11.7 dBi at 892 GHz. This antenna is a promising candidate for various THz systems due to its planar circuit integration and Silicon fabrication compatibility.

Another THz antenna for the frequency range of 1250 to 1400 GHz was developed by [100], using graphene for fixed-beam reflectarray antennas. Graphene's unique electronic band structure leads to a complex surface conductivity at THz frequencies, which allows the propagation of very slow plasmonic modes leading to a considerable reduction of the antenna size, without compromising the performance.

A reflectarray antenna based on square graphene patches is proposed by [101]. This antenna is optimized to demonstrate low cross polarization, low side-lobe level, good return loss, and excellent beam circularity over the 1700–2100 GHz frequency range, having a prototype of 31.7 dBi directivity.

A helix micro electro-mechanical systems (MEMS) based 3D on-chip antenna operating at 4 THz is realized on a silicon substrate [102]. This antenna is suitable for 2.8 THz to 4.4 THz operating frequency band. The simplicity, compactness, low cost and easy integration characteristics are the primary reasons for this antenna to be the designers choice for THz applications.

For depicting the true potential of the THz band (0.75-4.4 THz) for communication between drones, in the following, we employ the real THz antennas as considered in Fig.5.32 for the three mobility scenarios of perfectly aligned scenario, misaligned scenario via mobility over elevation, and misaligned scenario via real mobility traces.

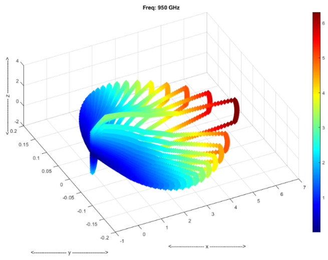

(a) Selected frequency = 950 GHz

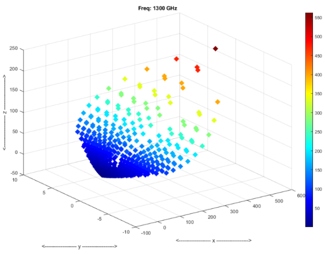

(b) Selected frequency = 1300 GHz

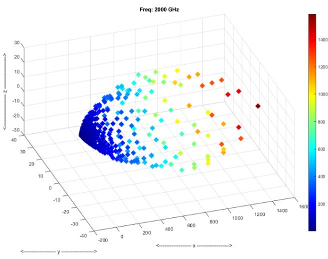

(c) Selected frequency = 2000 GHz

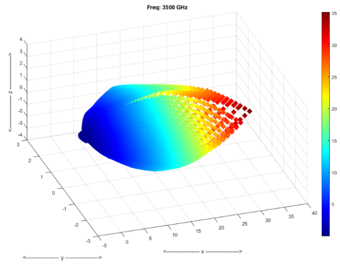

(d) Selected frequency = 3500 GHz

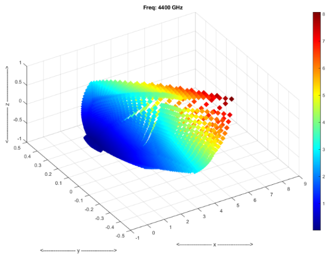

(e) Selected frequency = 4400 GHz

Figure 5.32 3D gain radiation pattern of real THz antennas over 0.75-4.4 THz with operating frequency ranges of: (a) 750-1000 GHz [99], (b) 1250-1400 GHz [100], (c) 1700-2100 GHz [101], (d) and (e) 3500-4400 GHz [102]. The practical antennas vary in the 3D gain radiation patterns at each selected frequency of operation and have fixed 3D gain radiation pattern i.e., no beamwidth adjustment.

5.5.1 Perfectly Aligned Scenario

As the first instance employing the real THz antennas, we consider the perfectly aligned scenario as considered earlier in Section 5.4.1.

Fig. 5.33 depicts the selected bands by the three channel selection schemes, each with WF and EP allocations for the perfectly aligned scenario with the real THz antennas. Clearly, WF allocations in all the considered schemes offer similar bands, showing the distance-dependent trend of the THz narrowbands, i.e., the number of selected bands reduce with the increase in the transmission range. With EP allocation, MaxActive selects less number of bands as compared to the CFB and STD schemes with EP allocations. This is because with the real THz antennas, THz Tx and Rx beamwidths are different for each frequency, hence the corresponding total antenna gains vary. Therefore, the SNR values drop to low levels, causing MaxActive with EP to select fewer number of bands as compared to the MaxActive with WF allocation.

For the perfectly aligned scenario with the real THz antennas, Fig. 5.34 depicts the capacity of the three channel selection schemes, each with WF and EP allocations,

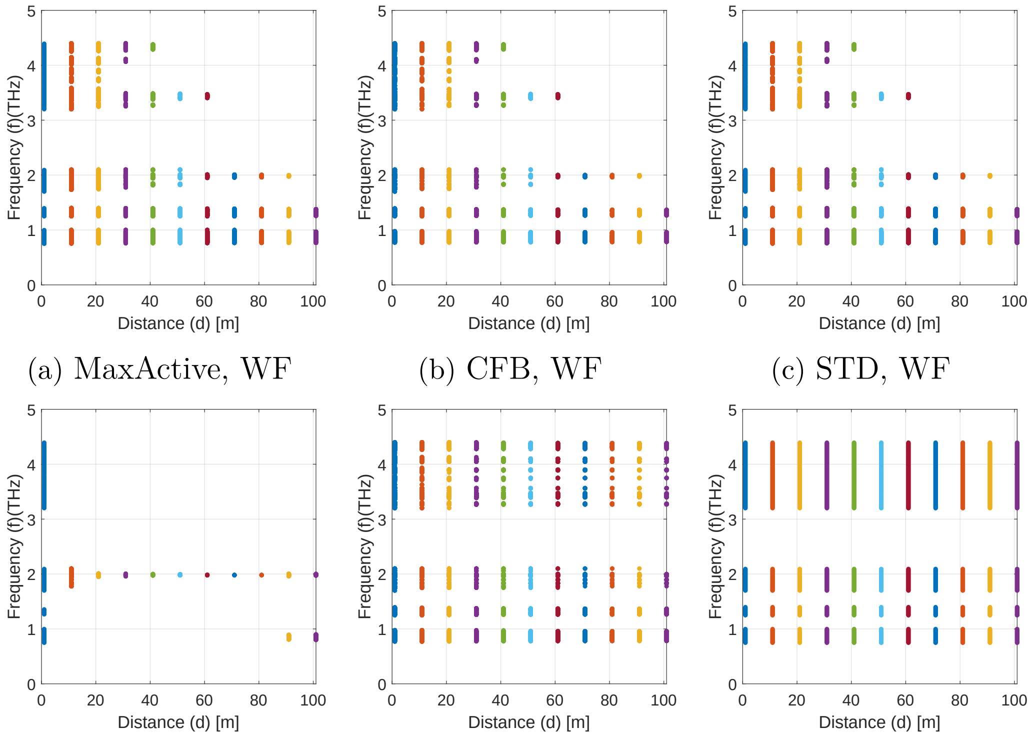

(a) MaxActive, WF (b) CFB, WF (c) STD, WF

(d) MaxActive, EP (e) CFB, EP (f) STD, EP

Figure 5.33 Selected bands for the perfectly aligned scenario using the real THz antennas.

as the function of range from 1 m to 101 m. All of the considered schemes with WF allocations provide similar capacity values over the entire range, ranging from 44 Tbps at 1 m to 2.90 Tbps at 101 m. Here, again, MaxActive with EP outperforms CFB and STD schemes with EP allocation over 1 m to 100 m, offering 15.48 Gbps at 50 m.

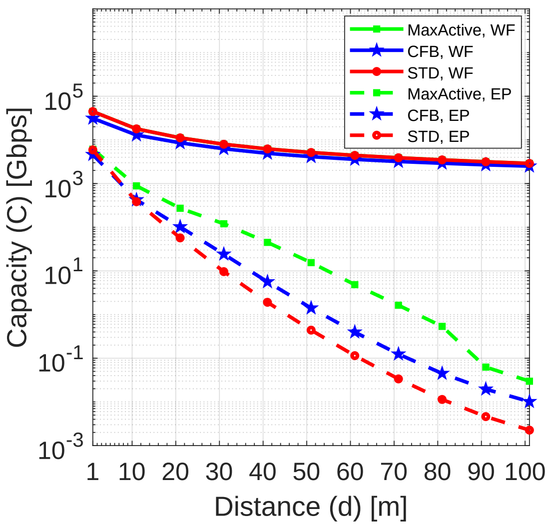

Figure 5.34 Capacity comparison of the channel selection schemes with WF and EP allocations for the perfectly aligned scenario with real THz antennas.

Fig. 5.35 provides the spectral efficiency of the three channel selection schemes, each with WF and EP allocation with respect to the transmission distance. It can be clearly observed that the MaxActive with EP marginally outperforms CFB and STD schemes with EP allocation, particularly over the ranges of 1 m up to 80 m, promising to be the most efficient channel selection scheme in terms of spectral efficiency. For instance, at d = 81 m, spectral efficiency of MaxActive with EP allocation is 5 orders of magnitude higher than the spectral efficiency of the STD scheme with EP allocation.

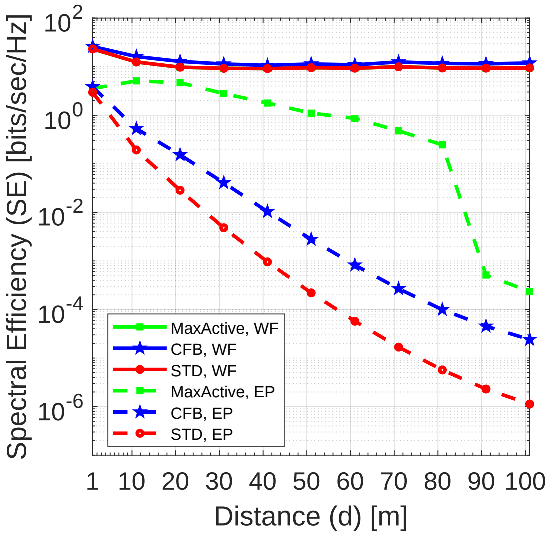

Figure 5.35 Spectral efficiency comparison of the channel selection schemes with WF and EP allocations for the perfectly aligned scenario with real THz antennas.

5.5.2 Misaligned Scenario via Mobility Over Elevation

We also consider the misaligned scenario via mobility over elevation as illustrated earlier in Section 5.4.4 by evaluating the THz-enabled Dr2Dr link performance at d = 20 m using the real THz antennas.

Fig. 5.37 provides the capacity with respective to the elevation angle ranging from 0° to 180°. It can be seen that the capacity values are similar for all the three channel selection schemes with WF allocation, having a maximum value of about 11 Tbps at 0°, where both Tx and Rx antennas are perfectly aligned, i.e., t = 0 sec. Moreover, with EP allocation, MaxActive still outperforms the CFB and STD schemes, offering a highest value of 303.4 Gbps at 0° elevation angle. Here, again, STD with EP offers the lowest capacity values over the entire elevation angle range. The results in Fig. 5.37 reveal that it is practically possible to achieve capacity values in the order of several 100s of Gbps up to 20 m range even with EP allocation using the state-of-the-art THz antennas.

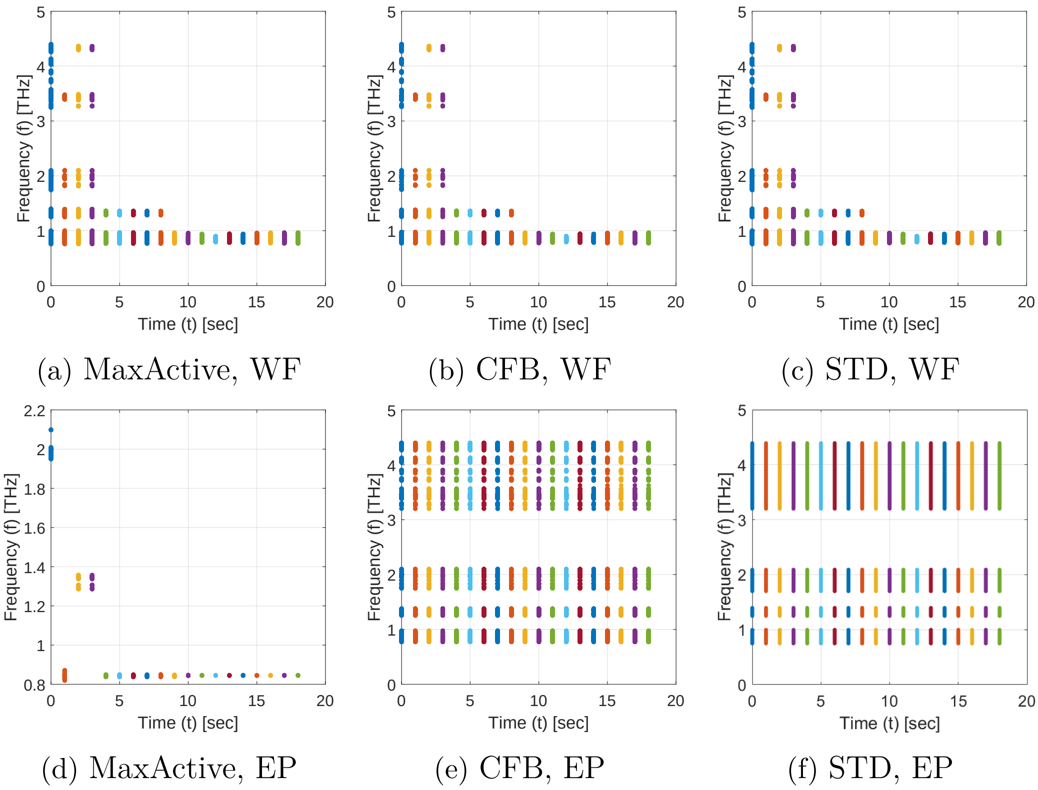

(a) MaxActive, WF (b) CFB, WF (c) STD, WF

(d) MaxActive, EP (e) CFB, EP (f) STD, EP

Figure 5.36 Selected bands for the misaligned scenario via mobility over elevation and real THz antennas.

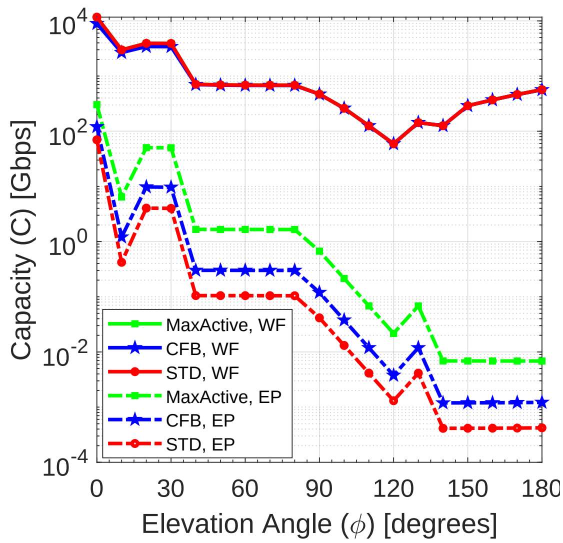

Figure 5.37 Capacity comparison of the channel selection schemes with WF and EP allocations for the misaligned scenario via mobility over elevation with real THz antennas.

Fig. 5.38 provides the spectral efficiency trend of the three channel selection schemes for the mobility over elevation scenario with real THz antennas. As seen in the earlier two mobility scenarios with real THz antennas, all the three channel selection schemes with WF allocation promise similar and highest spectral efficiency values as compared to the cases of EP allocation. With EP allocation, interestingly, it can be seen that the MaxActive offers much higher spectral efficiency values, i.e., up to 3 to 4 orders of magnitude higher as compared to the CFB and STD schemes over the entire elevation angle range. This shows that the MaxActive scheme with EP is highly favorable for practical THz systems in regards to the spectral efficiency.

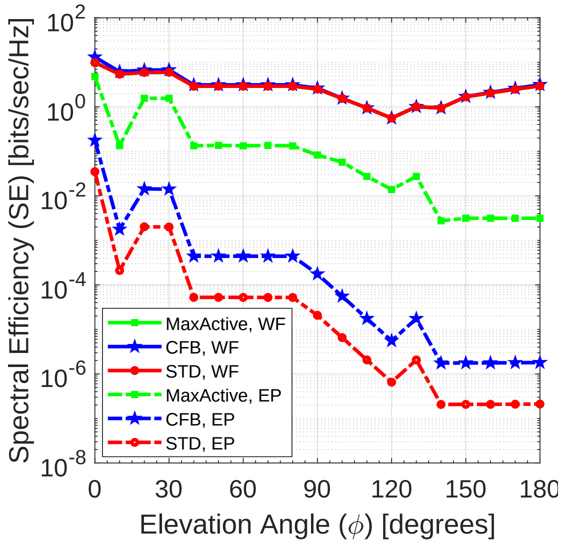

Figure 5.38 Spectral efficiency comparison of the channel selection schemes with WF and EP allocations for the misaligned scenario via mobility over elevation with real THz antennas.

5.5.3 Misaligned Scenario via Real Mobility Traces

As another practical scenario, we employ real THz antennas into the real mobility traces scenario, as presented earlier in Section 5.4.5. Initial Tx-Rx distance is set as 20 m with Tx at (0 m,10 m,100 m) and Rx at (0 m,30 m,100 m). Fig. 5.39 shows the selected bands by each of the three channel selection schemes with both WF and EP allocations. Clearly, with WF allocations, the three schemes select similar bands over the THz band 0.75-4.4 THz. However, with EP allocation, MaxActive selects fewer number of bands as compared to the earlier mobility scenarios due to variable antenna gains of the practical THz antennas with no beamwidth adjustment. Another reason is that the real THz antennas offer narrow THz beams across main lobes, with negligible side lobe gain levels. Hence, as soon as the Tx-Rx beams get misaligned, the total antenna gains drop, causing low SNR levels. For the CFB and STD schemes with EP allocations, the trend of selected bands are similar as observed in earlier mobility scenarios of this chapter.

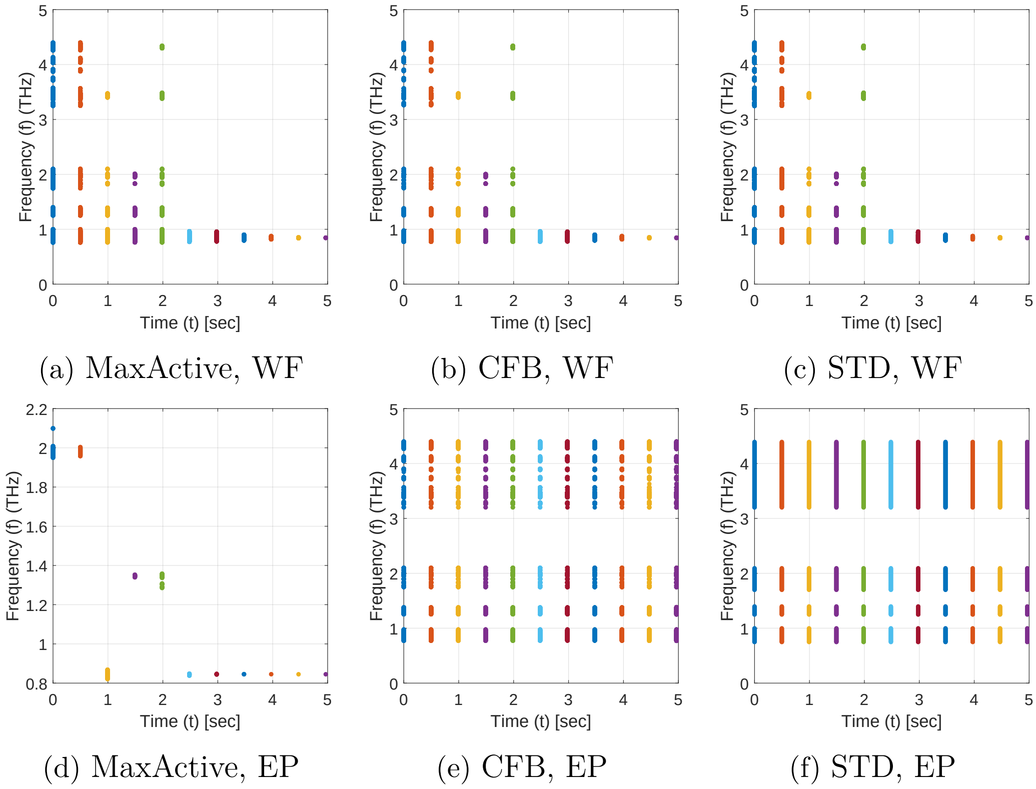

Figure 5.39 Selected bands for the misaligned scenario via real mobility traces and real THz antennas.

Fig. 5.40 provides the capacity comparison of the three channel selection schemes with both WF and EP allocations for the misaligned scenario via real mobility traces with real THz antennas. It can be seen that at $t = 0$ sec when both Tx and Rx are aligned, capacity values of about 11 Tbps are realizable using WF allocations with all the three schemes, while MaxActive with EP allocation offers about 298.8 Gbps, outperforming the CFB and STD schemes with EP allocation. Starting $t = 1$ sec, the real mobility of Tx and Rx drones causes the boresight misalignments, hence the overall capacity is reduced. This trend continues till $t = 5$ sec, where all the three schemes with WF offer capacity values of about 10 Mbps, whereas with EP, all the three schemes converge to the negligible capacity values, in the order of a few bps.

Fig. 5.41 provides the spectral efficiency with respect to time for the mobility with respect to the real traces and the practical THz antennas. Similar to case of the mobility over elevation scenario with real THz antennas in Fig. 5.37, all the three schemes with WF allocations offer highest spectral efficiency values, ranging from 13.09 bits/sec/Hz at $t = 0$ sec, up to about 300 mbits/sec/Hz at $t = 5$ sec. Moreover, again, MaxActive with EP clearly outperforms CFB and STD with EP allocations, by up to 5 order of magnitude. This shows the efficacy of employing the MaxActive

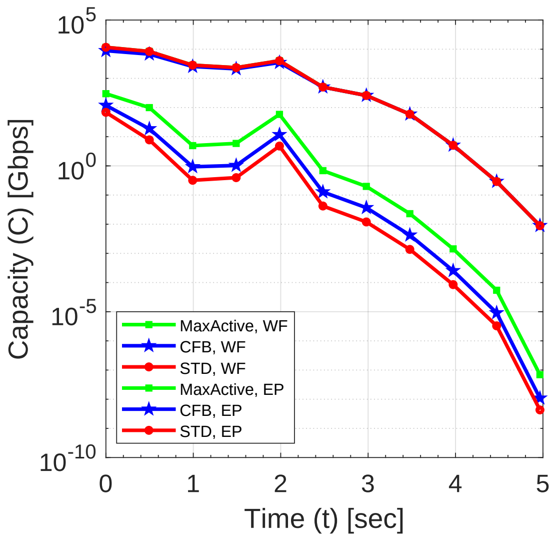

Figure 5.40 Capacity comparison of the channel selection schemes with WF and EP allocations for the misaligned scenario via real mobility traces and with real THz antennas.

scheme with EP allocation for real drone traces and real THz antennas, promising highly spectral efficient THz communication systems.

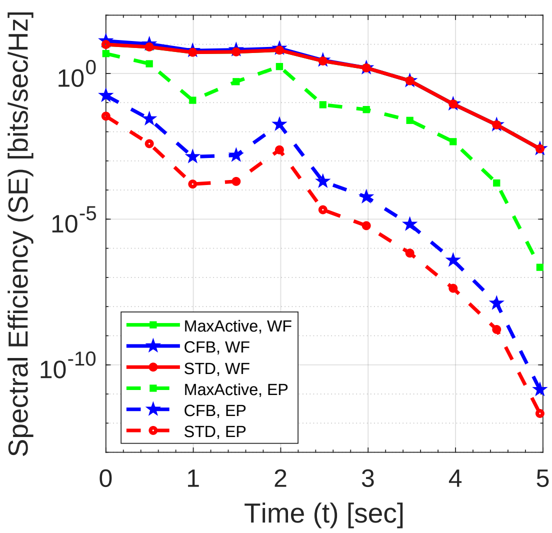

Figure 5.41 Spectral efficiency comparison of the channel selection schemes with WF and EP allocations for the misaligned scenario via real mobility traces and with real THz antennas.

For the perfectly aligned scenario, it is observed that the WF capacity and spectral efficiency results with the constant gain, 3D symmetric beamwidths without adjustment are increased by an order of magnitude when the real THz antennas are employed. Moreover, capacity values for the mobility over elevation scenario with constant gains, 3D symmetric beamwidths without adjustment are improved by four orders of the magnitude when real THz antennas are considered. Lastly, the real THz antennas under real mobility traces offer WF capacity and WF spectral efficiency values improved by five and three orders of the magnitudes, respectively, as compared to the constant gain, 3D symmetric beamwidths without adjustment. Conclusively, it can be inferred that considering the state-of-the-art THz antennas and real drone traces, employing the THz band (0.75-4.4 THz) for THz band Dr2Dr communications can promise WF-based capacity values in the order of several Gbps even if no beamwidth adjustment is provisioned, while for the ideal mobility case, i.e., perfect alignment, up to 2.8 Tbps of capacity is achievable, with a WF spectral efficiency of up to 11.88 bits/sec/Hz, depicting the potential of the THz band for Dr2Dr communications.

5.6 Complexity

Having proposed the joint channel selection, beamwidth adjustment and power control for capacity maximization via three schemes, i.e, MaxActive, CFB [15] and STD [18], the time complexity of the channel selection, power control and beamwidth adjustments will also affect the performance of the THz-enabled Dr2Dr link under mobility scenarios. For instance, on comparing the three channel selection schemes with EP allocation, STD scheme promises to be the simplest scheme since it considers all the THz narrowband channels for the transmission, while EP allocates the total transmit power equally over all the channels with negligible complexity. However, STD with EP provides the least channel capacity, since those channels will also be considered for transmission, where there are large absorption peaks, causing to degrade the capacity substantially. CFB scheme with EP allocation offers a higher complexity as compared to the STD with EP allocation, where the complexity contribution is mainly due to the selection of jointly flat bands between the total path gain and the colored noise PSD, while promising higher capacity values as compared to the STD with EP allocation, as presented in Chapter 4. Finally, MaxActive scheme, as proposed in Chapter 5, with EP allocation shows to be the most complex scheme as compared to the CFB and STD counterparts, where the channels are selected iteratively based on high SNR levels across the entire THz band

As compared to the EP allocation having the negligible complexity, WF allocation has a worst case complexity of 2^k, where k is the number of the THz narrowband channels [103]. Considering the STD scheme with WF provides the variable power allocation as well as deselecting the channels having high absorption peaks, thereby promising highest capacity values for a given mobility setting. Moreover, CFB with WF also provides similar capacity values as compared to the STD scheme with WF.

Lastly, MaxActive with WF allocation selects identical channels as compared to the STD with WF allocation. It is worth-mentioning here that MaxActive with even EP provides approximately the similar channels as offered by MaxActive and STD, each with WF allocations. Hence, MaxActive with EP promises to be a good complexity trade-off between MaxActive and STD with WF allocation, and STD and CFB with EP allocations. Finally, for addressing the beam misalignment, the beam training overhead e.g., via exhaustive search [104], will also contribute to the overall time complexity of the THz-enabled Dr2Dr links, as the communicating drones can get misaligned at each time instant, t, thereby arising the need to frequently re-align the Tx-Rx beams for achieving the maximum capacity values.

Chapter 6

CONCLUSIONS

In this dissertation, THz band communication has been presented for practical aerial scenarios at various atmospheric altitudes, directions and ranges by leveraging LBLRTM for obtaining realistic THz transmittance values corresponding to each aerial scenario setting. First, LBLRTM is employed for THz path loss and total usable bandwidth analyses for four practical aerial vehicle scenarios at various atmospheric altitudes considering constant noise model. Afterwards, capacity analysis has been presented under both no-fading and fading channel environments of the identical four aerial scenarios considering colored noise model. In the end, we have proposed joint channel selection, bandwidth adjustment and power control scheme, and provided a comprehensive mobility analysis. Detailed conclusions are provided as follows.

Considering the THz band (0.75-10 THz), path loss and total usable bandwidth analyses have been presented for four practical aerial scenarios including drones, jet planes, high altitude UAVs and satellites. We have shown that the THz band can be highly leveraged at high atmospheric altitudes, where almost the entire THz band, 9.25 THz wide, becomes feasible for communication as a single transmission window due to negligible water vapor concentrations at high atmospheric altitudes.

Secondly, we have assessed capacity and ergodic capacity of the aerial scenarios under no-fading and fading channel environments, respectively, also proposing an alternative way of computing altitude-dependent capacity based on variable bandwidth approach, considering CFBs between total path gain and noise, also comparing the variable bandwidth approach with the STD narrowband approach using both WF and EP allocations. The capacity analysis points out that the THz channel capacity without fading is improved under both WF and EP allocations at higher atmospheric altitudes: For both the proposed and the standard approaches, the sea-level capacity is enhanced by an order of magnitude for the drones, which is doubled for the jet plane scenario, which is further tripled for UAVs, which is again increased by another order of magnitude for the satellite communications. When ergodic capacity is computed for the fading scenarios, it is shown that the impact of fading vanishes at higher altitudes. Sea-level ergodic capacity is increased by an order of magnitude for drone-to-drone communications, providing several Tbps at 10 m, while 10s of Tbps is achievable among jet planes and UAVs, and several 100s of Tbps is possible for satellites/cubesats at 1 km under fading, suggesting that THz band is a promising alternative for aerial communications. The beam misalignment fading can be minimized by employing Tx-Rx antenna stabilizers, or by increasing the transmit power levels. Nevertheless, for the longer ranges, the beam misalignment fading diminishes as the Tx beam footprint becomes larger than the Rx beam.

Lastly, as a special case of the aerial communications, i.e., for drones over the THz band (0.75-4.4 THz), a scheme termed as MaxActive is proposed with the objective of selecting the channels for obtaining the maximum capacity. Then, we have considered the channel capacity maximization by proposing a joint channel selection, beamwidth adjustment and power control. Considering realistic 3D antenna model for THz beams, we have incorporated beamwidth adjustment of the Tx-Rx drones antennas to ensure communication over the high gain main lobe even under mobility uncertainties. Based on the joint process, various realistic Dr2Dr mobility scenarios are analyzed and capacity and spectral efficiency are obtained using MaxActive, also comparing with CFB and STD schemes with both WF and EP allocations.

For performance comparison, we have considered real drone mobility traces as well as real THz antennas to evaluate the true potential of Dr2Dr link performance under mobility. We have illustrated that due to mobility, Tx and Rx antennas observe frequent misalignments, causing a substantial degradation in the link performance, i.e., channel capacity and spectral efficiency of the three channel selection schemes. Results reveal that the beam misalignment degrades the link performance substantially. Also, the capacity of MaxActive even with EP allocation approximates the capacity of STD and MaxActive with WF, whereas MaxActive with EP clearly outperforms CFB and STD with EP allocation under all mobility scenarios. In regards to the spectral efficiency up to 100 m range, MaxActive EP outperforms CFB and STD schemes even with WF allocations. Numerical results further show that with the state-of-the-art THz antennas and real drone traces, employing the THz band (0.75-4.4 THz) can promise WF-based capacity values in the order of several Gbps even if no beamwidth adjustment is provisioned, while for the ideal mobility case, i.e., perfect alignment, up to 2.8 Tbps of capacity is achievable, with a WF spectral efficiency of up to 11.88 bits/sec/Hz, depicting the potential of the THz band for Dr2Dr communications.

Overall, we have illustrated that due to the mobile nature of the aerial vehicles including drones, jet planes, high altitude UAV and satellites, THz beams can get misaligned frequently causing the link performance degradation, e.g., channel capacity. Therefore, future research works for THz communications across various atmospheric altitudes should include employing the Tx-Rx antenna alignment techniques including antenna stabilizers, UM-MIMO arrays with smart beamforming techniques between communicating aerial vehicles by intelligently adjusting beam patterns, i.e., beam-steering, thereby promising uninterrupted high rate THz links between mobile aerial vehicles. Additionally, the beam-steering will also enable the aerial vehicles to transmit over multiple spots, e.g., drones-to-ground, satellites-to-HAPs/UAVs, satellites-to-jet planes, and so on. Also, extending the work presented in this dissertation to heterogeneous communication (inter-scenario) use-cases, such as drones to satellites, jet planes to satellites, jet planes to UAVs etc., as well as for cases when Tx and Rx are not at the same latitude would provide additional insights for realizing THz band communications in the air. Additionally, for the low altitude THz communications such as at the sea-level and drones, random atmospheric anomalies such as atmospheric ducting and the resulting humidity variations affecting the THz communication needs further investigation. For the high altitudes, i.e., THz space communications between 80 km to 600 km, incorporating the loss due to the ionospheric effects into the overall THz path loss is also left as a future work. Other research directions for THz band communications can include devising novel test-beds for real THz experiments, considering practical THz noise figure levels. Additionally, role of artificial and machine learning in addressing challenges of the THz band communication across all layers will be an important future research avenue, such as in channel estimation, UM-MIMO, IRS, spectrum management (cognitive radios), Mobile Edge Computing, etc.

Appendix A

Influence of Atmospheric Altitude on Path Gain and Noise

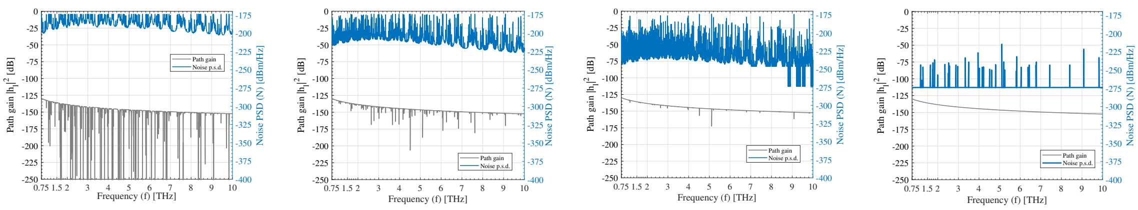

(a) $z_1 = z_2 = 10$ km. (b) $z_1 = z_2 = 20$ km. (c) $z_1 = z_2 = 40$ km. (d) $z_1 = z_2 = 100$ km.

Figure A.1 THz band deterministic path gain and noise PSD at various atmospheric altitudes, each at d=100 m.

Fig. A.1 depicts the path gain (left y-axis) and the noise PSD (right y-axis) as the functions of frequency over the THz band (0.75-10 THz) at various atmospheric altitudes with $z_1 = z_2$, i.e., horizontal communication ($\theta_{ZA} = 90°$) at $d = 100$ m, using US Standard 1976 model in LBLRTM. At $z_1 = z_2 = 10$ km, Fig. A.1(a) shows that the absorption contributions are considerable, while the noise follows color characteristics. At $z_1 = z_2 = 20$ km (Fig. A.1(b)), interestingly, although the absorption contributions are significantly lowered, however, unlike $z_1 = z_2 = 10$ km case, the noise becomes highly colored. Furthermore, at $z_1 = z_2 = 40$ km (Fig. A.1(c)), the path gain starts exhibiting negligible absorption contributions, behaving approximately as mere spread gain with the noise still observing higher color, due to the temperature variations as shown earlier in Fig. 2.3(a). Finally, reaching $z_1 = z_2 = 100$ km (Fig. A.1(d)), where there is an approximate atmospheric absence, the total path gain shows mere spread gain characteristics, while the noise depicts negligibly lower levels with intermittent sharp peaks. This infers that although the path gain exhibits entire considered band as flat, the noise trend makes it unrealistic for the

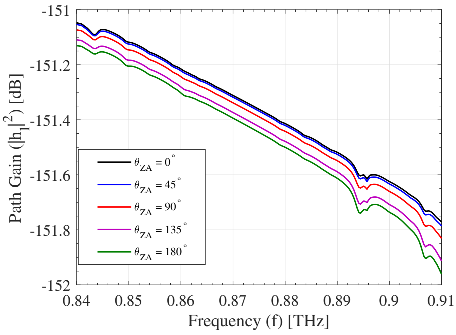

(a) Deterministic path gain.

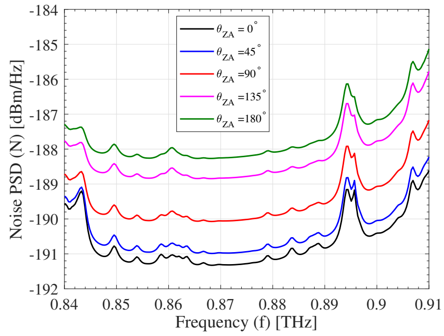

(b) Noise PSD.

Figure A.2 Deterministic path gain and noise PSD at $z_1 = 10$ km, $d = 1$ km, and z_2 is varying with respect to zenith angle settings.

flat constant narrowband transmission over the entire band. Rather, a need arises to determine those flat bands which are commonly flat, i.e. , across both the path gain and the noise PSD.

Fig. A.2 captures the absorption effect on the deterministic path gain (4.2) across various atmospheric layers by considering various θ_{ZA}, i.e. $0°$ (vertically up), $45°$ (slant-up), $90°$ (horizontal), $135°$ (slant-down), and $180°$ (vertically-down), hence varying receiver altitudes (z_2). US Standard 1976 weather profile is set in LBLRTM. Thanks to LBLRTM, the path gain trend illustrates that traversing across different atmospheric layers induces variations in the absorption. More specifically, Fig. A.2(a)-(b) shows that the least-affected absorption is across the vertically-up direction ($0°$), followed by $45°$, $90°$, $135°$ with the worst zenith angle being $180°$. Furthermore, even the noise is indeed effected by the atmospheric variations, as the noise is a function of transmittance from (4.9)-(4.11). In more detail, the noise PSD is favorable, i.e., at lower levels for the cases of traversing-up across the atmosphere, due to the lower atmospheric concentrations at higher altitudes.

BIBLIOGRAPHY

[1] I. F. Akyildiz, A. Kak, and S. Nie, "6G and Beyond: The Future of Wireless Communications Systems," *IEEE Access*, vol. 8, pp. 133995–134030, 2020.

[2] J. Huang, C. Wang, H. Chang, J. Sun, and X. Gao, "Multi-frequency multi-scenario millimeter wave mimo channel measurements and modeling for B5G wireless communication systems," *IEEE Journal on Selected Areas in Communications*, pp. 1–1, 2020.

[3] H. Elayan, O. Amin, R. M. Shubair, and M. Alouini, "Terahertz communication: The opportunities of wireless technology beyond 5G," in *2018 International Conference on Advanced Communication Technologies and Networking (CommNet)*, pp. 1–5, April 2018.

[4] I. F. Akyildiz, J. M. Jornet, and C. Han, "Terahertz Band: Next Frontier for Wireless Communications," *Physical Communication*, vol. 12, p. 16–32, Sept. 2014.

[5] H.-J. Song and T. Nagatsuma, "Present and Future of Terahertz Communications," *IEEE Transactions on Terahertz Science and Technology*, vol. 1, no. 1, pp. 256–263, 2011.

[6] T. S. Rappaport, Y. Xing, O. Kanhere, S. Ju, A. Madanayake, S. Mandal, A. Alkhateeb, and G. C. Trichopoulos, "Wireless Communications and Applications Above 100 GHz: Opportunities and Challenges for 6G and Beyond," *IEEE Access*, vol. 7, pp. 78729–78757, 2019.

[7] M. Latva-aho, "Radio Access Networking Challenges Towards 2030," in *Proc. 1st International Telecommunication Union Workshop on Network 2030, New York*, Oct. 2018.

[8] Z. Zhang, Y. Xiao, Z. Ma, M. Xiao, Z. Ding, X. Lei, G. K. Karagiannidis, and P. Fan, "6G Wireless Networks: Vision, Requirements, Architecture, and Key

Technologies," *IEEE Vehicular Technology Magazine*, vol. 14, no. 3, pp. 28–41, 2019.

[9] L. Bariah, L. Mohjazi, S. Muhaidat, P. C. Sofotasios, G. K. Kurt, H. Yanikomeroglu, and O. A. Dobre, "A Prospective Look: Key Enabling Technologies, Applications and Open Research Topics in 6G Networks," *IEEE Access*, vol. 8, pp. 174792–174820, 2020.

[10] A. A. Boulogeorgos, A. Alexiou, T. Merkle, C. Schubert, R. Elschner, A. Katsiotis, P. Stavrianos, D. Kritharidis, P. Chartsias, J. Kokkoniemi, M. Juntti, J. Lehtomaki, A. Teixeira, and F. Rodrigues, "Terahertz Technologies to Deliver Optical Network Quality of Experience in Wireless Systems Beyond 5G," *IEEE Communications Magazine*, vol. 56, no. 6, pp. 144–151, 2018.

[11] NetWorld2020, "Smart networks in the context of ngi," *Strategic Research and Innovation Agenda 2021-27*, pp. 1–116, 2018.

[12] I. F. Akyildiz and J. M. Jornet, "Realizing Ultra-Massive MIMO (1024×1024) Communication in the (0.06-10) Terahertz band," *Nano Comm. Netw.*, vol. 8, pp. 46–54, 2016.

[13] Y. Yang, M. Mandehgar, and D. Grischkowsky, "Determination of the water vapor continuum absorption by thz-tds and molecular response theory," *Opt. Express*, vol. 22, pp. 4388–4403, Feb 2014.

[14] C. Han and I. F. Akyildiz, "Distance-Aware Bandwidth-Adaptive Resource Allocation for Wireless Systems in the Terahertz Band," *IEEE Transactions on Terahertz Science and Technology*, vol. 6, no. 4, pp. 541–553, 2016.

[15] A. Saeed, O. Gurbuz, A. O. Bicen, and M. A. Akkas, "Variable-Bandwidth Model and Capacity Analysis for Aerial Communications in the Terahertz Band," *IEEE Journal on Selected Areas in Communications*, pp. 1–1, 2021.

[16] V. Petrov, D. Moltchanov, M. Komar, A. Antonov, P. Kustarev, S. Rakheja, and Y. Koucheryavy, "Terahertz Band Intra-Chip Communications: Can Wireless Links Scale Modern x86 CPUs?," *IEEE Access*, vol. 5, pp. 6095–6109, 2017.

[17] M. A. Akkas, "Study of absorption-defined transmission windows in the terahertz band," *Ad Hoc Networks*, vol. 74, pp. 30 – 33, 2018.

[18] J. M. Jornet and I. F. Akyildiz, "Channel Modeling and Capacity Analysis for Electromagnetic Wireless Nanonetworks in the Terahertz Band," *IEEE Trans. Wireless Communications*, vol. 10, no. 10, pp. 3211–3221, 2011.

[19] M. Stojanovic and J. Preisig, "Underwater Acoustic Communication Channels: Propagation Models and Statistical Characterization," *IEEE Communications Magazine*, vol. 47, pp. 84–89, January 2009.

[20] C. Han, A. O. Bicen, and I. F. Akyildiz, "Multi-ray channel modeling and wideband characterization for wireless communications in the terahertz band," *IEEE Transactions on Wireless Communications*, vol. 14, pp. 2402–2412, May 2015.

[21] A. A. Boulogeorgos, E. N. Papasotiriou, and A. Alexiou, "Analytical performance assessment of thz wireless systems," *IEEE Access*, vol. 7, pp. 11436–11453, 2019.

[22] Q. Pham, F. Fang, V. N. Ha, M. J. Piran, M. Le, L. B. Le, W. Hwang, and Z. Ding, "A survey of multi-access edge computing in 5g and beyond: Fundamentals, technology integration, and state-of-the-art," *IEEE Access*, vol. 8, pp. 116974–117017, 2020.

[23] M. S. Allahham, M. F. Al-Sa'd, A. Al-Ali, A. Mohamed, T. Khattab, and A. Erbad, "Dronerf dataset: A dataset of drones for rf-based detection, classification and identification," *Data in Brief*, vol. 26, p. 104313, 2019.

[24] M. Mirahsan, R. Schoenen, and H. Yanikomeroglu, "Hethetnets: Heterogeneous traffic distribution in heterogeneous wireless cellular networks," *IEEE Journal on Selected Areas in Communications*, vol. 33, no. 10, pp. 2252–2265, 2015.

[25] D. F. Lamiano, K. Leung, L. C. Monticone, W. J. Wilson, and B. Phillips, "Digital broadband vhf aeronautical communications for air traffic control," in *2009 Integrated Communications, Navigation and Surveillance Conference*, pp. 1–12, 2009.

[26] B. Li, Z. Fei, and Y. Zhang, "UAV communications for 5G and beyond: Recent advances and future trends," *IEEE Internet of Things Journal*, vol. 6, no. 2, pp. 2241–2263, 2019.

[27] A. D. Panagopoulos, P. M. Arapoglou, and P. G. Cottis, "Satellite communications at ku, ka, and v bands: Propagation impairments and mitigation techniques," *IEEE Communications Surveys Tutorials*, vol. 6, no. 3, pp. 2–14, 2004.

[28] ESA, "Satellite frequency bands," *European Space Agency*, 2018.

[29] K. Tekbiyik, A. R. Ekti, G. Karabulut-Kurt, A. Görçin, and H. Yanikomeroglu, "A holistic investigation on terahertz propagation and channel modeling toward vertical heterogeneous networks," *ArXiv*, vol. abs/2005.00509, 2020.

[30] M. T. Dabiri, H. Safi, S. Parsaeefard, and W. Saad, "Analytical channel models for millimeter wave uav networks under hovering fluctuations," *IEEE Transactions on Wireless Communications*, vol. 19, no. 4, pp. 2868–2883, 2020.

[31] M. Saqlain, N. M. Idrees, L. Zhang, and X. Yu, "Capacity analysis of opto-electronic thz earth-satellite links," in *2019 Asia Communications and Photonics Conference (ACP)*, pp. 1–3, 2019.

[32] J. Y. Suen, M. T. Fang, S. P. Denny, and P. M. Lubin, "Modeling of terabit geostationary terahertz satellite links from globally dry locations," *IEEE Transactions on Terahertz Science and Technology*, vol. 5, pp. 299–313, March 2015.

[33] J. Sun, F. Hu, and S. Lucyszyn, "Predicting atmospheric attenuation under pristine conditions between 0.1 and 100 THz," *IEEE Access*, vol. 4, pp. 9377–9399, 2016.

[34] S. Hayat, E. Yanmaz, and R. Muzaffar, "Survey on Unmanned Aerial Vehicle Networks for Civil Applications: A Communications Viewpoint," *IEEE Communications Surveys Tutorials*, vol. 18, no. 4, pp. 2624–2661, 2016.

[35] E. Yanmaz, S. Yahyanejad, B. Rinner, H. Hellwagner, and C. Bettstetter, "Drone Networks: Communications, Coordination, and Sensing," *Ad Hoc Networks*, vol. 68, pp. 1 – 15, 2018. Advances in Wireless Communication and Networking for Cooperating Autonomous Systems.

[36] G. Chmaj and H. Selvaraj, "Distributed Processing Applications for UAV/drones: A Survey," in *Progress in Systems Engineering* (H. Selvaraj, D. Zydek, and G. Chmaj, eds.), (Cham), pp. 449–454, Springer International Publishing, 2015.

[37] M. Song, Y. Huo, T. Lu, X. Dong, and Z. Liang, "Meteorologically Introduced Impacts on Aerial Channels and UAV Communications," in *2020 IEEE 92nd Vehicular Technology Conference (VTC2020-Fall)*, pp. 1–5, 2020.

[38] W. Xia, V. Semkin, M. Mezzavilla, G. Loianno, and S. Rangan, "Multi-Array Designs for mmWave and Sub-THz Communication to UAVs," in *2020 IEEE*

21st International Workshop on Signal Processing Advances in Wireless Communications (SPAWC), pp. 1–5, 2020.

[39] R. Karim, A. Iftikhar, B. Ijaz, and I. Ben Mabrouk, “The Potentials, Challenges, and Future Directions of On-Chip-Antennas for Emerging Wireless Applications—A Comprehensive Survey,” *IEEE Access*, vol. 7, pp. 173897–173934, 2019.

[40] L. Xu, M. Chen, M. Chen, Z. Yang, C. Chaccour, W. Saad, and C. S. Hong, “Joint Location, Bandwidth and Power Optimization for THz-enabled UAV Communications,” *IEEE Communications Letters*, pp. 1–1, 2021.

[41] A. A. Raja, M. A. Jamshed, H. Pervaiz, and S. A. Hassan, “Performance Analysis of UAV-assisted Backhaul Solutions in THz Enabled Hybrid Heterogeneous Network,” in *IEEE INFOCOM 2020 - IEEE Conference on Computer Communications Workshops (INFOCOM WKSHPS)*, pp. 628–633, 2020.

[42] X. Wang, P. Wang, M. Ding, Z. Lin, F. Lin, B. Vucetic, and L. Hanzo, “Performance Analysis of Terahertz Unmanned Aerial Vehicular Networks,” *IEEE Transactions on Vehicular Technology*, vol. 69, no. 12, pp. 16330–16335, 2020.

[43] R. Mendrzik, D. Cabric, and G. Bauch, “Error Bounds for Terahertz MIMO Positioning of Swarm UAVs for Distributed Sensing,” in *2018 IEEE International Conference on Communications Workshops (ICC Workshops)*, pp. 1–6, 2018.

[44] S. Farrag, E. Maher, A. El-Mahdy, and F. Dressler, “Outage Probability Analysis of UAV Assisted Mobile Communications in THz Channel,” in *2021 16th Annual Conference on Wireless On-demand Network Systems and Services Conference (WONS)*, pp. 1–8, 2021.

[45] Y. Pan, K. Wang, C. Pan, H. Zhu, and J. Wang, “UAV-Assisted and Intelligent Reflecting Surfaces-Supported Terahertz Communications,” *IEEE Wireless Communications Letters*, pp. 1–1, 2021.

[46] S. Mumtaz, J. Jornet, J. Aulin, W. Gerstacker, X. Dong, and b. ai, “Terahertz Communication for Vehicular Networks,” *IEEE Transactions on Vehicular Technology*, vol. 66, pp. 5617–5625, 07 2017.

[47] S. K. Moorthy and Z. Guan, “LeTera: Stochastic Beam Control Through ESN Learning in Terahertz-Band Wireless UAV Networks,” in *IEEE INFOCOM 2020 - IEEE Conference on Computer Communications Workshops (INFOCOM WKSHPS)*, pp. 1039–1044, 2020.

[48] Z. Guan and T. Kulkarni, "On the Effects of Mobility Uncertainties on Wireless Communications between Flying Drones in the mmWave/THz Bands," in *IEEE INFOCOM 2019 - IEEE Conference on Computer Communications Workshops (INFOCOM WKSHPS)*, pp. 768–773, 2019.

[49] S. Krishna Moorthy and Z. Guan, "Beam Learning in MmWave/THz-band Drone Networks Under In-Flight Mobility Uncertainties," *IEEE Transactions on Mobile Computing*, pp. 1–1, 2020.

[50] S.A. Clough , M.W. Shephard , E.J. Mlawer , J.S. Delamere , M.J. Iacono , K. Cady-Pereira , S. Boukabara and P.D. Brown, "Atmospheric Radiative Transfer Modeling: A Summary of the AER Codes," *Journal of Quantitative Spectroscopy and Radiative Transfer*, vol. 91, no. 2, pp. 233 – 244, 2005.

[51] S. A. Clough, M. J. Iacono, and J.-L. Moncet, "Line-by-Line Calculations of Atmospheric Fluxes and Cooling Rates: Application to Water Vapor," *Journal of Geophysical Research: Atmospheres*, vol. 97, no. D14, pp. 15761–15785, 1992.

[52] R. M. Goody and Y. L. Yung, *Atmospheric radiation : theoretical basis*. New York N.Y.: Oxford University Press, 1989.

[53] H. T. Friis, "A note on a simple transmission formula," *Proceedings of the IRE*, vol. 34, pp. 254–256, May 1946.

[54] D. F. Swinehart, "The beer-lambert law," *Journal of Chemical Education*, vol. 39, no. 7, p. 333, 1962.

[55] F. Strong, "Correction: Theoretical basis of the bouguer-beer law of radiation absorption," *Analytical Chemistry*, vol. 24, no. 12, pp. 2013–2013, 1952.

[56] I. Gordon, L. Rothman, C. Hill, R. Kochanov, Y. Tan, P. Bernath, M. Birk, V. Boudon, A. Campargue, K. Chance, B. Drouin, J.-M. Flaud, R. Gamache, J. Hodges, D. Jacquemart, V. Perevalov, A. Perrin, K. Shine, M.-A. Smith, J. Tennyson, G. Toon, H. Tran, V. Tyuterev, A. Barbe, A. CsÃ¡szÃ¡r, V. Devi, T. Furtenbacher, J. Harrison, J.-M. Hartmann, A. Jolly, T. Johnson, T. Karman, I. Kleiner, A. Kyuberis, J. Loos, O. Lyulin, S. Massie, S. Mikhailenko, N. Moazzen-Ahmadi, H. MÃ¼ller, O. Naumenko, A. Nikitin, O. Polyansky, M. Rey, M. Rotger, S. Sharpe, K. Sung, E. Starikova, S. Tashkun, J. V. Auwera, G. Wagner, J. Wilzewski, P. WcisÅ‚o, S. Yu, and E. Zak, "The hitran2016 molecular spectroscopic database," *Journal of Quantitative Spectroscopy and Radiative Transfer*, vol. 203, pp. 3–69, 2017. HITRAN2016 Special Issue.

[57] L.S. Rothman , I.E. Gordon, Y. Babikov , A. Barbe , D. Chris Benner , P.F. Bernath , M. Birk , L. Bizzocchi , V. Boudon , L.R. Brown , A. Campargue , K. Chance , E.A. Cohen , L.H. Coudert , V.M. Devi , B.J. Drouin , A. Fayt , J.-M. Flaud , R.R. Gamache , J.J. Harrison , J.-M. Hartmann , C. Hill , J.T. Hodges , D. Jacquemart , A. Jolly , J. Lamouroux , R.J. Le Roy , G. Li , D.A. Long , O.M. Lyulin , C.J. Mackie , S.T. Massie , S. Mikhailenko , H.S.P. Müller , O.V. Naumenko , A.V. Nikitin , J. Orphal , V. Perevalov , A. Perrin , E.R. Polovtseva , C. Richard , M.A.H. Smith , E. Starikova , K. Sung , S. Tashkun , J. Tennyson , G.C. Toon , Vl.G. Tyuterev and G. Wagner, "The hitran2012 molecular spectroscopic database," *Journal of Quantitative Spectroscopy and Radiative Transfer*, vol. 130, pp. 4 – 50, 2013. HITRAN2012 special issue.

[58] S. Mikhailenko, B. Yu.L., and G. V.F., "Information-calculating system spectroscopy of atmospheric gases. the structure and main functions," *Atmospheric and Oceanic Optics*, vol. 18, pp. 685–695, 09 2005.

[59] S. Paine, "The am atmospheric model," Sept. 2019.

[60] Y. Yang, A. Shutler, and D. Grischkowsky, "Measurement of the Transmission of the Atmosphere from 0.2 to 2 THz," *Opt. Express*, vol. 19, pp. 8830–8838, Apr 2011.

[61] S. Wohnsiedler, M. Theuer, M. Herrmann, S. Islam, J. Jonuscheit, R. Beigang, and F. Hase, "Simulation and Experiment of Terahertz Stand-off Detection," in *Terahertz Technology and Applications II* (K. J. Linden, L. P. Sadwick, and C. M. O'Sullivan, eds.), vol. 7215, pp. 101 – 108, International Society for Optics and Photonics, SPIE, 2009.

[62] L. Rothman, I. Gordon, Y. Babikov, A. Barbe, D. C. Benner, P. Bernath, M. Birk, L. Bizzocchi, V. Boudon, L. Brown, A. Campargue, K. Chance, E. Cohen, L. Coudert, V. Devi, B. Drouin, A. Fayt, J.-M. Flaud, R. Gamache, J. Harrison, J.-M. Hartmann, C. Hill, J. Hodges, D. Jacquemart, A. Jolly, J. Lamouroux, R. L. Roy, G. Li, D. Long, O. Lyulin, C. Mackie, S. Massie, S. Mikhailenko, H. MÃ¼ller, O. Naumenko, A. Nikitin, J. Orphal, V. Perevalov, A. Perrin, E. Polovtseva, C. Richard, M. Smith, E. Starikova, K. Sung, S. Tashkun, J. Tennyson, G. Toon, V. Tyuterev, and G. Wagner, "The hitran2012 molecular spectroscopic database," *Journal of Quantitative Spectroscopy and Radiative Transfer*, vol. 130, pp. 4 – 50, 2013. HITRAN2012 special issue.

[63] P. M. Rowe, "MATLAB LBLRTM interface," 2019.

[64] I. F. Akyildiz and A. Kak, "The internet of space things/cubesats: A ubiquitous cyber-physical system for the connected world," *Computer Networks*, vol. 150, pp. 134 – 149, 2019.

[65] D. M. Slocum, E. J. Slingerland, R. H. Giles, and T. M. Goyette, "Atmospheric absorption of terahertz radiation and water vapor continuum effects," *Journal of Quantitative Spectroscopy and Radiative Transfer*, vol. 127, pp. 49 – 63, 2013.

[66] S. A. R. Naqvi, S. A. Hassan, H. Pervaiz, and Q. Ni, "Drone-aided communication as a key enabler for 5G and resilient public safety networks," *IEEE Communications Magazine*, vol. 56, pp. 36–42, Jan 2018.

[67] E. Yanmaz, S. Yahyanejad, B. Rinner, H. Hellwagner, and C. Bettstetter, "Drone networks: Communications, coordination, and sensing," *Ad Hoc Networks*, vol. 68, pp. 1 – 15, 2018. Advances in Wireless Communication and Networking for Cooperating Autonomous Systems.

[68] G. Yang, X. Lin, Y. Li, H. Cui, M. Xu, D. Wu, H. Ryden, and S. B. Redhwan, "A telecom perspective on the internet of drones: From lte-advanced to 5G," *CoRR*, vol. abs/1803.11048, 2018.

[69] I. Tuzcu, P. Marzocca, E. Cestino, G. Romeo, and G. Frulla, "Stability, control, and simulation of high-altitude-long-endurance uavs," *Journal of Guidance, Control, and Dynamics*, vol. 30, pp. 713–721, May-June 2007.

[70] H. Elayan, O. Amin, R. M. Shubair, and M. Alouini, "Terahertz communication: The opportunities of wireless technology beyond 5G," in *2018 International Conference on Advanced Communication Technologies and Networking (CommNet)*, pp. 1–5, April 2018.

[71] J. C. McDowell, "The edge of space: Revisiting the karman line," *Acta Astronautica*, vol. 151, pp. 668 – 677, 2018.

[72] S. U. Hwu, K. B. deSilva, and C. T. Jih, "Terahertz (THz) wireless systems for space applications," in *2013 IEEE Sensors Applications Symposium Proceedings*, pp. 171–175, Feb 2013.

[73] L. Sun, W. Huang, Y. Zhou, J. Yang, and Y. Wang, "Monitor link assignment for reentry users based on beidou inter-satellite links," *Advances in Space Research*, vol. 64, no. 3, pp. 747 – 758, 2019.

[74] I. F. Akyildiz, J. M. Jornet, and S. Nie, “A new cubesat design with reconfigurable multi-band radios for dynamic spectrum satellite communication networks,” *Ad Hoc Networks*, vol. 86, pp. 166 – 178, 2019.

[75] T. Schneider, A. Wiatrek, S. Preussler, M. Grigat, and R. Braun, “Link budget analysis for terahertz fixed wireless links,” *IEEE Transactions on Terahertz Science and Technology*, vol. 2, pp. 250–256, March 2012.

[76] C. Han, A. O. Bicen, and I. F. Akyildiz, “Multi-wideband waveform design for distance-adaptive wireless communications in the terahertz band,” *IEEE Transactions on Signal Processing*, vol. 64, pp. 910–922, Feb 2016.

[77] N. Khalid, N. A. Abbasi, and O. B. Akan, “300 ghz broadband transceiver design for low-thz band wireless communications in indoor internet of things,” in *2017 IEEE International Conference on Internet of Things (iThings) and IEEE Green Computing and Communications (GreenCom) and IEEE Cyber, Physical and Social Computing (CPSCom) and IEEE Smart Data (SmartData)*, pp. 770–775, 2017.

[78] T. Yilmaz and O. B. Akan, “Utilizing terahertz band for local and personal area wireless communication systems,” in *2014 IEEE 19th International Workshop on Computer Aided Modeling and Design of Communication Links and Networks (CAMAD)*, pp. 330–334, Dec 2014.

[79] A. Fotouhi, M. Ding, and M. Hassan, “Flying drone base stations for macro hotspots,” *IEEE Access*, vol. 6, pp. 19530–19539, 2018.

[80] ITU, “Systems for public mobile communications with aircraft,” *Report ITU-R M.2282-0*, vol. M., pp. 1–20, December 2013.

[81] J. L. Zhendong Yin, Zhenguo Shi and Z. Wu, “Design of unmanned aerial vehicle space communication links based on ds-uwb,” *Information Technology Journal*, vol. 9, no. 9, pp. 1713–1718, 2010.

[82] ITU, “Technical and operational characteristics of satellites operating in the range 20-375 THz,” *RECOMMENDATION ITU-R S.1590*, vol. 264, no. /4, pp. 1–20, 2002.

[83] G. Djuknic, J. Freidenfelds, and Y. Okunev, “Establishing wireless communications services via high-altitude aeronautical platforms: A concept whose time has come?,” *Communications Magazine, IEEE*, vol. 35, pp. 128 – 135, 10 1997.

[84] M. M. Azari, G. Geraci, A. Garcia-Rodriguez, and S. Pollin, "Cellular uav-to-uav communications," in *2019 IEEE 30th Annual International Symposium on Personal, Indoor and Mobile Radio Communications (PIMRC)*, pp. 1–7, 2019.

[85] A. A. Farid and S. Hranilovic, "Outage capacity optimization for free-space optical links with pointing errors," *Journal of Lightwave Technology*, vol. 25, no. 7, pp. 1702–1710, 2007.

[86] M. D. Yacoub, "The α-μ distribution: A physical fading model for the stacy distribution," *IEEE Transactions on Vehicular Technology*, vol. 56, no. 1, pp. 27–34, 2007.

[87] F. Box, "Utilization of atmospheric transmission losses for interference-resistant communications," *IEEE Transactions on Communications*, vol. 34, pp. 1009–1015, October 1986.

[88] A. Goldsmith, *Wireless Communications.* New York, NY, USA: Cambridge University Press, 2005.

[89] G. Castellanos, M. Deruyck, L. Martens, and W. Joseph, "Performance evaluation of direct-link backhaul for uav-aided emergency networks," *Sensors*, vol. 19, no. 15, 2019.

[90] ITU, "Compatibility study to support the line-of-sight control and non-payload communications link(s) for unmanned aircraft systems proposed in the frequency band 5 030-5 091 Mhz," *RECOMMENDATION ITU-R S.1590*, no. 264/4, 2011.

[91] ITU, "Fci technology investigations: L band compatibility criteria and interference scenarios study," *Eurocontrol*, vol. 1, August 2009.

[92] F. US Department of Transportation, "Acceptable methods, techniques, and practices – aircraft alterations," in *AFS-300*, vol. AC No: 43.13-2B, pp. –, 2008.

[93] J. Angevain, A. Ihle, G. Rodrigues, and J. Santiago-Prowald, "Large deployable spaceborne reflector antennas in europe: Progress status and perspectives," in *2019 13th European Conference on Antennas and Propagation (EuCAP)*, pp. 1–5, 2019.

[94] N. Chahat, R. E. Hodges, J. Sauder, M. Thomson, E. Peral, and Y. Rahmat-Samii, "Cubesat deployable ka-band mesh reflector antenna development for

earth science missions," *IEEE Transactions on Antennas and Propagation*, vol. 64, no. 6, pp. 2083–2093, 2016.

[95] P. V. Trinh, T. Cong Thang, and A. T. Pham, "Mixed mmwave rf/fso relaying systems over generalized fading channels with pointing errors," *IEEE Photonics Journal*, vol. 9, no. 1, pp. 1–14, 2017.

[96] M. T. Dabiri, S. M. S. Sadough, and M. A. Khalighi, "Channel modeling and parameter optimization for hovering uav-based free-space optical links," *IEEE Journal on Selected Areas in Communications*, vol. 36, no. 9, pp. 2104–2113, 2018.

[97] C. A. Balanis, *Antenna theory: analysis and design*. Wiley-Interscience, 2005.

[98] J. Wildman, P. H. J. Nardelli, M. Latva-aho, and S. Weber, "On the joint impact of beamwidth and orientation error on throughput in directional wireless poisson networks," *IEEE Transactions on Wireless Communications*, vol. 13, pp. 7072–7085, Dec 2014.

[99] H.-T. Zhu, Q. Xue, J.-N. Hui, and S. W. Pang, "A 750–1000 ghz h -plane dielectric horn based on silicon technology," *IEEE Transactions on Antennas and Propagation*, vol. 64, no. 12, pp. 5074–5083, 2016.

[100] E. Carrasco and J. Perruisseau-Carrier, "Reflectarray antenna at terahertz using graphene," *IEEE Antennas and Wireless Propagation Letters*, vol. 12, pp. 253–256, 2013.

[101] N. Chahat, T. J. Reck, C. Jung-Kubiak, T. Nguyen, R. Sauleau, and G. Chattopadhyay, "1.9-thz multiflare angle horn optimization for space instruments," *IEEE Transactions on Terahertz Science and Technology*, vol. 5, no. 6, pp. 914–921, 2015.

[102] L. Guo, H. Meng, L. Zhang, and J. Ge, "Design of mems on-chip helical antenna for thz application," in *2016 IEEE MTT-S International Microwave Workshop Series on Advanced Materials and Processes for RF and THz Applications (IMWS-AMP)*, pp. 1–4, 2016.

[103] D. Palomar and J. Fonollosa, "Practical algorithms for a family of waterfilling solutions," *IEEE Transactions on Signal Processing*, vol. 53, no. 2, pp. 686–695, 2005.

[104] C. Jeong, J. Park, and H. Yu, "Random access in millimeter-wave beamforming cellular networks: issues and approaches," *IEEE Communications Magazine*, vol. 53, no. 1, pp. 180–185, 2015.